OBSERVATION OF A RESONANCE AT 2.36 GeV/c$^2$

IN 400 GeV/c pN INTERACTIONS

By

James K. Woosley

Dissertation

Submitted to the Faculty of the

Graduate School of Vanderbilt University

in partial fulfillment of the requirements

for the degree of

DOCTOR OF PHILOSOPHY

in

Physics

August, 1987

Nashville, Tennessee

Approved:                                          Date:

_Medford S. Webster_ _____    _May 8, 1987_

_Volker E. Oberacker_ _____    _May 8, 1987_

_Med E. Gioma_ _____    _May 8, 1987_

_Thomas J. Weiler_ _____    _May 8, 1987_

_R. F. Arenstorf_ _____    _May 8, 1987_

# OBSERVATION OF A RESONANCE AT 2.36 GeV/c$^2$ IN 400 GeV/c pN INTERACTIONS

## JAMES K. WOOSLEY

Dissertation under the direction of Professor Medford S. Webster

The purpose of this dissertation is to present evidence for a resonance in an analysis of data obtained by Fermi National Accelerator Laboratory (FNAL) experiment E623. This experiment was performed in the FNAL Multiparticle Spectrometer (MPS) utilizing a 400 GeV/c proton beam on a nuclear target. The MPS for E623 included a hardware trigger designed to enhance the inclusive $K^+K^-K^+K^-$ sample, with low $K^+K^-$ mass to enhance the detection of pairs of $\phi$ mesons observed through the $\phi \longrightarrow K^+K^-$ decay.

This resonance was observed in the inclusive $K^+K^-K^+K^-\pi^+\pi^-$ subset of the E623 data, comprising 94,786 triggered events. The $K^+K^-\pi^+\pi^-$ spectrum in these events displayed evidence of resonance production at a mass of 2.363 $\pm$ 0.005 GeV/c$^2$, with a measured width of 0.040 $\pm$ 0.015 GeV/c$^2$. An excess of 1291 $^{+368}_{-338}$ entries over a smooth background was observed. This excess is correlated with high associated particle multiplicity and with high transverse momentum relative to the beam. The additional $K^+K^-$ pair in the event produces an associated $\phi$ in 293 $\pm$ 279 entries. With the $\phi K^+K^-\pi^+\pi^-$ acceptance of (3.3 $\pm$ 0.4) x 10$^{-4}$, the cross-section of this subset of the observed resonance is

$$\sigma(\phi X(2.36)) \cdot BR(X \longrightarrow K^+K^-\pi^+\pi^-) = 1.77 \pm 1/70 \ \mu b.$$

No substates are observed to occur in the $K^+K^-\pi^+\pi^-$; thus, the parity of the state is $(-1)^J$.

Since the width is consistent with the experimental mass resolution, it can be argued that that state is too narrow to be an ordinary $q\bar{q}$ meson. The correspondence to the previously uncorroborated result of Oh et al in $\bar{p}p$ collisions [Phys. Rev. Lett. 24, 1257 (1970)], suggests interpretation as a $s\bar{s}u\bar{u}$ exotic meson. However, on the basis of available information, no firm conclusions about the nature of the state can be drawn.

Approved_____Date_____
              Advisor

## ACKNOWLEDGEMENTS

Finally, I would like to thank my parents, Wilcy and Mona Woosley, and the rest of my family, for their continued support as this effort has continued. I also wish to extend my special thanks to my fiancee, Jann Melton, and her daughter, Jeanna, for their support, and to Jann for her help in typing this manuscript. I could not have done it without them, and it is to them that I dedicate this dissertation.

## SPECIAL ACKNOWLEDGEMENT

As Dr. Isaac Asimov once noted, "the golden age of science fiction is when you are twelve." That certainly proved true for me, as it was then that I first encountered the fiction of Edward Elmer Smith, Ph.D. Dr. Smith invented most of the concepts that became the familiar cliches of science fiction, and, as most inventors, he saw further and more clearly than those who have come afterward.

I first encountered Dr. Smith's fiction in 1970, and my desire to become a physicist dates directly to that event. If some of his romantic notions have been tempered by hard reality, it is of little consequence. His real lessons were in the arena of hard work; in following his example I have always strived to enjoy what I do and to do it well. Further, I have learned to recognize parallels between his character's capabilities and those of the real world -- parallels that I often find astoundingly close to contemporary theory.

As I achieve this goal, until now the most important goal in my life, I wish once again to acknowledge that this destination was the one I set out towards over seventeen years ago. During this time, there have been other influences -- Robert A. Heinlein; Forrest J Ackerman; Spider Robinson; Al Fennelly -- men whose work has inspired me upward, and who I also wish to thank. Always, though, the chief steersman and lighthouse keeper has been Dr. Edward Elmer Smith.

# TABLE OF CONTENTS

# LIST OF TABLES

LIST OF FIGURES

CHAPTER I

INTRODUCTION

In May and June, 1982, Fermi National Accelerator Laboratory (FNAL or Fermilab) Experiment E623[1,2] collected data on the production of states with two low-mass $K^+K^-$ pairs. In E623, a 400 GeV/c proton beam was incident on a segmented, plastic scintillator target. Data for tracking and momentum determination were recorded by the Fermilab Multi-Particle Spectrometer (FMPS), including two atmospheric pressure nitrogen threshold Cherenkov counters for particle identification. These counters distinguished $\pi$ from K or p in the 5.7 - 23.0 GeV/c momentum band. The four kaon requirement was implemented by an on-line trigger processor.[3]

The purpose of this experiment was the identification of massive states which decayed through the $\phi\phi$ channel with the $\phi \longrightarrow K^+K^-$ decay mode; hence, the four kaon trigger. This final state is believed to be particularly clean for the observation of glueballs or exotic mesons. It has also been used for precision studies of the quantum numbers of the $\eta_C$. The trigger is also sensitive to a portion of the inclusive $D_S DK$ cross-section, through the well-known $D_S \longrightarrow \phi\pi$ decay mode. The results of these studies have been reported elsewhere.[4-10]

The present work reports the results of a study of the $K^+K^-K^+K^-\pi^+\pi^-$ final state observed in this experiment. A resonance candidate at a mass of 2.36 GeV/c$^2$ and with a width of 0.040 GeV/c$^2$ has been observed

in the $K^+K^-\pi^+\pi^-$ spectrum. This candidate has not been conclusively identified with any previously observed resonance state. Further, the width of the observed enhancement is dominated by the experimental resolution, suggesting either a narrow hadronic width, a weak decay mode, or an exotic structure.

A qualitative discussion of the theory of hadronic resonances will be presented in chapter II. The configuration of the FMPS used in this experiment will be given in chapter III. The data analysis routine will be described in chapter IV. In chapter V, the results and interpretation of this study will be presented. Finally, the conclusions will be presented in chapter VI.

CHAPTER II

THEORY

In this chapter, a qualitative discussion of hadronic interactions is presented.[11-20] In particular, a discussion of the production of strange and charmed mesons, of glueballs, and of exotic mesons is given. A summary of those aspects of quantum chromodynamics necessary to understand these processes is provided first. Strange meson production and spectroscopy will be discussed in Sect. B, and charmed mesons in Sect. C. A general discussion of exotic hadrons follows in Sect. D, with glueballs and $q^2\bar{q}^2$ states in the subsequent sections.

A.   Quantum Chromodynamics

Quantum chromodynamics, or QCD, is the currently accepted theory of the strong force. This theory has been developed from a number of experimental results and previous theories, and a review of the process by which it arose will serve as an introduction to its techniques and results.

In 1963, when Gell-Mann, Ne'eman, and Zweig discovered that the spectrum of elementary scalar mesons formed an $\underline{8} \pm \underline{1}$ representation of the symmetry group SU(3), as shown in Fig. 1, there was no reason to believe that the "quarks" of the fundamental $\underline{3}$ representation [Fig. 2] were other than mathematical fictions. If the quarks are real entities, they must be fermions to account for the spins of the observed hadrons.
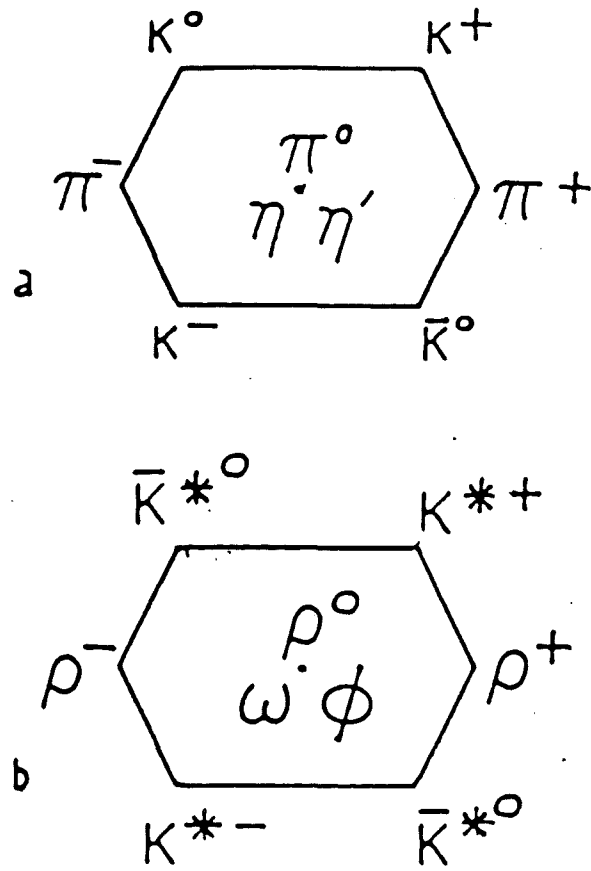
FIG. 1.   Pseudoscalar (a) and Vector (b) Meson Nonets
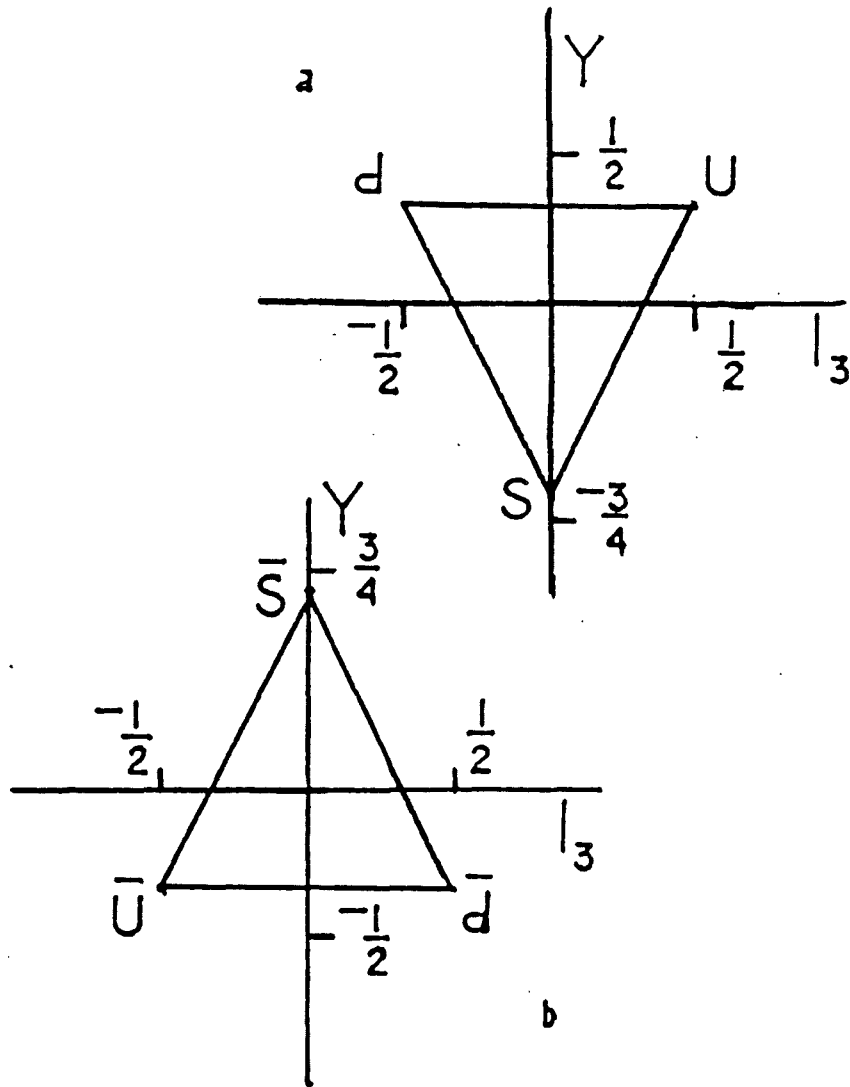
FIG. 2. Flavor representations of up, down, and strange quarks (a), and the corresponding antiquarks (b), in $SU(3)_F$

However, the naive uuu quark assignment of the $\Delta^{++}$ resonance, with isospin $\frac{3}{2}^{+}$ and spin $\frac{3}{2}^{+}$, violates the Pauli exclusion principle. A variety of postulates were examined, including the breakdown of spin statistics (parastatistics) for quarks, before it was concluded that quarks carry an additional quantum number, resolving this problem.

Quantum chromodynamics is based upon the postulate that this new quantum number is the "charge" of the strong force. The example of the $\Delta$ (and other experimental evidence, including the $\pi^{0}$ decay rate and the hadronic production cross-section in $e^{+}e^{-}$ reactions) shows that three distinct charges are involved. Further, this "charge" is not observed directly in hadrons, indicating that the three charges exactly neutralize each other. Consequently, QCD is based on the assumption that the three independent, equal charges are the basis vectors of the $\underline{3}_C$ representation of a local $SU(3)_C$ symmetry -- the subscript C indicating reference to the symmetry group of QCD rather than to the "flavor" $SU(3)_F$ (global) which parameterizes the distinctive identities of the quarks, as postulated by Gell-Mann, Ne'eman, and Zweig. It is noted that the same group is observed in either case; the subscript appears only as a convenience to the reader.

The charge of the strong force is called color, in analogy to the three primary colors (red, blue, and green). In this analogy, neutral states are "white," or "color singlets," as they arise only in the $\underline{1}_C$ representation of $SU(3)_C$. Antiquarks have the three anticolors (respectively, cyan, yellow, and magenta) of the $\underline{3}^{*}$ representation of $SU(3)_C$. The quanta of the color field are called gluons, and the gluons appear in an $\underline{8}_C$ representation as shown in Fig. 3.
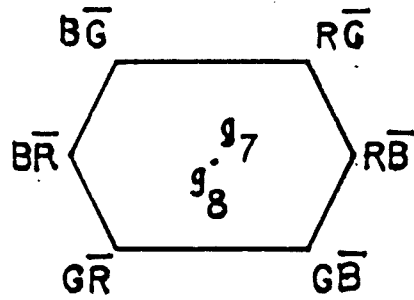
$$g_7 = \left( R\bar{R} - G\bar{G} \right) / \sqrt{2}$$

$$g_8 = \left( R\bar{R} + G\bar{G} - B\bar{B} \right) / \sqrt{6}$$

FIG. 3.   SU(3)$_C$ gluon octet

The group $SU(3)_C$ yields a non-Abelian (non-commutative) symmetry. The permitted vertices involving quarks and gluons are shown in Fig. 4. As can be seen, one vertex involves a quark, an antiquark, and a gluon ($q\bar{q}g$), in analogy to the $e^+e^-\gamma$ vertex in quantum electrodynamics. However, vertices involving three gluons and four gluons are also permitted; this is the physical manifestation of the appearance of charged force-exchange quanta. This complication accounts in part for the difficulty in the experimental verification of QCD. In addition, the sheer strength of the strong force severely inhibits the utility of perturbative quantum field theory. Perturbative quantum field theory (PQFT) permits the definition of an effective, or "running," coupling constant in renormalization theory. The running coupling constant is an estimate of the correction for higher order perturbative effects not included to given order in the theory. The running coupling constants for the strong force, the electromagnetic force, and the weak force are shown in Fig. 5. The strong force is seen to get relatively stronger at lower energy, the realm including the processes by which scattered quarks form complete baryons and mesons (hadronization). Because of this strengthening, the phenomenology of hadronization processes and of the low-energy baryon and meson spectra is poorly understood.

B. Meson Spectroscopy

As shown in Fig. 1, the ordinary and strange pseudoscalar mesons occur in an $\underline{8} \pm \underline{1}$ (nonet) of $SU(3)_F$. This pattern persists for all allowed spin-orbital angular momentum combinations, since only the nonet is available for ordinary quark-antiquark combinations in $SU(3)_F$ ($\underline{3} \times \underline{3}* = \underline{8} \pm \underline{1}$). The spectrum of presently observed mesons is shown in Table I. The relevant quantum numbers of meson states are:

q

a $\qquad$ g

$\bar{q}$

b

c
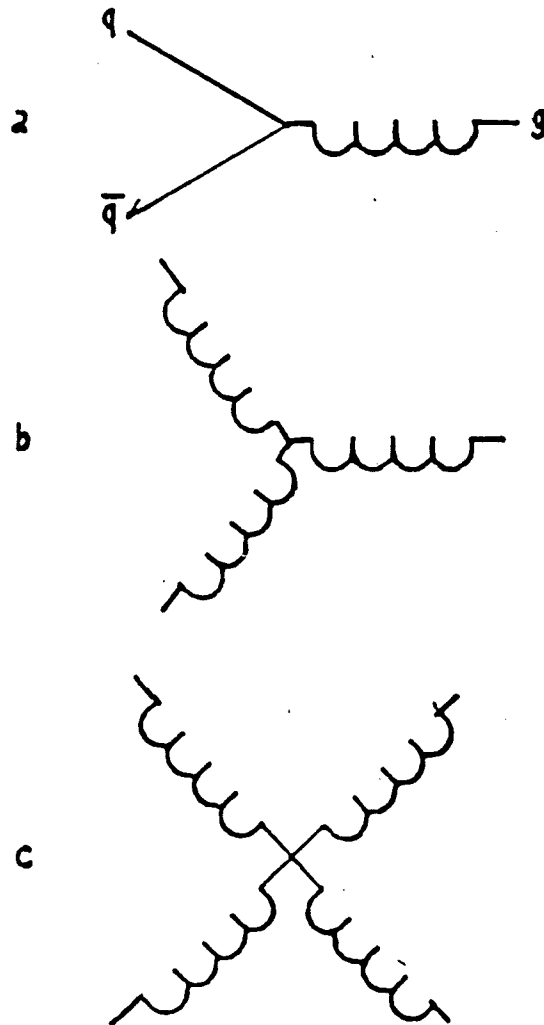
FIG. 4. SU(3)$_C$ QCD vertices for quarks and gluons (a) q$\bar{\text{q}}$g vertex (b) Three-gluon vertex (c) Four-gluon vertex
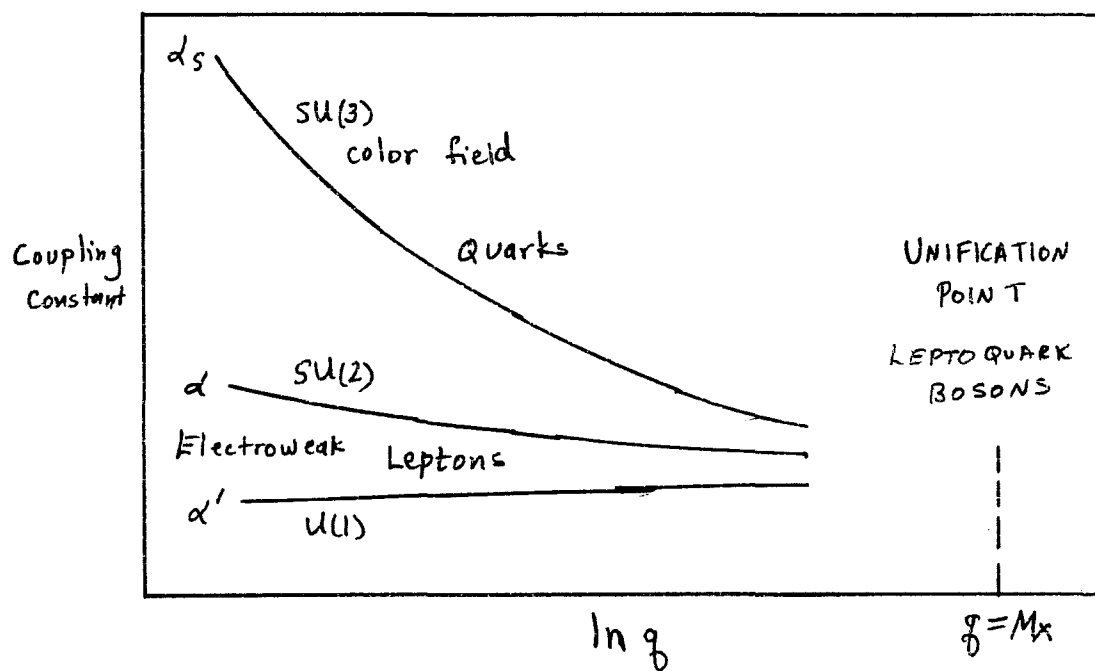
FIG. 5. Running coupling constants for the strong, electromagnetic, and weak forces

TABLE I

SELECTED MESON STATES

| MESON | $I^G(J^{PC})$ | MASS $GeV/c^2$ | WIDTH $GeV/c^2$ | QUARK CONTENT |
|---|---|---|---|---|
| $\pi$ | $1^-(0^{-+})$ | 0.13496 | stable | uu,dd,ud |
| $\eta$ | $0^+(0^{-+})$ | 0.5488 | stable | uu,dd |
| $\rho$ | $1^+(1^{--})$ | 0.770 | 0.153 | uu,ud |
| $\omega$ | $0^-(1^{--})$ | 0.783 | 0.010 | uu,ud |
| $\eta'$ | $0^+(0^{-+})$ | 0.958 | 0.0002 | uu,ss |
| $f_0$ | $0^+(0^{++})$ | 0.975 | 0.033 | uu(?) |
| $a_0$ | $1^-(0^{++})$ | 0.983 | 0.054 | uu,ud(?) |
| $\phi$ | $0^-(1^{--})$ | 1.020 | 0.004 | ss |
| $h_1$ | $0^-(1^{+-})$ | 1.190 | 0.320 | uu |
| $f_0$ | $0^+(0^{++})$ | 1.300 | broad | uu,dd,ss |
| $\eta$ | $0^+(0^{-+})$ | 1.440 | 0.076 | uu(?) |
| $\rho$ | $1^+(1^{--})$ | 1.590 | 0.260 | uu,ud(?) |
| $f_2$ | $0^+(2^{++})$ | 1.716 | 0.134 | uu(?) |
| $\eta_C$ | $0^+(0^{-+})$ | 2.981 | 0.011 | cc |
| $J/\psi$ | $0^-(1^{--})$ | 3.0969 | stable | cc |
| $\psi'$ | $(1^{--})$ | 3.770 | 0.025 | cc |
| K | $1/2(0^-)$ | 0.498 | stable | us,ds |
| $K^*$ | $1/2(1^-)$ | 0.896 | 0.051 | us |
| $K_2$ | $1/2(2^-)$ | 1.770 | 0.200 | us |
| $K_4^*$ | $1/2(4^+)$ | 2.060 | 0.210 | us |
| D | $1/2(0^-)$ | 1.865 | stable | uc,dc |
| $D_S$ | $0(0^-)$ | 1.971 | stable | cs |

Total quark spin $\underline{S}$, 0 (singlet) or 1 (triplet).

Quark orbital angular momentum $\underline{L}$.

Total angular momentum, $\underline{L} + \underline{S} = \underline{J}$.

Parity, $P = (-1)^{L+1}$.

Charge conjugation, $C = (-1)^{L+S}$.

Following standard spectroscopic notation, the states may be referred to as $^{2S+1}L_J$, where the letters S, P, D, F . . . stand for L = 0, 1, 2, 3 . . .. Thus, the singlet L = 0 mesons ($\pi$, K, $\eta$) are in the $^1S_0$ state, the triplet states ($\rho$, $\omega$, $K^*$, and $\phi$) in the $^3S_0$ states, etc. Alternatively, mesons may be identified by the notation $J^P$, with little ambiguity; thus, the singlet L=0 states are $0^-$, the triplet L=0 states $1^-$, etc.

Due to the previously discussed breakdown in QCD phenomenology at low energy, and due to the relativistic nature of calculations involving the light (u, d, and s) quarks, the detailed meson spectroscopy of the light-quark mesons is almost impossible to calculate. The results of one of the best mass models to date[21] are shown in Table II. However, although masses of the mesons are difficult to calculate, the mass differences between pseudoscalar and higher spin mesons with the same flavor content is calculable from the Regge theory. The K meson Regge trajectory, showing the theoretical and experimental masses of the $s\bar{u}$ and $s\bar{d}$ meson resonances, is shown in Fig. 6.

Of interest here are the strange mesons, mesons containing an s or $\bar{s}$, and those mesons containing an $s\bar{s}$ pair. The strange meson spectrum, as it is currently believed to exist, is shown in Fig. 7. The known isoscalar $s\bar{s}$ states are shown in Fig. 8. In the latter case, it is

W

13

## TABLE II

### MESON MASS FIT PRODUCED BY ONE-PARAMETER POTENTIAL[a]

| NAME | EXPT. $GeV/c^2$ | FIT $GeV/c^2$ | NAME | EXPT. $GeV/c^2$ | FIT $GeV/c^2$ |
|---|---|---|---|---|---|
| $\Upsilon : b\bar{b}\ 1^3S_1$ | 9.460 | 9.488 | $\phi : s\bar{s}\ 1^3S_1$ | 1.020 | 0.972 |
| $\Upsilon : b\bar{b}\ 2^3S_2$ | 10.021 | 10.016 | $\phi': s\bar{s}\ 2^3S_1$ | 1.684? | 1.715 |
| $\Upsilon : b\bar{b}\ 3^3S_1$ | 10.351 | 10.345 | $S^*: s\bar{s}\ 1^3P_0$ | 0.975 | 1.127 |
| $\Upsilon : b\bar{b}\ 4^3S_1$ | 10.572 | 10.607 | $E : s\bar{s}\ 1^3P_1$ | 1.420 | 1.394 |
| $\Upsilon : b\bar{b}\ 1^3P_0$ | 9.872 | 9.855 | $f': s\bar{s}\ 1^3P_2$ | 1.515 | 1.521 |
| $\Upsilon : b\bar{b}\ 1^3P_1$ | 9.893 | 9.890 | $F^*: c\bar{s}\ 1^3S_1$ | 2.140 | 2.085 |
| $\Upsilon : b\bar{b}\ 1^3P_2$ | 9.913 | 9.916 | $F : c\bar{s}\ 1^1S_0$ | 1.970 | 1.959 |
| $\Upsilon : b\bar{b}\ 2^3P_0$ | 10.234 | 10.216 | $\rho : u\bar{u}\ 1^3S_1$ | 0.770 | 0.677 |
| $\Upsilon : b\bar{b}\ 2^3P_1$ | 10.251 | 10.241 | $\rho': u\bar{u}\ 2^3S_1$ | 1.620 | 1.555 |
| $\Upsilon : b\bar{b}\ 2^3P_2$ | 10.267 | 10.259 | $\delta : u\bar{u}\ 1^3P_0$ | 0.983 | 0.783 |
| $B : b\bar{u}\ 1^1S_0$ | 5.268 | 5.209 | $A_1: u\bar{u}\ 1^3P_1$ | 1.275 | 1.189 |
| $\psi : c\bar{c}\ 1^3S_1$ | 3.097 | 3.123 | $A_2: u\bar{u}\ 1^3P_2$ | 1.320 | 1.334 |
| $\psi : c\bar{c}\ 2^3S_1$ | 3.686 | 3.664 | $g : u\bar{u}\ 1^3D_3$ | 1.690 | 1.795 |
| $\psi : c\bar{c}\ 3^3S_1$ | 4.029 | 4.076 | $\pi : u\bar{u}\ 1^1S_0$ | 0.139 | 0.274 |
| $\chi : c\bar{c}\ 1^3P_0$ | 3.415 | 3.400 | $\pi': u\bar{u}\ 2^1S_0$ | 1.300? | 1.342 |
| $\chi : c\bar{c}\ 1^3P_1$ | 3.510 | 3.482 | $B : u\bar{u}\ 1^1P_1$ | 1.228 | 1.185 |
| $\chi : c\bar{c}\ 1^3P_2$ | 3.556 | 3.535 | $A_3: u\bar{u}\ 1^1D_2$ | 1.680 | 1.714 |
| $\psi : c\bar{c}\ 1^3D_1$ | 3.770 | 3.768 | $D^*: c\bar{u}\ 1^3S_1$ | 2.007 | 1.949 |
| $\psi : c\bar{c}\ 2^3D_1$ | 4.159 | 4.147 | $D : c\bar{u}\ 1^1S_0$ | 1.863 | 1.818 |
| $\psi : c\bar{c}\ 3^3D_1$ | 4.415 | 4.485 | $K^*: s\bar{u}\ 1^3S_1$ | 0.892 | 0.824 |
| $\eta_C: c\bar{c}\ 1^1S_0$ | 2.980 | 3.013 | $Q_1: s\bar{u}\ 1^3P_1$ | 1.280 | 1.284 |
| $\eta_C: c\bar{c}\ 2^1S_0$ | 3.590 | 3.598 | $K^*: s\bar{u}\ 1^3P_0$ | 1.423 | 1.421 |
| $\psi : c\bar{c}\ 1^1P_1$ | 3.455? | 3.497 | $K : s\bar{u}\ 1^1S_0$ | 0.496 | 0.515 |
| | | | $Q : s\bar{u}\ 1^1P_1$ | 1.280 | 1.297 |

[a]This table is consistent in terminology with Ref. 21, rather than with current usage
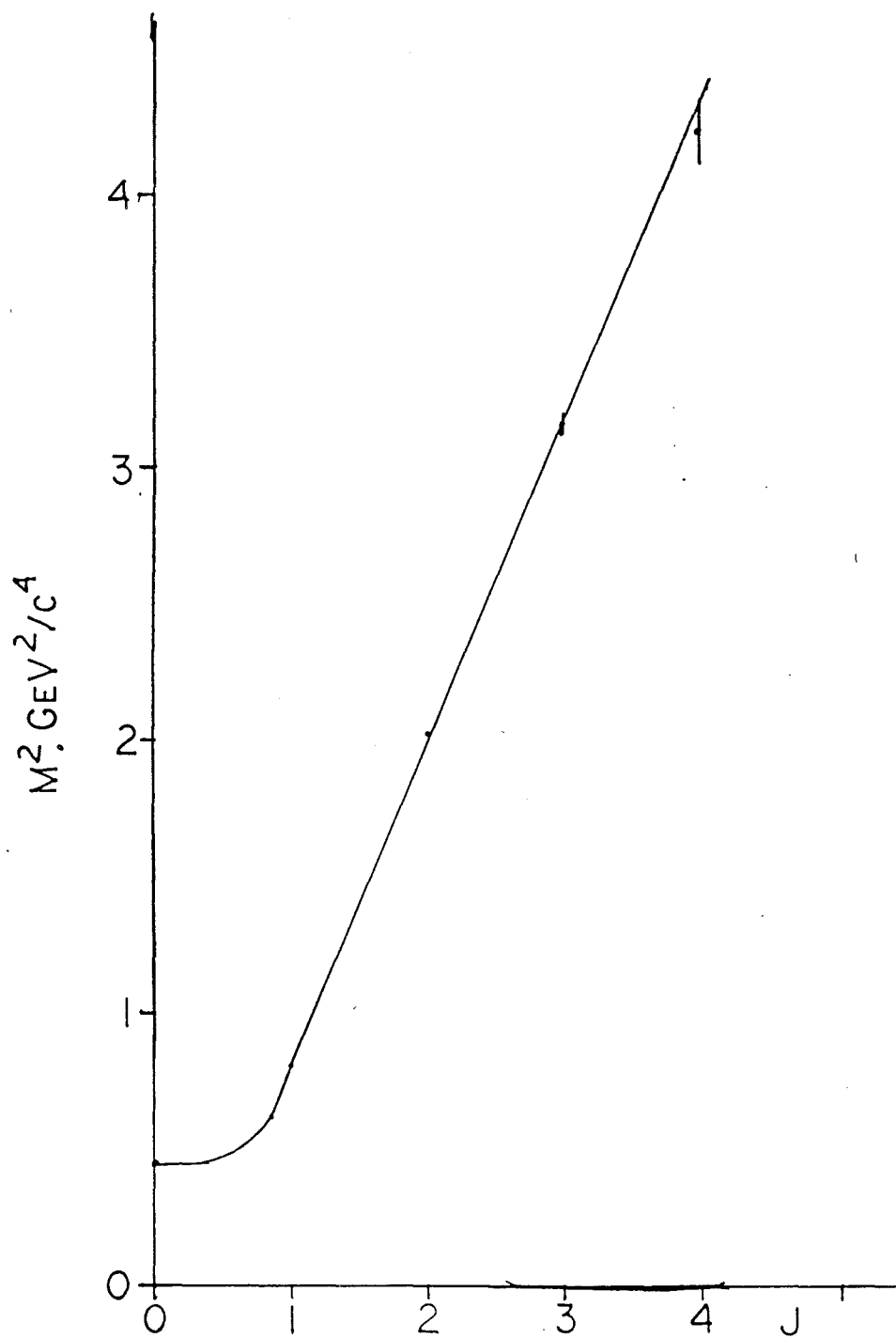
FIG. 6. K meson Regge trajectory and masses of strange resonances
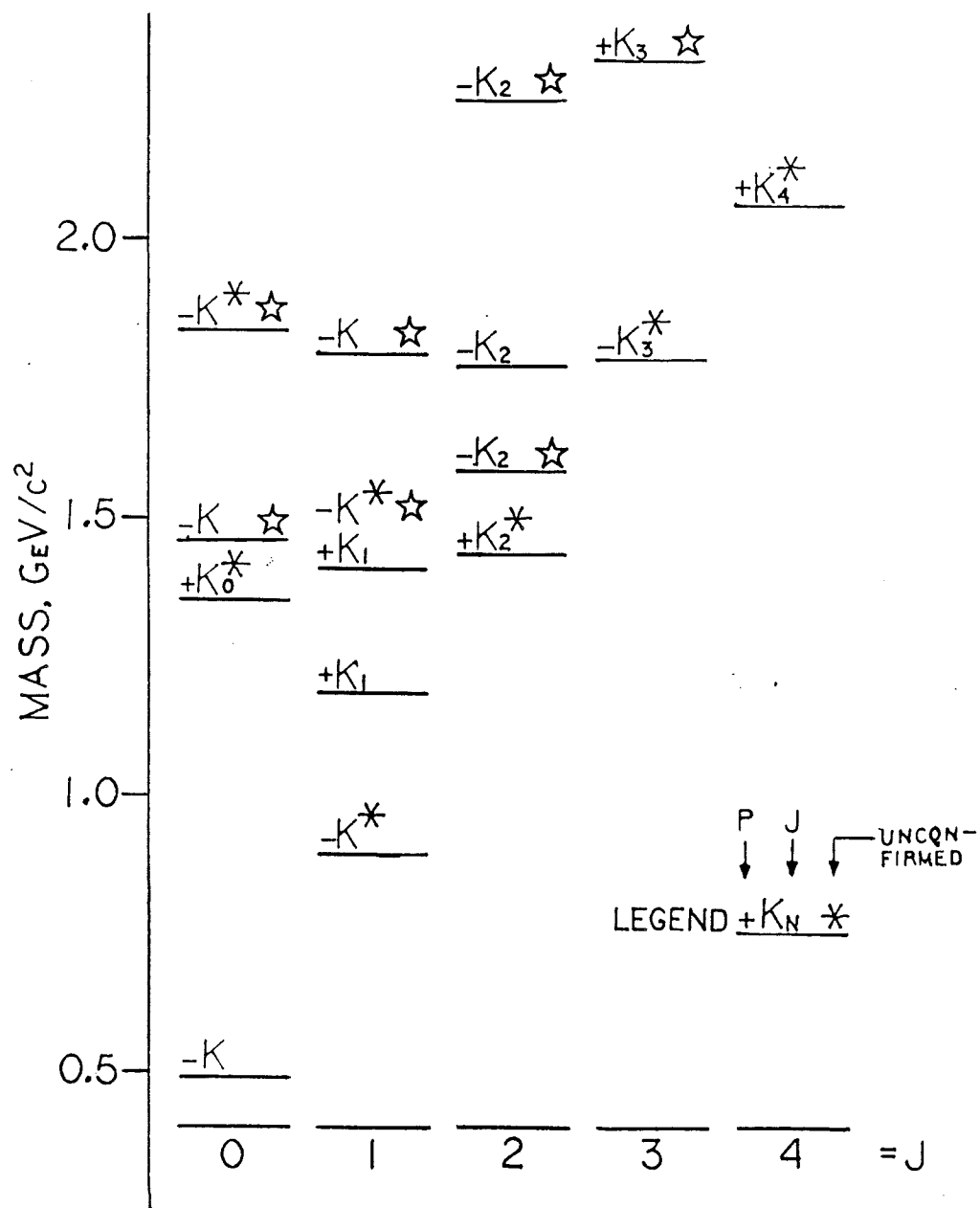
FIG. 7. Strange meson spectrum
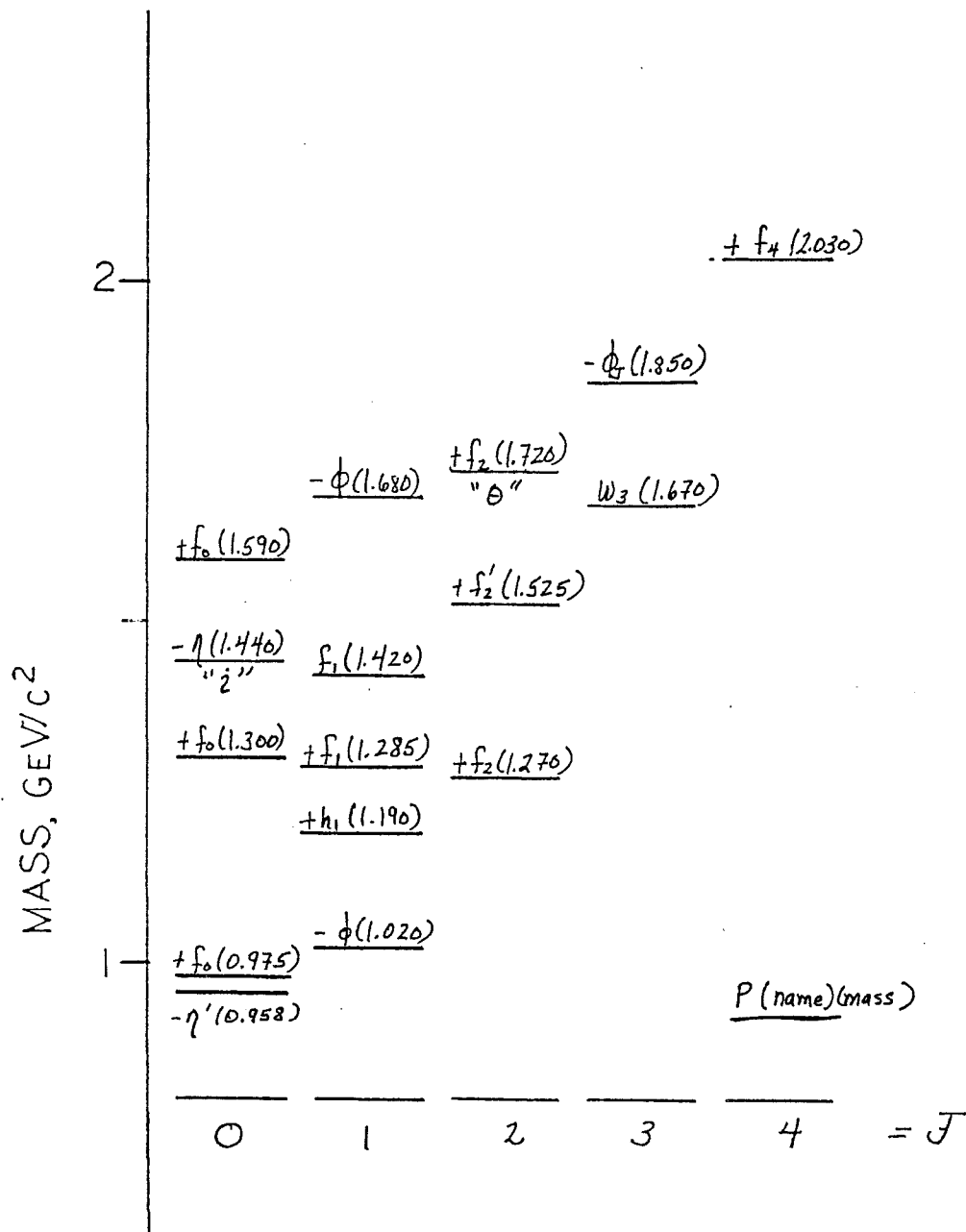
FIG. 8. Isoscalar mesons, including known or suspected s͞s states

believed that the $\eta$ and $\eta'$ contain admixtures of $s\bar{s}$ with $u\bar{u}$ and $d\bar{d}$, rather than being pure states. This is peculiar to the lighter quarks, as the charm and bottom quarks are sufficiently heavy to preclude significant pseudoscalar mixing. Another peculiarity lies in the mass of the $\phi$, which is slightly larger than the $K^+K^-$ threshold. Consequently, the $KK$ mode is open to the $\phi$, a state of affairs which does not hold for the $J/\psi$. This decay is shown in Fig. 9. A diagram of this form is known as a quark-flow diagram, as it shows the disposition of the quark currents during the hadronization process. Another $\phi$ decay mode is the $\pi^+\pi^-\pi^0$; the quark flow diagram for this decay is shown in Fig. 10. This process is of the type known as Zweig-suppressed (or OZI-suppressed, for Okubo-Zweig-Iizuka); none of the quarks in the initial particle appear in the final state. These processes are observed to occur two orders of magnitude less frequently than Zweig-allowed processes in which the quark currents flow from initial to final state.

Quark-flow diagrams for the production of strange particle states are shown in Figs. 11 - 13. Figure 11 shows the simplest hadroproduction mode of the $K^+$ in pp collisions, in pp --> $K^+\Lambda$p. This shows the conservation of the quark currents from the incident protons, and the production of the $s\bar{s}$ pair from the vacuum by coupling to a virtual gluon. Figure 12 shows the OZI-allowed production of a $\phi$ in pp --> $K^+\phi\Lambda$p. As seen here, the $s\bar{s}$ pair which forms the $\phi$ comes from the production of two $s\bar{s}$ pairs from the vacuum, with the additional strange quarks coupled to the up quark currents from the initial hadrons. Finally, Fig. 13 shows OZI-suppressed production of a $\phi\phi$ pair
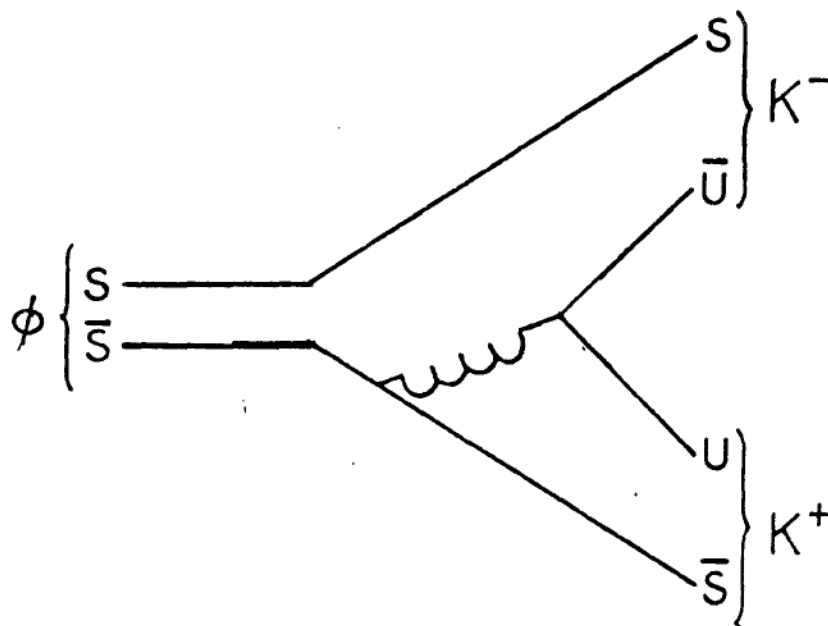
FIG. 9. $\phi \dashrightarrow K^+K^-$ decay
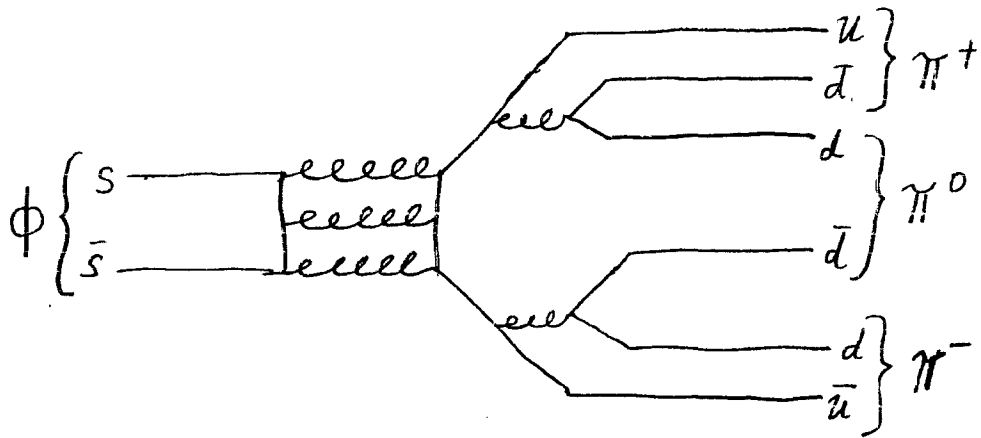
FIG. 10. $\phi \longrightarrow \pi^+\pi^-\pi^0$ decay
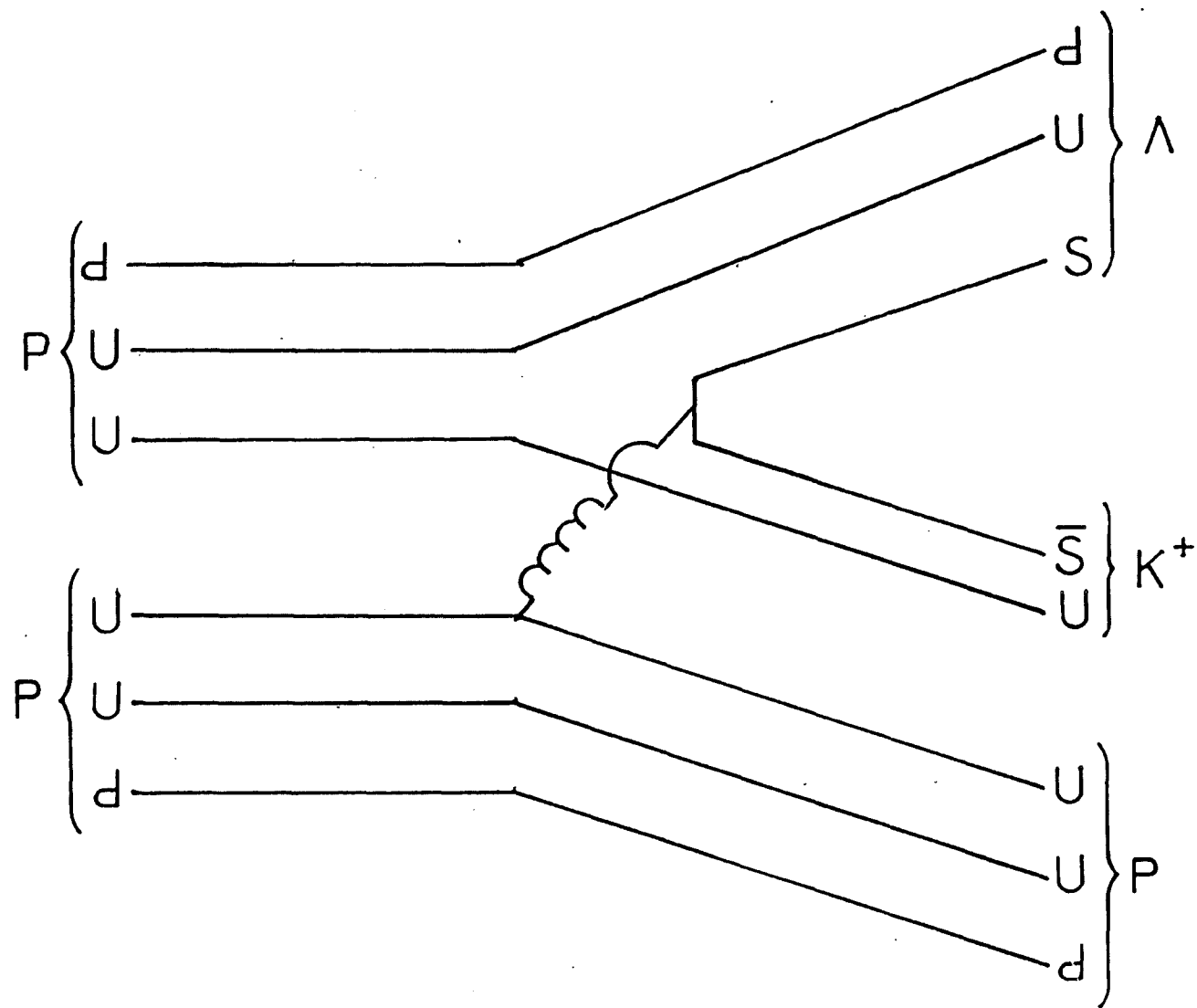
FIG. 11. Kaon hadroproduction in pp --> $K^+\Lambda p$
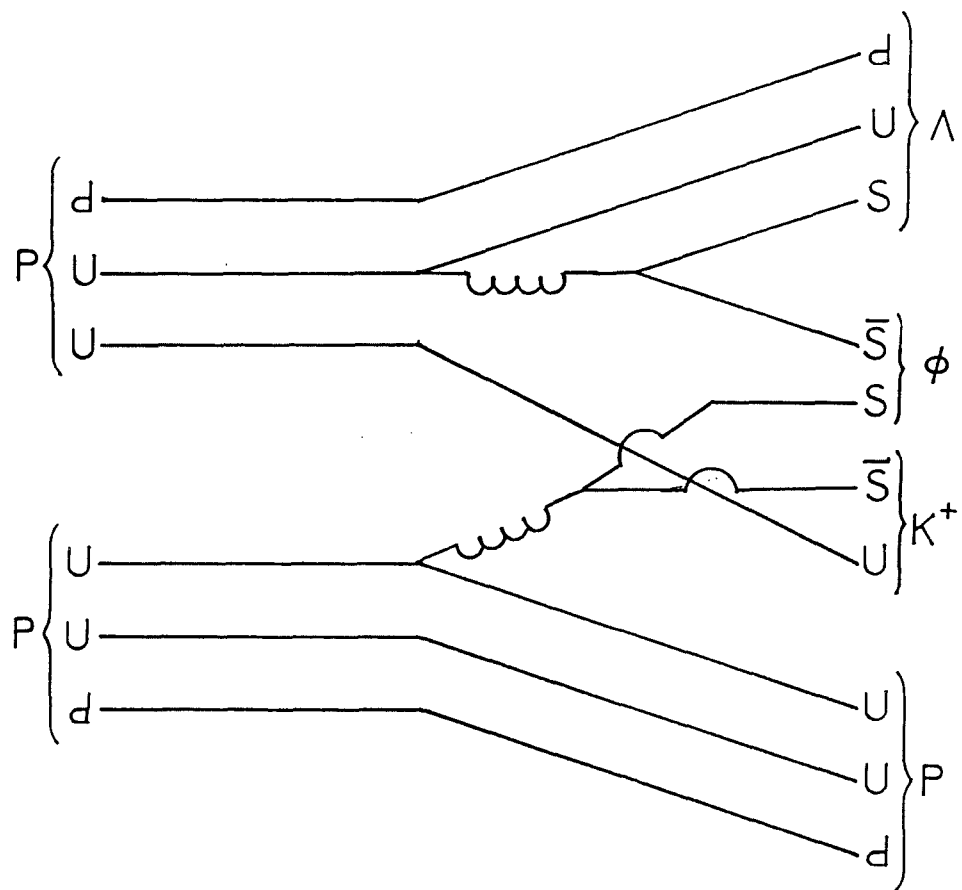
FIG. 12.   OZI-allowed $\phi$ hadroproduction in pp $-->$ K$^+\phi\Lambda$p
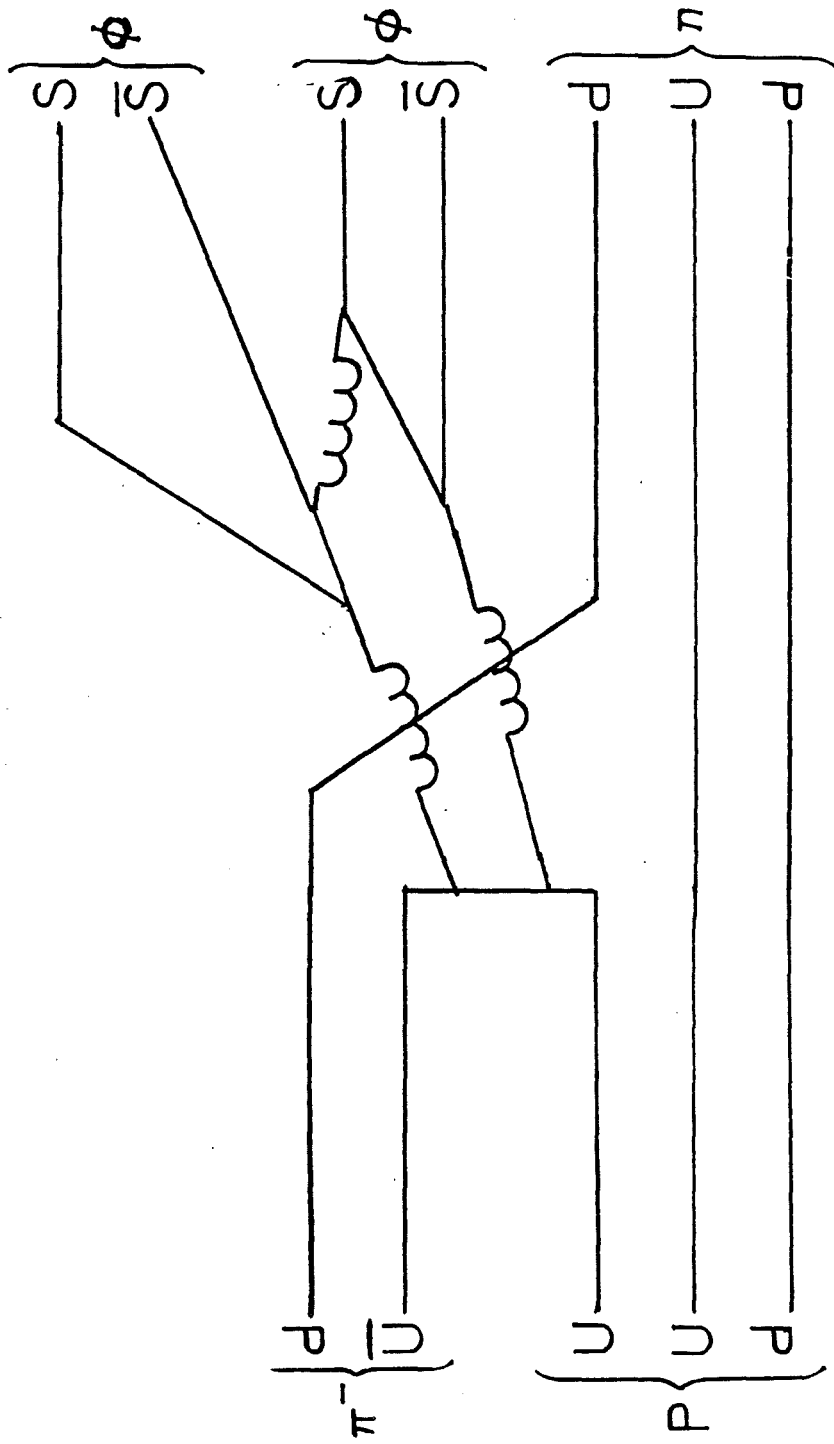
FIG. 13. OZI-suppressed $\phi\phi$ production in $\pi^- p \longrightarrow \phi\phi n$

in $\bar{\pi} p \longrightarrow \phi\phi n$. This reaction will be discussed in more detail later, as enhancement of the $\phi\phi$ spectrum in the reaction is considered an important signature of glueball production.

As the hadronic mass spectrum is poorly understood, so are the hadronic decay rates and resonance widths. The problems involved are illustrated graphically in Fig. 14, which shows one possible decay tree of the $K_2(1.770)$. The accessibility of intermediate resonance states, the effects of forbidden or suppressed intermediate states, and the difficulty of analyzing high-spin states with low production cross-sections against large backgrounds for the final state and intermediate states all contribute to the difficulties of hadronic resonance studies. There are, however, some recent indications[22] that anomalously narrow F wave (1 = 3) resonances may exist in the 2.0-2.5 $GeV/c^2$ range.

C. Charmed Meson Production

As the Weinberg-Salam-Glashow theory of quark identity ("flavor") matured, one of the most significant problems to arise was in the area of neutral current interactions. The theory predicted a neutral gauge boson, the $Z^0$ discovered at CERN in 1983. This boson mediates the weak neutral current. Early theoretical models containing the $Z^0$ predicted a strangeness-changing neutral current which would be evidenced by such processes as $K_S^0 \longrightarrow \mu^+\mu^-$. Non-observation of such processes led Glashow, Iliopoulas, and Maiani in 1970 to postulate the existence of a new flavor of quark. The contribution of this quark to the weak neutral current, of charge $+\frac{2}{3}e$ like the up quark, cancels the strangeness-changing neutral current. This theory was spectacularly

$K_2^-$ { $\overline{U}$ $S$

$\overline{U}$

$U$

$\pi^o$

$\overline{U}$ } $\pi^o$ $U$

$\underbrace{K_2^*(1.430)^-}$

$\overline{U}$ } $\pi^+$ $d$

$\overline{d}$ } $\overline{K}^o$

$\underbrace{K^*(0.892)^-}$

$S$
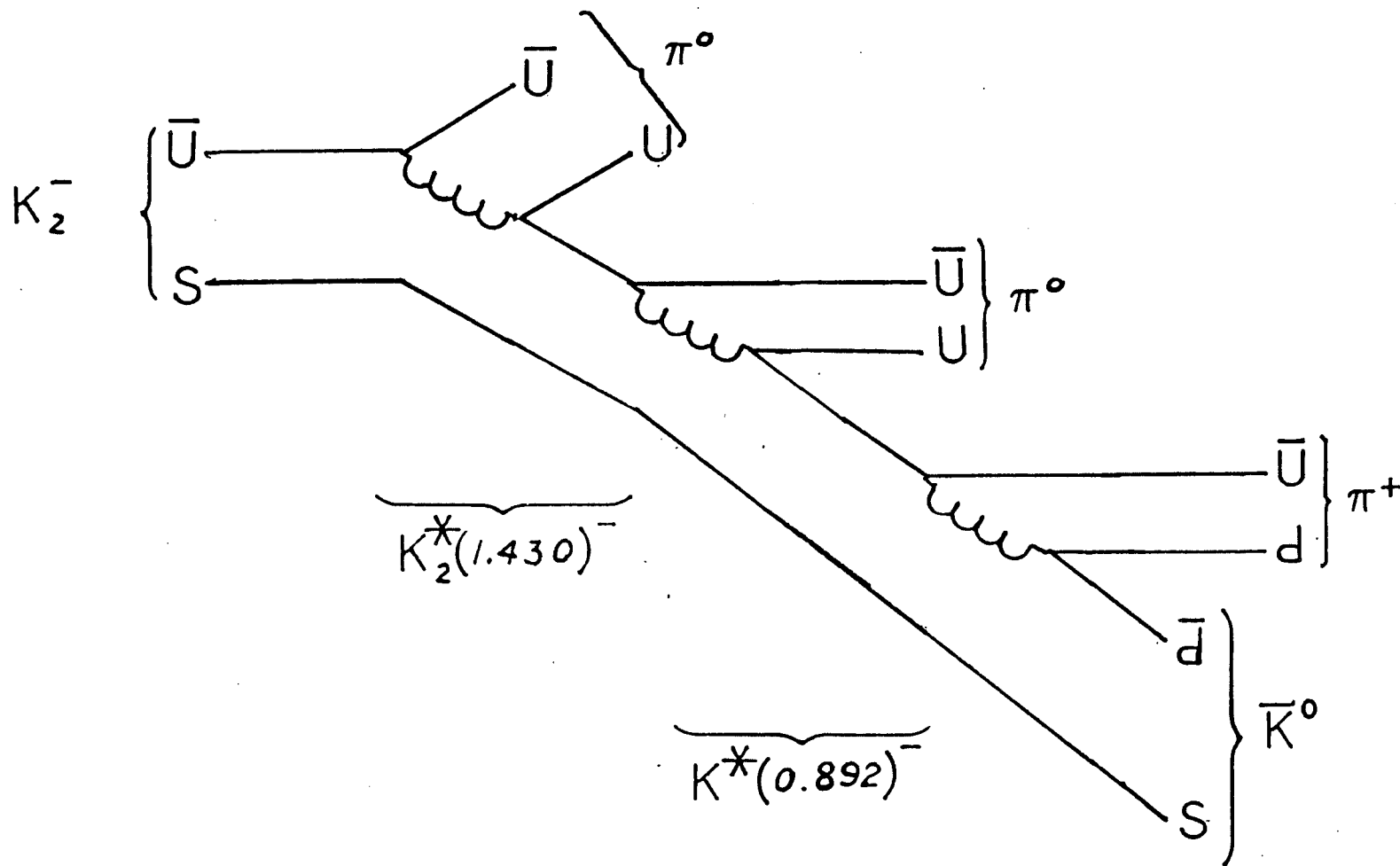
FIG. 14. Likely decay tree for $K_2(1.770)$

confirmed in 1974, when the J/ψ, later identified as the $^3S_1$ $c\bar{c}$ resonance, was reported by researchers at Brookhaven, using a hadron beam, and at Stanford, in $e^+e^-$ collisions, in the same week.

From measurements made primarily at $e^+e^-$ machines such as PEP at Stanford, the spectrum shown in Fig. 15 was eventually obtained. The $^3S$ states were all identified by direct coupling to $e^+e^-$ on production and decay. The other states were observed in the decay sequences of the $^3S$, usually in radiative decays by measurement of the associated γ. Of particular notice is the $3^3S_1$ ψ(3.770), which lies above $D\bar{D}$ threshold. This is the lightest $c\bar{c}$ state which permits OZI-allowed decay to charmed mesons. The lighter states, such as the J/ψ, can access only the OZI-suppressed decay modes shown in Fig. 16.

The known charmed mesons are shown in Fig. 17. These are shown in the 20 of SU(4), [Fig. 18] the smallest group including charmed meson states. Studies of these mesons are based almost entirely on $e^+e^-$ production of $c\bar{c}$ pairs. The hadronic production cross sections are uniformly low when compared to light quark cross sections,[23,24] and the problem of discriminating charmed events against the low-mass quark backgrounds has been successfully solved in only a few experiments. The present experiment sought, but failed to observe, the $η_C$ --> φφ decay (Fig. 19),[4,5] and identified the Cabibbo-suppressed decay $D^\pm$ --> φπ$^\pm$ (Fig. 20).[6,7]

D.  Exotic Meson States

As discussed above, presently observed hadrons are composed either of $q\bar{q}$ pairs or of three-quark/three-antiquark combinations, occurring in the singlet $\underline{1}_C$ representation of SU(3)$_C$; that is, observable hadrons are
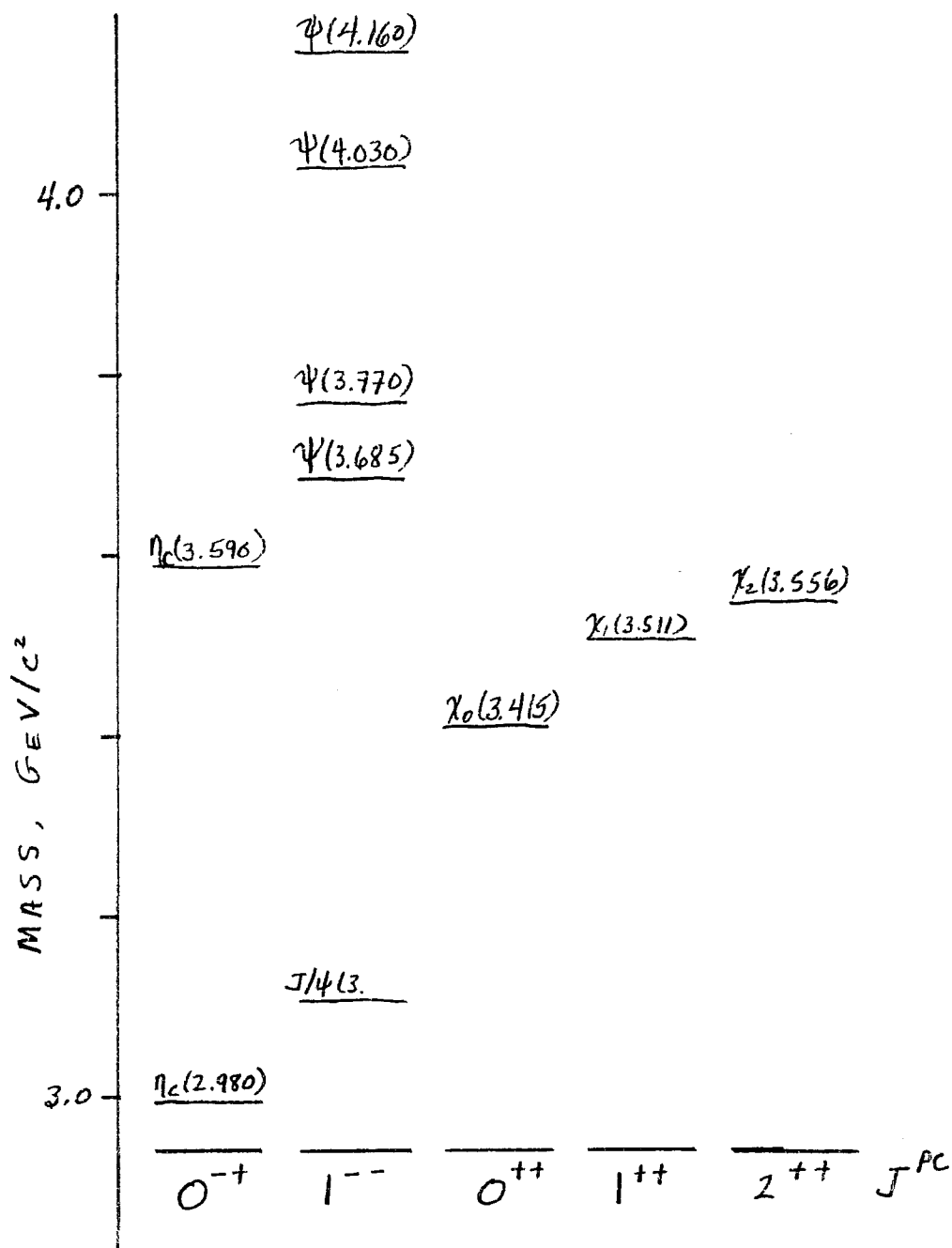
FIG. 15. Charmonium (c̄c) spectrum
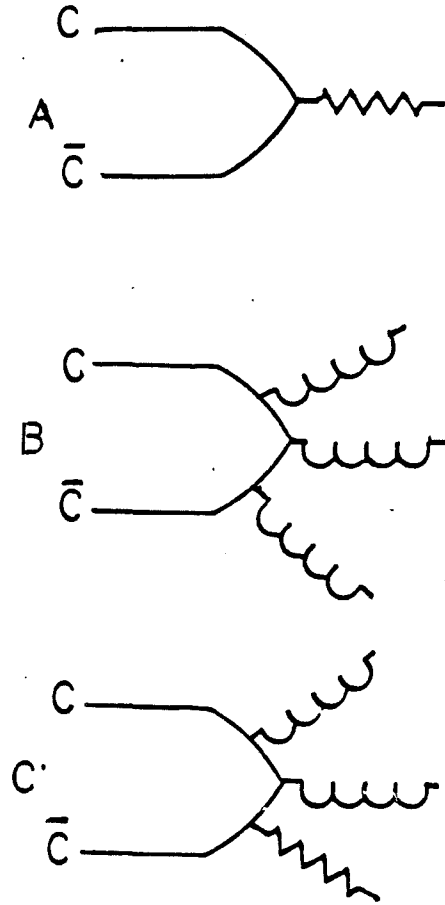
FIG. 16. OZI-suppressed decay modes of the J/ψ (a) Electromagnetic decay (b) Three-gluon decay (c) Radiative (γgg) decay

MASS, GeV/c²

1.4

2.2

2.0

2.2

2.0

1.8

D* ☆ ←UNCONFIRMED

Ds* ☆

-D*

-Ds

-D·

O    I    P    O    I
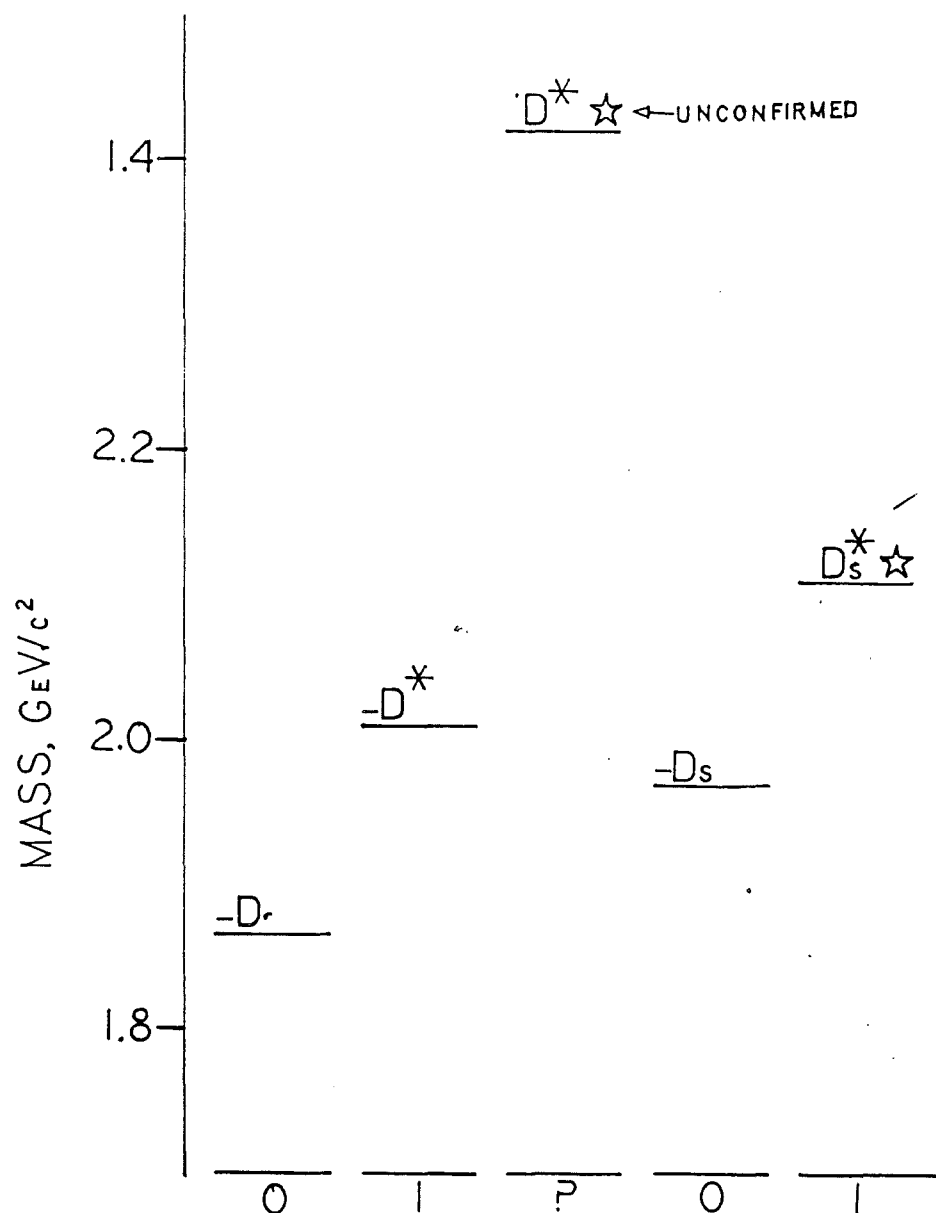
FIG. 17.   Charmed meson spectrum
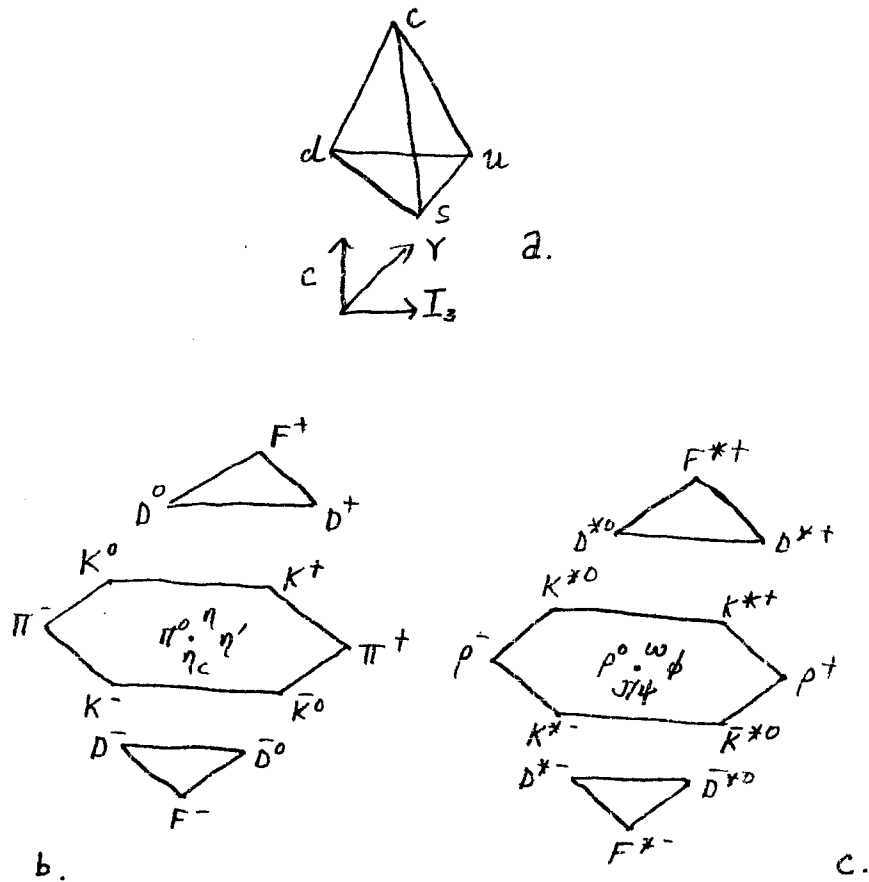
FIG. 18.  SU(4)$_F$ representations of charmed states  (a)  Fundamental

$\underline{4}$ showing quarks  (b)  $\underline{20}$ of pseudoscalar mesons (c) $\underline{20}$ of

vector mesons
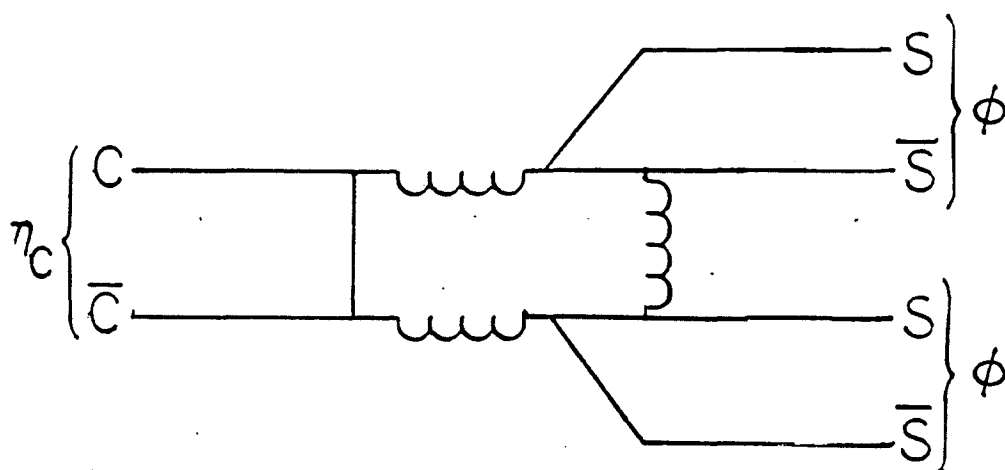
FIG. 19. $\eta_C \longrightarrow \phi\phi$ decay
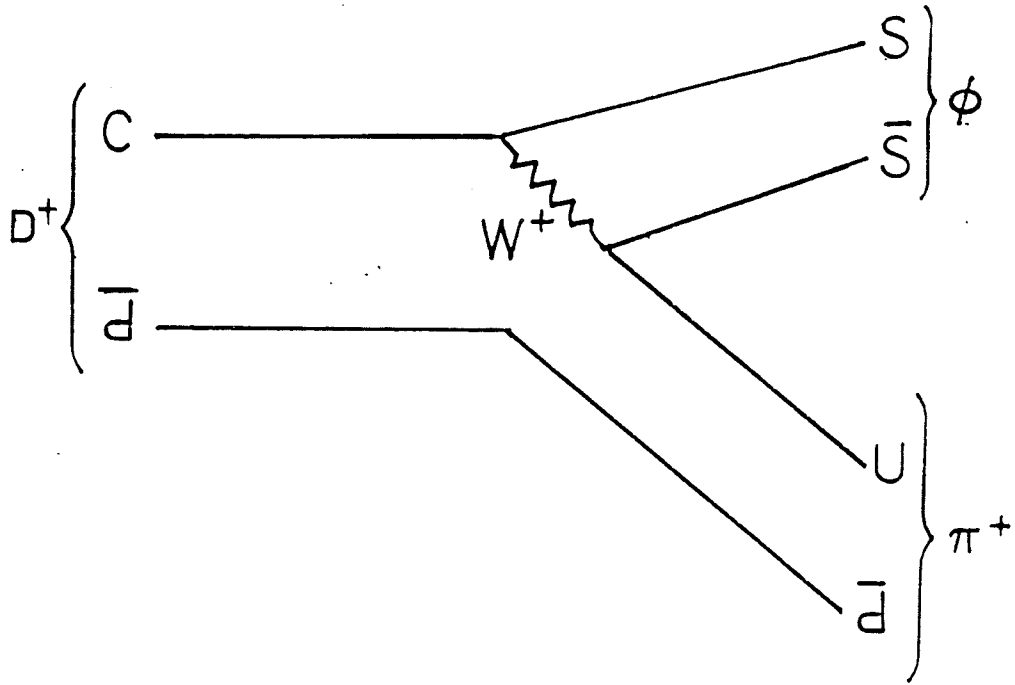
FIG. 20. The Cabibbo-suppressed decay $D^{\pm} \longrightarrow \phi\pi^{\pm}$

"colorless." It remains possible that states exist both as color combinations described by higher dimensional representations of $SU(3)_C$ (for example, unbound quarks in a $\underline{3}$ or unbound gluons or color octet $q\bar{q}$ mesons in an $\underline{8}$) and as color singlets with more than three quarks or antiquarks. Any combination of quarks which yields a color singlet and which is consistent with all other conservation laws should yield experimentally observable states. Some candidates are:

a) The dibaryon, a color singlet state with six quarks. The simplest dibaryon candidate is the deuteron, a bound state of neutron and proton. Some models for the deuteron suggest that $\sim 6\%$ of its wavefunction is in the form of a single-quark bag,[25] the least massive member of a low-lying dibaryon $\underline{10}^*$. A $\Lambda N$ resonance at 2.137 GeV is the candidate isodoublet member of this antidecuplet. However, it is suggested that this state might instead be an ordinary hypernucleus (a nucleus with one of the ordinary quarks replaced by a strange quark).[26] An experiment at CERN[27] has set an extremely low upper limit for the production cross-section of an expected $S = -2$ dibaryon state, the $H_2^-$. This upper limit lies well below the predicted cross-section for production of a $\Xi N$ dibaryon; the $\Lambda N$ is believed to be a hyperdeuteron rather than a six quark bag.

b) The baryonium, a color singlet $q^2\bar{q}^2$ or $q^3\bar{q}^3$ state which couples to a baryon-antibaryon pair, as by production in $\bar{p}p$ reactions. The composition varies in different production models, which assert that such states may be $q^2\bar{q}^2$ bags, a baryon-antibaryon state bound by nuclear forces, or a $q^3\bar{q}^3$ bag analogous to the dibaryon. The first baryonium candidate, the X(1.935),[28] was not confirmed to exist in

higher-statistics experiments.[29] It is now believed that baryonia, if they exist, cannot be distinguished from ordinary $q\bar{q}$ mesons in present experiments.[30]

c) The "hybrid" state of an ordinary meson or baryon coupled to a valence gluon. The term "valence gluon" refers to the possibility that a gluon may exist as a discrete quantum within a resonance, bound to the other particles within the hadron by gluon exchange. Only recently postulated,[31-34] no candidate states exist; it is believed that $q\bar{q}g$ states should lie ~ 300-500 MeV above the corresponding $q\bar{q}$ states.

d) The glueball, a state containing two or more valence gluons and no quarks in a color singlet combination. This is possible because gluons occur in a color octet, and two or more gluons may couple to form a color singlet. A number of two-gluon glueball candidate states have been suggested,[33,35-38] but it has not been proven that any of these states are other than ordinary mesons.

e) The exotic mesons of the form $q^2\bar{q}^2$. These are distinguished from the baryonia mentioned above because baryonia couple to baryon-antibaryon systems, having a quark pair in either a $\underline{3}^*$ or $\underline{6}$ representation of $SU(3)_F$ bound to an antiquark pair in a $\underline{3}$ or $\underline{6}^*$. An exotic meson is any $q^2\bar{q}^2$ state which is not formed in a baryon-antibaryon system, specifically those containing two $q\bar{q}$ pairs each in an $\underline{8}$ of $SU(3)_C$, with the four-quark combination in the color singlet of $\underline{8} \times \underline{8}$.[39] The experimental status of these exotic meson is confused; it is considered possible that the $J^P = 0^+$ nonet, $[a_0(0.980)$, $f_0(0.975)$, $K_0^*(1.350)$, $f_0(1.300)]$ is a low-lying $0^+$ $q^2\bar{q}^2$ state[13] rather than the $^3P_0$ $q\bar{q}$ nonets, or is a combination of the two. No $q^2\bar{q}^2$ states

have been unambiguously identified, but a nonet of $J^{PC} = 2^{++}$ $q^2\bar{q}^2$ states is predicted in the range 1.5-2.0 GeV, and a $2^{++}$ 36-plet of states in the range 1.5-2.25 Gev.[13,39-42] Some of the glueball candidate states may be members of one of these exotic multiplets.[40-41] This is particularly true of the candidate states $f_2(2.120)$, $f_2(2.240)$, and $f_2(2.390)$.

E. Glueballs

In 1980, a significant signal was detected at a mass of 1.440 GeV in $K\bar{K}\pi$ from the radiative decay $J/\psi \dashrightarrow \gamma K\bar{K}\pi$. Labeled $\eta(1.440)$, this $0^{-+}$ resonant state sparked a search for electrically neutral hadronic resonances with integral spin which do not fall into known meson nonet and which decay into states with no net flavor; these are the two definite signatures of a state composed solely of gluons.[33]

The $J/\psi$ and those of its excited states which fall below the threshold for decay into charmed mesons are considered to be especially likely states for the formation of two-gluon glueballs in their radiative decays. As was shown in Fig. 16, $J/\psi$ and $\psi'$ decays can proceed in three modes: annihilation into a single intermediate photon, which couples to $e^+e^-$ or $q\bar{q}$; annihilation into three gluons (necessary to conserve parity, angular momentum, and color) with coupling to hadrons; or annihilation into one photon with two gluons. This radiative mode is particularly likely to give rise to glueball candidates. In the radiative decay of the $J/\psi$, any glueball with two gluons, with mass less than the $J/\psi$ mass, and with accessible spin-parity may be formed before coupling to particle-antiparticle pairs. These states may be identified by the occurrence of a single

photon in conjunction with any combination of two or more particles with no net flavor. Two other glueball candidates are the $2^{++}$ $f_2(1.720)$, discovered in the radiative decay $J/\psi \longrightarrow \gamma\eta\eta$, and the $X(2.220)$, seen in radiative $J/\psi$ decay with a $\gamma K\bar{K}$ final state.

The observation of glueball candidates in hadronic interactions is more difficult than in $J/\psi$ radiative decay, because the signatures are not as clear, the backgrounds are worse, and the reaction dynamics favor OZI allowed processes. The only hadronic production experiment to produce glueball candidates to date was reported by Etkin et al[35-37] in the exclusive reaction $\pi^- p \longrightarrow \phi\phi n$ at 22 Gev/c. With a 4000 event sample, a partial wave analysis of the $\phi\phi$ system has revealed three states, the $f_2(2.120)$, $f_2(2.240)$, and $f_2(2.390)$. A summary of the experimental properties of these states is given in Table III. Lindenbaum considers these three states to be glueball candidates, because the $\phi\phi$ final state occurs in an exclusive channel with all ingoing flavor coupled to the final state neutron; the $\phi\phi$ pair can only be produced by the OZI suppressed reaction of Fig. 13. These $\phi\phi$ events were triggered on exclusive four kaon production against a recoil neutron. The $\phi\phi$ was significantly enhanced over uncorrelated four kaon events and over $\phi KK$, and the three resonances were observed with little background. Enhanced production in an OZI suppressed channel is indicative of an anomalous process, such as the formation of an intermediate glueball.

Most of these glueball candidates have been observed in only one decay channel. Further, this channel always contains either a strange particle and its antiparticle or two particles with hidden strangeness.

TABLE III

EXPERIMENTAL PROPERTIES OF BNL $\phi\phi$ STATES

| $I^G(J^{PC}) = 0^+(2^{++})$ | | |
|---|---|---|
| STATE | MASS $GeV/c^2$ | WIDTH $GeV/c^2$ |
| $f_2(2.120)$ | $2.120 \begin{smallmatrix} +0.020 \\ -0.120 \end{smallmatrix}$ | $0.300 \begin{smallmatrix} +0.150 \\ -0.050 \end{smallmatrix}$ |
| $f_2(2.240)$ | $2.236 \pm 0.021$ | $0.166 \pm 0.035$ |
| $f_2(2.390)$ | $2.386 \pm 0.013$ | $0.188 \pm 0.045$ |

This is usually attributed to the presence of $SU(3)_F$ symmetry breaking;
because of the larger s quark mass, $s\bar{s}$ pairs are observed to be produced
less than half as often as $u\bar{u}$ or $d\bar{d}$ pairs.[43] Strange particle phase
space, and, consequently, the background, is smaller. It has been
suggested[32,33,44] on the basis of bag model calculations that some $2^{++}$
glueballs should couple almost exclusively to final states with two $s\bar{s}$
pairs, the $f_2(1.720)$ and the $f_2(2.120)$ family are examples.

## F.  Production of $q^2\bar{q}^2$ Exotic Mesons

The simplest mesonic system with more than three quarks is the
color singlet combination which contains two quarks and two antiquarks.
Since such a system has integral spin and baryon number zero, $q^2\bar{q}^2$
states have become known generically as exotic mesons. This is
particularly true of those combinations which have quantum numbers $J^{PC}$
inacessible to $q\bar{q}$ states.

As discussed above, it is possible (though not generally believed),
that the scalar nonet may be the low-lying $0^+$ $q^2\bar{q}^2$ nonet predicted by
Jaffe in 1977[13]. It may also be an admixture[10] of $q\bar{q}$ or $q^2\bar{q}^2$ elements.
This suggestion is predicated on three experimental facts:

a) The $f_0(1.300)$ is so broad as to preclude accurate mass or width
determination, with possible elements of the wave function extending
almost to zero mass[10]. $q^2\bar{q}^2$ states have available an "OZI superallowed"
decay mode due to crossing quark lines as shown in Fig. 21; such a
superallowed decay would explain the anomalies associated with this
state.

b) The $f_0(0.975)$ and $a_0(0.983)$ are very similar in mass, despite
the expectation that the isotriplet $a_0$ would be $\sim 0.200$ GeV/$c^2$ less
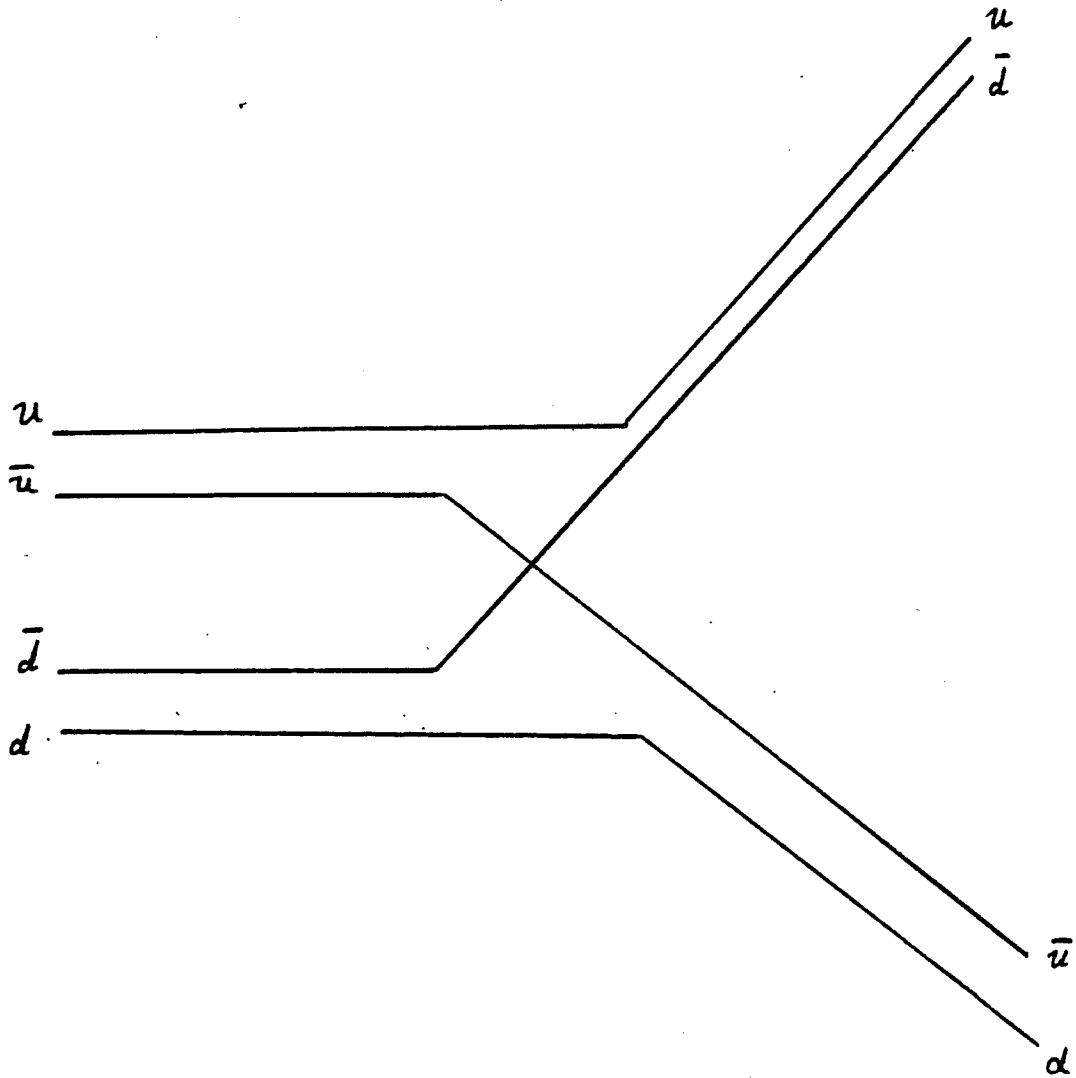
FIG. 21. OZI-superallowed decay of $q^2\bar{q}^2$ state

massive than the $f_0$ if the $a_0$ were the $^3P_0$ companion of the $\pi$[13,45] and the $f_0$ of the $\eta'$.

c) The mass difference between the $0^-$ and $1^-$ meson nonets demonstrates that most of the mass difference in the meson spectrum is due to spin-spin coupling rather than to spin-orbit coupling. Consequently Jaffe's scalar $q^2\bar{q}^2$ nonet is expected to exist at low mass, with the experimental nonet composed of exotic flavor combinations as shown in Table IV. The theoretical mass assignments in Table IV are from a bag model calculation.

Because of the anomalous features of the $f_0(1.300)$, it is difficult to discuss the relative spectroscopy of the states in this nonet. However, it has been demonstrated[10] that the spectroscopy of the scalar mesons can be explained by an admixture of virtual $q\bar{q}q\bar{q}$ pairs into a $q\bar{q}$ wavefunction. While this is possible, it does not explain why such effects are not observed in other systems.

There have been other predictions of $q^2\bar{q}^2$ states; particularly interesting are the results for $2^{++}$ $q^2\bar{q}^2$ states. Such states can occur in S-wave only if the diquark-diantiquark couple into two axial-vector systems, and the two $q\bar{q}$'s formed within the exotic state subsequently couple into vector mesons. Hence, in the OZI superallowed decays of $2^{++}$ exotic mesons, the double vector meson (VV) decay mode is expected to dominate if the resonance is above VV threshold. The lowest-lying $2^{++}$ exotic states are a nonet (with two or fewer s or $\bar{s}$ quarks, as in the $0^+$ nonet) and a 36-plet with up to four s or $\bar{s}$'s. The estimated masses of these states in the bag model are shown in Table V.

It is noteworthy that the $s^2\bar{s}^2$ is predicted to lie in the region of

TABLE IV

EXOTIC HYPOTHESIS FOR THE $0^+$ NONET

| FLAVOR | THEORETICAL MASS $GeV/c^2$ | STATE | EXPERIMENTAL MASS $GeV/c^2$ | EXPERIMENTAL WIDTH $GeV/c^2$ |
|---|---|---|---|---|
| $u\bar{u}d\bar{d}$ | 0.650 | $f_0(1.300)$ | $\sim 1.300$ | $0.150 - 0.400$ |
| $s\bar{s}(u\bar{u}+d\bar{d})$ | 1.100 | $f_0(0.975)$ | $0.975 \pm 0.004$ | $0.033 \pm 0.006$ |
| $u\bar{d}s\bar{s}$ | 1.100 | $f_0(0.980)$ | $0.983 \pm 0.002$ | $0.054 \pm 0.007$ |
| $u\bar{s}d\bar{d}$ | 0.900 | $K_0^*(1.350)$ | $\sim 1.350$ | $\sim 0.250$ |

TABLE V

BAG MODEL MASSES OF $2^{++}$ EXOTIC MESONS

| FLAVOR | PREDICTED MASS $GeV/c^2$ |
|--------|--------------------------|
| $u\bar{u}d\bar{d}$ | 1.600 |
| $u\bar{u}s\bar{d}$ | 1.750 - 1.800 |
| $u\bar{u}s\bar{s}$ | 1.900 - 1.950 |
| $u\bar{s}s\bar{s}$ | 2.050 - 2.100 |
| $s\bar{s}s\bar{s}$ | 2.200 - 2.250 |

the $f_2(2.120)$ family of states. This has lead Li and Liu[40-42] to infer that these states are the $s^2\bar{s}^2$ exotic. Li and Liu have developed a gluon vector dominance model (GVDM) in which $q^2\bar{q}^2$ states are formed to lowest order in perturbative QCD by the mechanism of Fig. 22. As shown, two gluons emitted by the initial hadronic system couple to two flavor-singlet vector mesons ($\omega$ or $\phi$) with $q\bar{q}$ pairs of necessity forming a color octet. These two "color octet vector mesons" combine to form the $q^2\bar{q}^2$ state, which decays directly by the OZI superallowed process. Such states are slightly above threshold for decay into two vector mesons according to the bag model mass calculation, so that threshold effects yield a width $\Gamma \simeq 100$-$200$ MeV for the resulting $q^2\bar{q}^2$'s. Li and Liu explain the spectroscopy of the Brookhaven states by postulating that the two octet $\phi$'s couple in $^5S_2$, $^1D_2$, and $^5D_2$ combinations, consistent with the results presented in Table III. The GVDM also predicts cross-sections for double vector meson production via an intermediate $q^2\bar{q}^2$ which are in good agreement with experimental cross-sections.

The $f_2(1.720)$ is consistent with the mass predictions for the $u\bar{u}d\bar{d}$, etc. families within the exotic $\underline{9} \pm \underline{36}$. However, the $f_2$ is observed only in $\eta\eta$ and $K\bar{K}$, while the preferred double-pseudoscalar decay mode of a $u\bar{u}d\bar{d}$ would be $\pi\pi$, regardless of a possible double vector meson decay mode. Hence Li and Liu identify the $f_2$ as a glueball. As candidates for the lowest lying $q^2\bar{q}^2$ states, they show[41,45] that the enhancement of $\rho^0\rho^0$ over $\rho^+\rho^-$ in both $J/\psi$ radiative decay and $\gamma\gamma$ production reactions may be an indication of interference between the nonet $2^{++}$ isosinglet and the $2^{++}$ 36-plet isotensor.
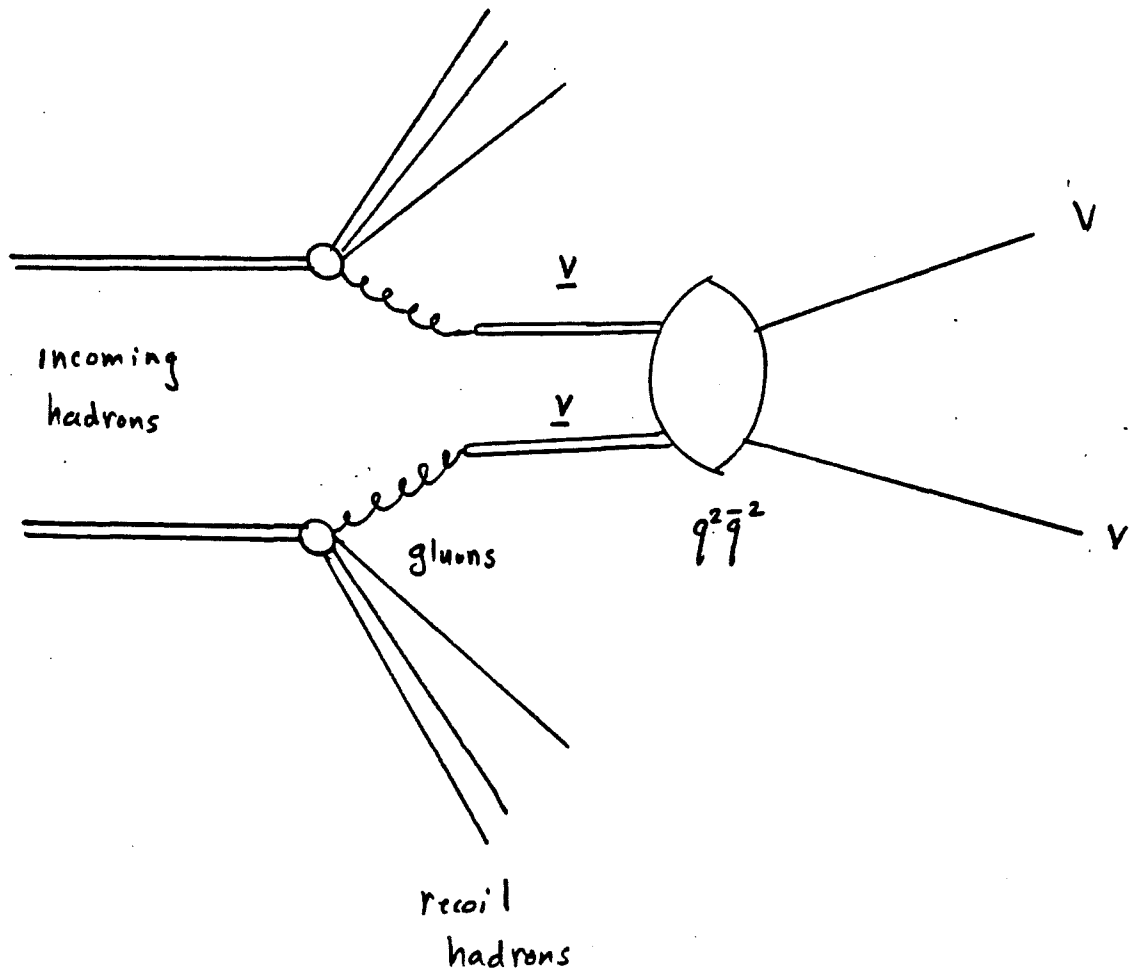
FIG. 22. GVDM model formation of $q^2\bar{q}^2$ state

One method for identifying the composition of candidate exotic states is an examination of other potentially accessible decay modes. As was discussed above, a $\bar{s}\bar{s}ss$ exotic with $J^{PC} = 2^{++}$ is expected to decay almost exclusively through OZI superallowed fragmentation into two $\phi$ mesons, since it is above threshold for such a decay. Consequently, if for example the $f_2(2.120)$ family were $s^2\bar{s}^2$ states, they would not be observed in decay modes other than $\phi\phi$ without very high statistics; the most likely candidates for such modes would be $\eta$ and $\eta'$ in the D wave. Other double-vector-meson channels would provide evidence for the existence of the remaining members of the $q^2\bar{q}^2$ $\underline{9} \pm \underline{36}$. In particular, the $K^{*0}\bar{K}^{*0}$ channel would provide evidence for the nonet and/or 36-plet states with $s\bar{s}$ coupled to a lighter $q\bar{q}$ pair, expected at a mass of $\sim 1.950$ GeV/c$^2$. It should be noted that one experiment[46] sees an enhancement in $K^{*0}\bar{K}^{*0}$ at this mass, but with very low statistics.

Conversely, any given glueball should couple to any kinematically accessible meson combination with the proper quantum numbers. Glueballs couple to all open hadronic channels, and are observed only when the background from other hadronic interactions in a channel is particularly small. This expectation is, however, in disagreement with the observation[44] that $2^{++}$ glueballs, formed of two noninteracting transverse magnetic gluons in a spherical cavity bag, couple to final states containing two $s\bar{s}$ pairs. Indeed, this result predicts coupling through $s\bar{s}$ to be enhanced to $\sim 25$ times the light quark couplings.

CHAPTER III

EXPERIMENTAL APPARATUS

The experiment was performed at the Fermilab Multiparticle Spectrometer (FMPS) facility, which was located in the M6W beamline at the time of the experiment. The FMPS is located 1850 feet downstream of the Meson West production target, which for this experiment was used to reduce the primary beam flux from $10^{11}$ 400 GeV/c protons per pulse to $1 - 3 \times 10^{6}$ protons per pulse at the experiment.

The laboratory coordinate system is shown in Fig. 23. The z direction paralleled the beam, and increased in the beam direction (downstream). The center of the coordinate system (x = 0, y = 0, z = 0) was defined to be the point at which the beam entered the spectrometer magnet aperture. The x-z plane was defined to be the plane of maximum curvature within the magnet, and x increased in the direction of curvature of a negatively charged particle. The y direction was defined so as to complete a right-handed rectilinear coordinate system. Within the lab, the setting of the apparatus was such that z increased to the north, x to the west, and y upward.

The spectrometer proper (Fig. 24) contained the following elements, given in order of increasing z:

a) Three stations (BA1, BA2, and BB) of multiple wire proportional chambers (MWPC), labeled BAY1 through BBY in Table VI. These chambers were used to define the trajectory of the interacting proton.

b) A veto counter to eliminate interactions by particles outside

45

$\hat{x}$

$\hat{z}$

$\hat{y}$

Front face of magnet

$z = 0$
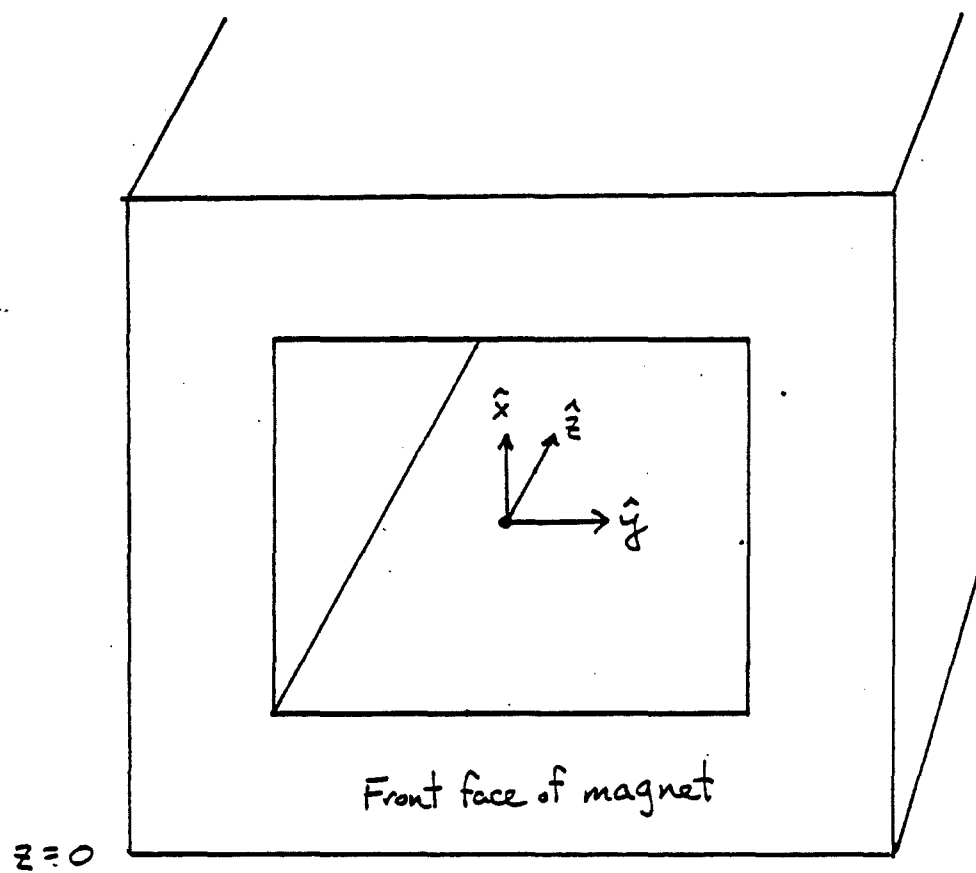
FIG. 23. Experiment laboratory coordinate system

Beam →

ST   A   B   C   $C_A$   Magnet   D   $C_B$   DA   DB   SC   F

$-2.0$   $-1.0$   $0.0$   $1.0$   $2.0$   $3.0$   $4.0$   $5.0$   $6.0$   $7.0$   $8.0$

Z (meters)
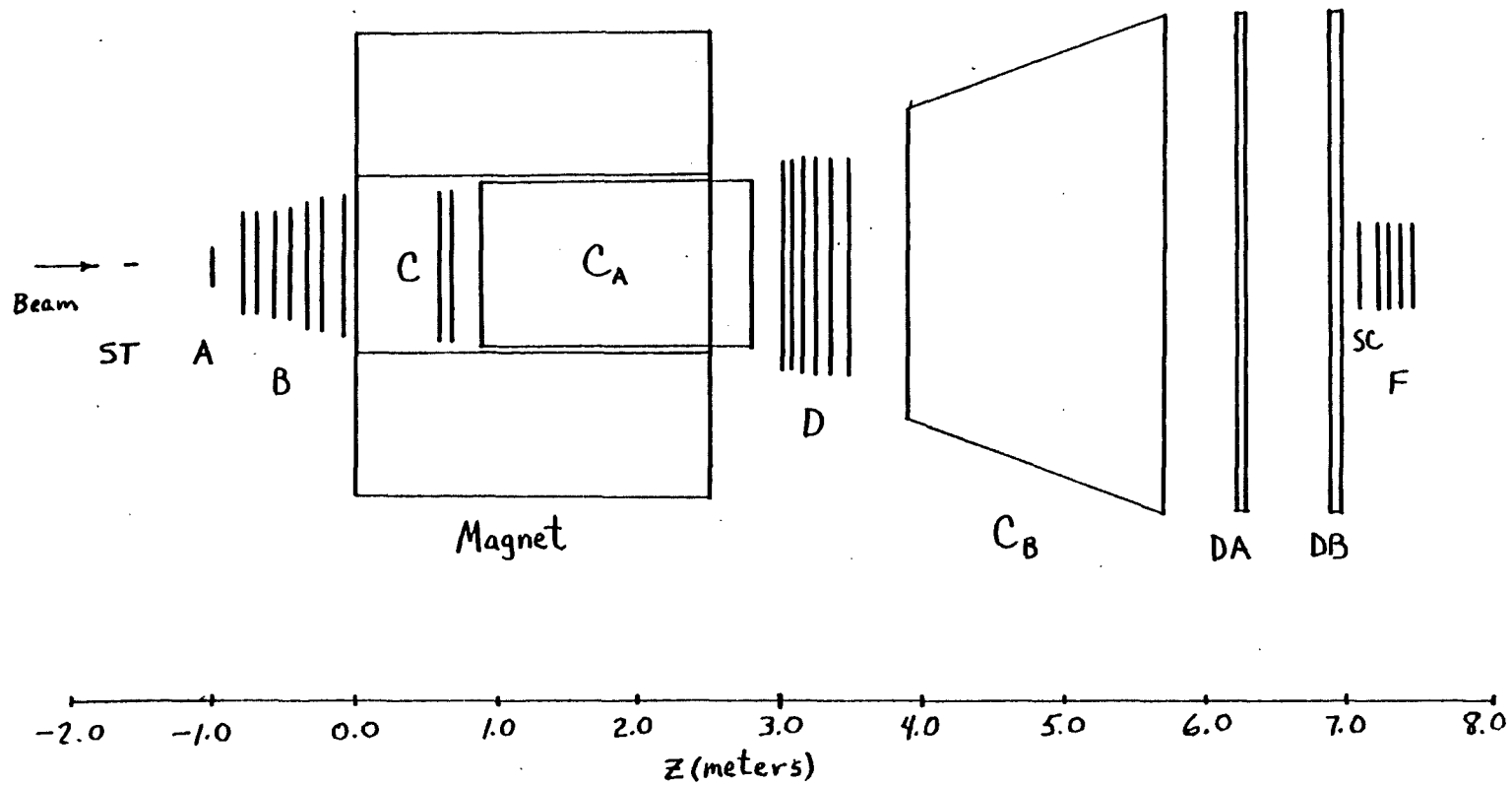
FIG. 24.   Configuration of FMPS

TABLE VI

E623 WIRE CHAMBERS

| NAME | SPACING mm | NUMBER OF WIRES | Z POSITION m | ANGLE deg |
|------|------------|-----------------|--------------|-----------|
| BA1X | 2.0 | 64 | -33.236 | 0 |
| BA1Y | 2.0 | 64 | -33.252 | 90 |
| BA2Y | 2.0 | 64 | -21.197 | 90 |
| BA2X | 2.0 | 64 | -21.182 | 0 |
| BA3V | 2.0 | 64 | -21.043 | 135 |
| BB2X | 1.0 | 32 | -2.185 | 0 |
| BB1X | 1.0 | 32 | -1.880 | 0 |
| BB1Y | 1.0 | 32 | -1.873 | 90 |
| AX1 | 1.0 | 256 | -1.054 | 0 |
| AX2 | 1.0 | 256 | -1.048 | 0 |
| AY1 | 1.0 | 256 | -1.043 | 90 |
| AY2 | 1.0 | 256 | -1.037 | 90 |
| AU | 1.0 | 256 | -0.968 | 45 |
| AV | 1.0 | 256 | -0.963 | 135 |
| BX1 | 2.0 | 384 | -0.813 | 0 |
| BY1 | 2.0 | 192 | -0.720 | 90 |
| BX2 | 2.0 | 384 | -0.572 | 0 |
| BY2 | 2.0 | 192 | -0.478 | 90 |
| BX3 | 2.0 | 448 | -0.362 | 0 |
| BY3 | 2.0 | 256 | -0.283 | 90 |
| BU | 2.0 | 448 | -0.081 | 27 |
| CX | 2.0 | 512 | +0.600 | 0 |
| CY | 2.0 | 320 | 0.676 | 90 |
| DX1 | 2.0 | 800 | 3.001 | 0 |
| DY1 | 3.0 | 320 | 3.088 | 90 |
| DU | 2.0 | 864 | 3.177 | 15 |
| DV | 2.0 | 864 | 3.298 | 165 |
| DY2 | 3.0 | 320 | 3.386 | 90 |
| DX2 | 2.0 | 800 | 3.475 | 0 |
| DAU | 18.3 | 192 | 6.198 | 17 |
| DAV | 18.3 | 192 | 6.217 | 163 |
| DAX1 | 19.0 | 176 | 6.236 | 0 |
| DAX2 | 19.0 | 176 | 6.255 | 0 |
| DBU | 18.3 | 192 | 6.910 | 17 |
| DBV | 18.3 | 192 | 6.929 | 163 |
| DBX1 | 19.0 | 176 | 6.948 | 0 |
| DBX2 | 19.0 | 176 | 6.967 | 0 |
| FX | 2.0 | 320 | 7.211 | 0 |
| FY | 2.0 | 320 | 7.291 | 90 |
| FU | 2.0 | 320 | 7.374 | 45 |
| FV | 2.0 | 320 | 7.455 | 135 |

the beam proper.

c) A target composed of twenty panels of plastic scintillator, yielding a total 10% interaction rate.

d) A scintillation counter (dE/dx), used by the trigger to identify interacting beam events.

e) Three stations (A, B, and C) of MWPCs to define the "upstream" leg of particle tracks, from the interaction point to the center of the spectrometer magnet. Station C was within the magnet aperture.

f) The spectometer magnet, with a $p_t$ kick of 0.697 GeV/c in the x - z plane. The upstream face of the magnet was defined to be z = 0.

g) A multicell threshold Cherenkov counter, CA, residing within the exit aperture of the magnet.

h) One station (D) of MWPCS to initiate downstream tracking.

i) A second multicell threshold Cherenkov counter, CB.

j) Two stations of high resolution drift chambers, DA and DB. These conclude the primary downstream tracking.

k) Between the drift chambers, a 1" x 1" (1 x 1) scintillator resided in the path of the non-interacting beam.

l) A 32 panel scintillator hodoscope, SCWALL.

m) A final station of MWPCs, F, centered on the dense near-axis region.

In addition, the experiment includes a hardware trigger processor which used x measurements performed at stations C, D, DB, CA, and CB to identify candidate events containing two low mass $K^+K^-$ pairs. This processor will be described at the end of the chapter. The hardware elements described above will first be discussed.

A. The Beam

With the FNAL accelerator running at 400 GeV/c, the M6W beam line can provide either a proton beam with $p \leq 400$ GeV/c, or a pion beam of useful intensity with $p \leq 250$ GeV/c; in this experiment, a 400 GeV/c proton was used. The momentum resolution of the beam was 0.5%. At this beam energy, the contamination of the beam by other charged species is negligible. The beam spot was an oval with a FWHM of 2.0 cm in X and 0.5 cm in Y, and a mean angle of incidence of 2.5 mrad. The purpose of the eight planes of beam MWPC's was to measure the trajectories of individual interacting beam particles for kinematic calculations. With a one second pulse delivering an average of $2 \times 10^6$ protons per pulse, the mean separation of beam particles was 0.5 $\mu$s, and of interactions was 5.0 $\mu$s. This separation effectively eliminated coincidences and spurious counts due to multiple interactions.

B. The Target

The target for this experiment was an active, or "smart," target composed of twenty segments of plastic scintillator enclosed in aluminum foil and paper. Each segment was $3.172 \pm 0.003$ cm in height and width, and $0.621 \pm 0.006$ cm in thickness, giving a total target length of $13.619 \pm 0.056$ cm.

The smart target was designed to provide secondary interaction identification by measuring changes in particle multiplicity between segments. This would be used to identify, for example, three-prong charm decays within the target. Analysis of target data revealed that the change in scintillator photoelectron yield was, by itself, insufficient to permit secondary identification. Consequently, the

target data were not used in the analysis except for the location of the primary vertex.

## C.  Tracking Chambers

Tracking was provided by 25 planes of MWPC's and the 8 drift chamber planes.  A MWPC plane is a parallel array of anode wires at positive high voltage, with solid sheet cathode planes on either side. Ionization events in the gas yield electrons, which are directed to the anode wire by the prevailing electric field.  Secondary electrons are generated by the passage of electrons through the gas, yielding an electron avalanche near the anode wire and converted into a current pulse.  The estimated position of the track in the MWPC is the known wire position.  The position uncertainty is usually taken to be the mean wire separation divided by the square root of twelve, as would be obtained for a uniform distribution across the wire separation distance. A typical MWPC is shown in Fig. 25.

The most significant problem encountered in the analysis of MWPC data is that of clustering.  If a particle passes approximately halfway between two anode wires, some electrons will be attracted to each wire. yielding measurable pulses in both.  Taken in isolation, this should decrease the uncertainty of such a point on the particle track. However, the same effect is observed for a variety of other reasons. Two or more adjacent wires may fire due to the passage of particles through adjacent cells, production of delta rays or other energetic secondary phenomena, background radiation (including coincident interactions), and spurious firing.  A common method of handling clusters is to use the cluster center position and to increase the

*Typical MWPC (E623)*

*particle direction*

*Cathode planes*
*V ≅ -3500V*

*Signal wires*
*V ≅ 0*

*2mm*
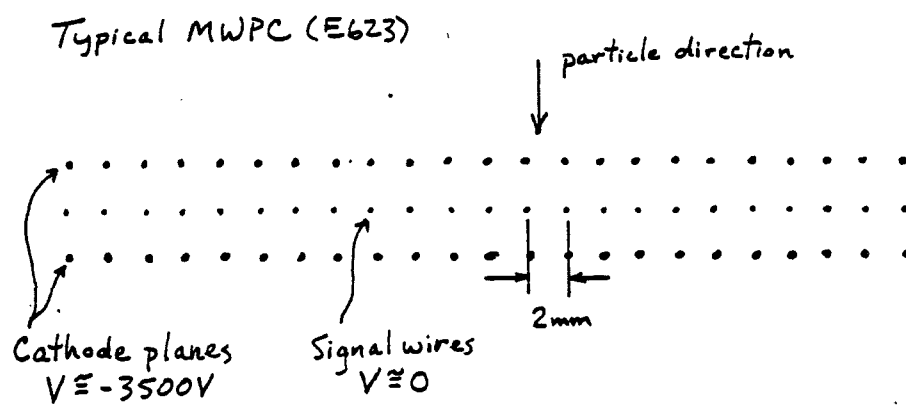
FIG. 25. Typical MWPC configuration

uncertainty of the clustered hit to (total cluster width)/(square root
of twelve). Analysis of reconstructed tracks shows that wide clusters
tend to contain two reconstructed tracks, particularly in the upstream
chambers.

As seen in Fig. 26, the basic operating principle of the drift
chamber is similar to that of the MWPC. Arrays of cathode and anode
wires form an electric field which causes charge collection on the anode
wires. In the drift chamber, however, the time of flight is used to
provide an accurate position measurement, on the order of 350 microns.
Drift chamber parameters are also given in Table VI.

Since separate tracking in (x - z) and (y - z) is, by itself,
insufficient to match the projections to define a track in space, one
third of the chambers measure "u" or "v" directions at some acute angle,
clockwise or counterclockwise respectively, from the x axis, facing
downstream. The angle of these chambers are given in Table VI. The use
of this information in track finding and track fitting will be discussed
in the next chapter.

The elements of the tracking system described here, together with
knowledge of the primary interaction vertex obtained from the beam
chambers and target, are sufficient to provide an angular resolution of
0.5 mrad in y and upstream x, and of 0.3 mrad in downstream x. Using
the vertex point for tracking and the known $p_t$ kick of the magnet, we
obtain a track momentum error of

$$\frac{\sigma_p}{p} = 0.0009 \ p[GeV/c] \ ( \ 1 \ + \ p^2[GeV/c]/35^2 \ )^{1/2}$$
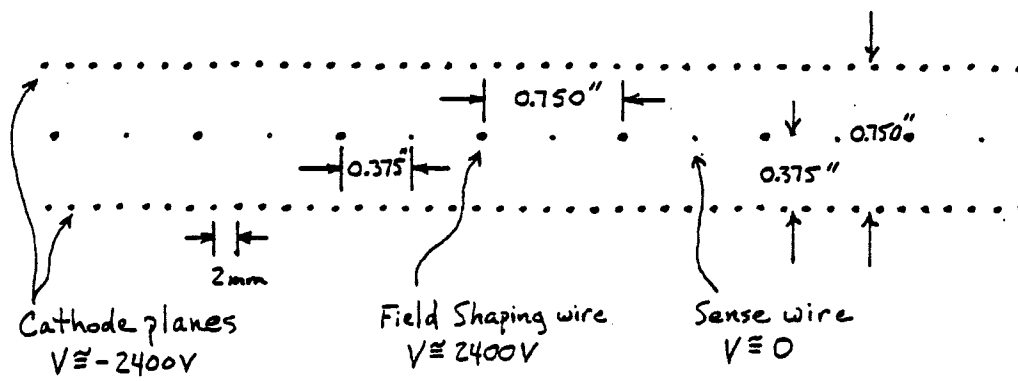
FIG. 26. Typical drift chamber configuration

## D. Spectrometer Magnet

The FMPS spectrometer magnet is a ferrite superconducting magnet producing a centrally homogeneous magnetic field of 1.7 T at its maximum excitation of 180 amps. The aperture of the magnet is 1.20 m in x and 0.8 m in y. The length of the magnet is 2.54 m.

## E. Cherenkov Counters

Two multicell threshold Cherenkov counters were used during the data collection. Both of these counters contained $N_2$ at atmospheric pressure as the excitation medium. Deviations of chamber temperature and pressure from STP were insignificant. The expected photon yields for protons, kaons, and pions, as a function of particle momentum, are shown in Fig. 27. The cell arrangement of CA is shown in Fig. 28, and of CB in Fig. 29.

Due to the curvature of particles in the magnetic field, the cone of radiation emitted by a given relativistic particle typically swept across several cells of CA. Consequently, CA was used only as a multiplicity veto in the trigger, and was not used for particle identification. CB was used in the particle identification process, which is discussed in more detail in chapter IV.

## F. Scintillator Hodoscope

The scintillator wall (SC WALL) was located downstream of CB to aid in the separation of pions and kaons in the crowded central region of the spectrometer. As shown in Fig. 30, it consisted of 32 elements, arranged in an array of four rows and eight columns centered on the x - z axis of the spectrometer. The eight columns were each 7.62 cm
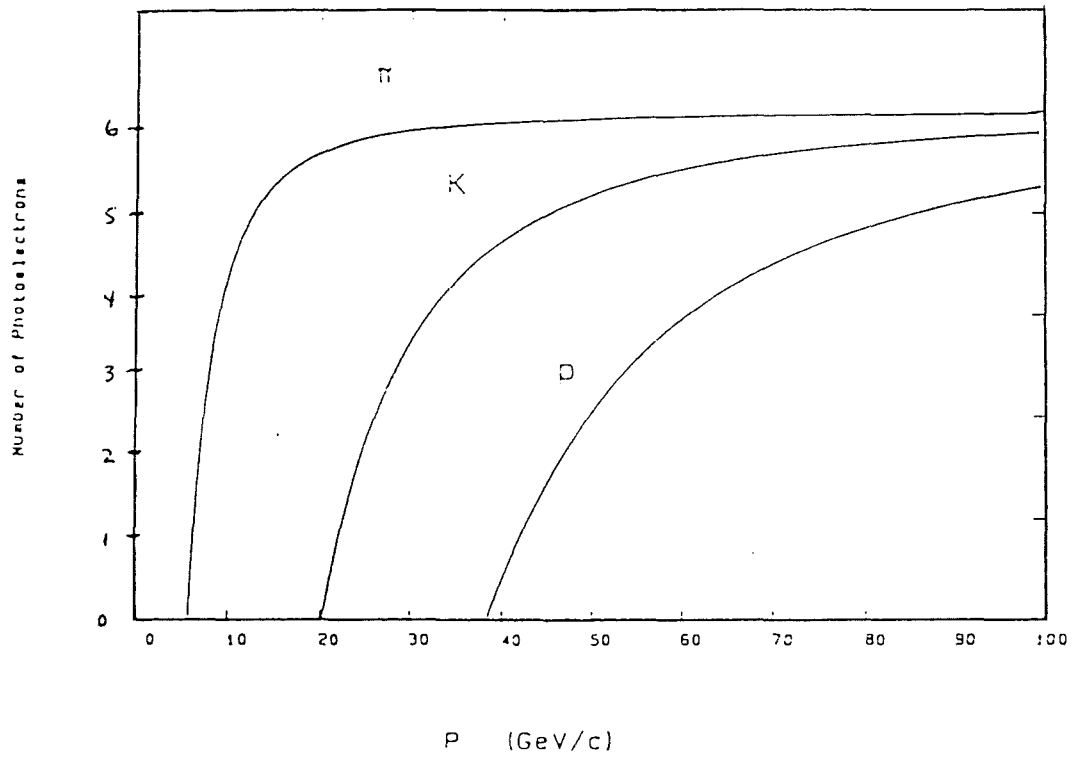
FIG. 27. Expected photon yield in Cherenkov counters
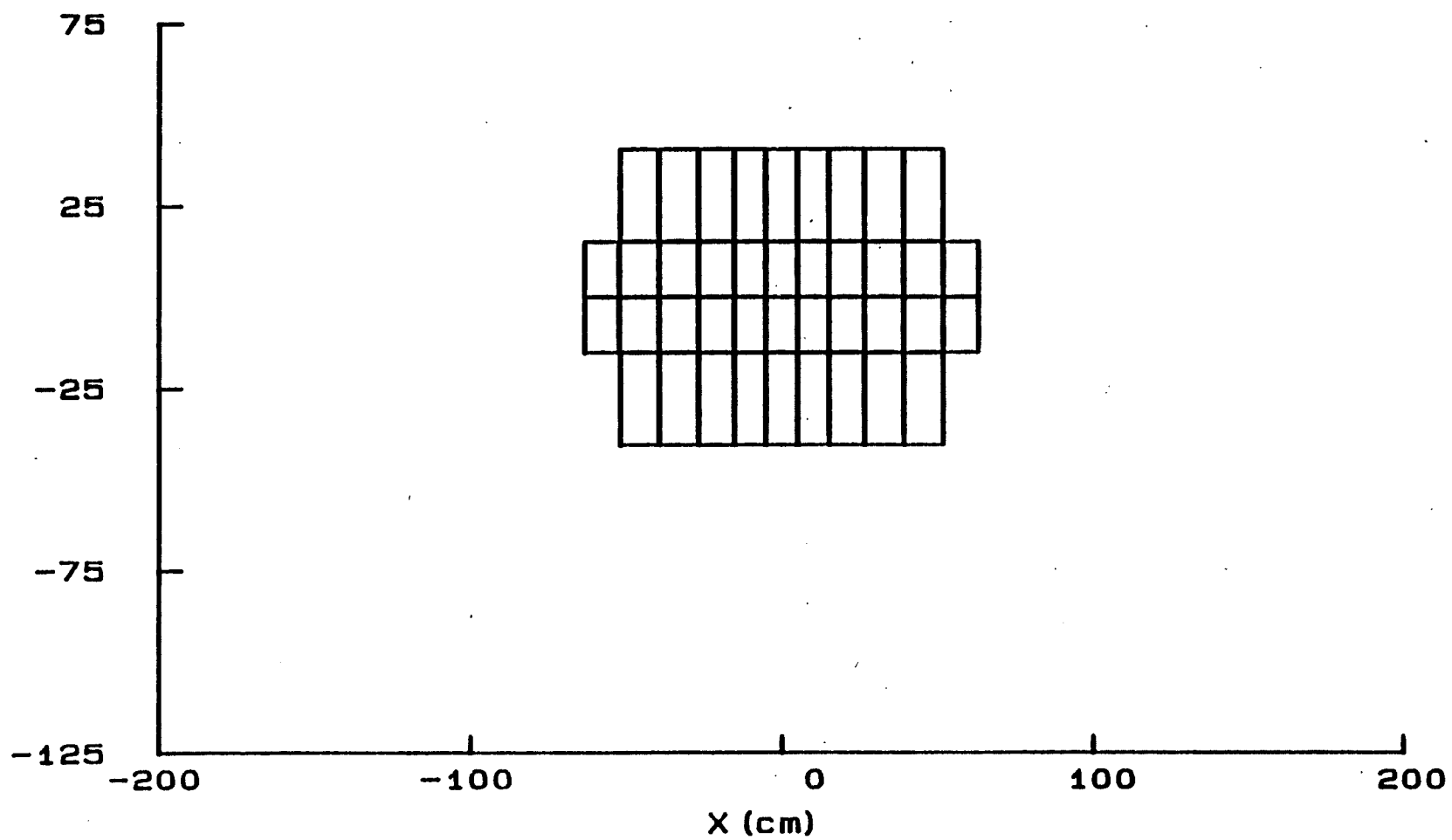
FIG. 28. Arrangement of cells in CA
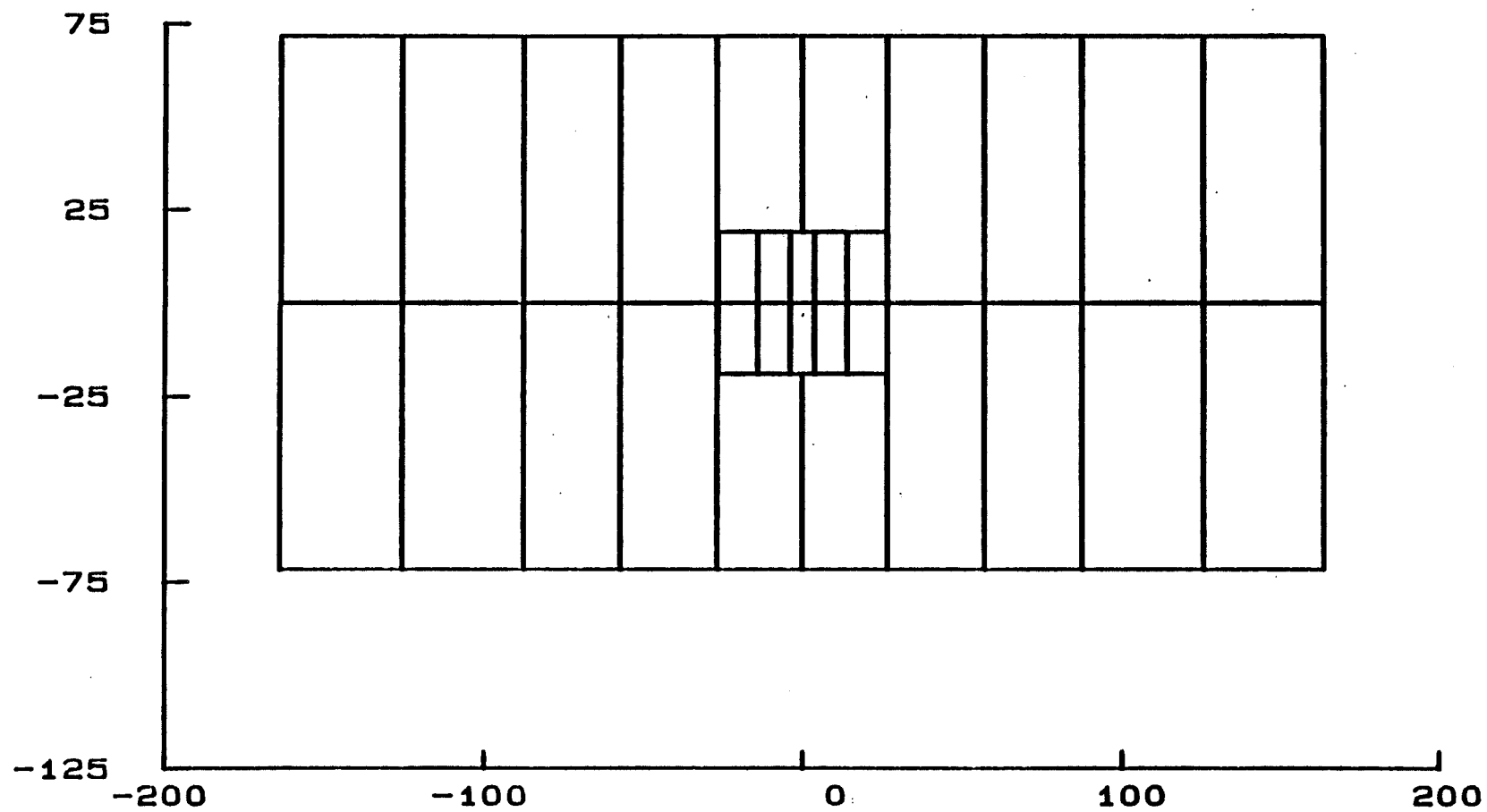
FIG. 29. Arrangement of cells in CB
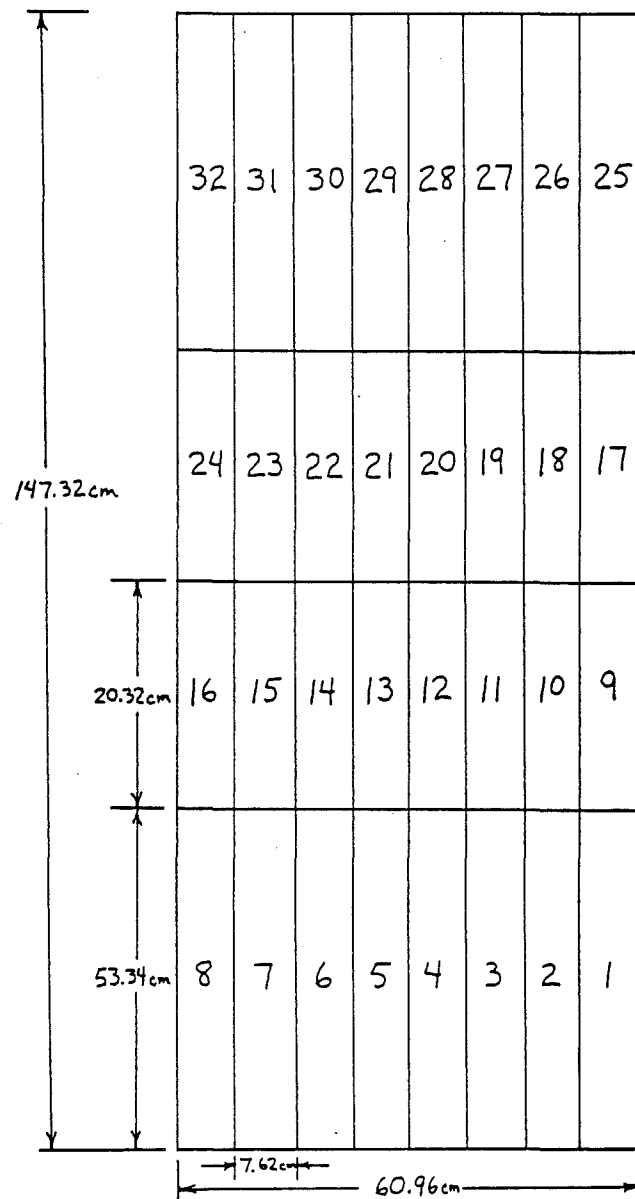
FIG. 30.   Arrangement of elements in SCWALL

wide.   The two central rows extended 20.32 cm from the center line.   The outer rows extended an additional 33.02 cm.

G.   The 1 x 1 Counter

This 1" X 1" scintillating plastic square was placed in the direct path of the bent beam.   This detector confirmed interaction of a beam particle by containing no signal when other detectors contained interaction signals.   This was a veto against spurious events, cosmic ray interactions, and old beam particles in the spectrometer.   The counter was located between DA an DB.

H.   The Trigger Processor.

In order to minimize the number of irrelevant events which must be processed by the on-line and off-line hardware and software, many high energy physics experiments employ a trigger processor designed to accept only events which satisfy certain geometric or dynamical criteria.   Such a processer was employed in this experiment.   A brief, qualitative description of the operation and function of the trigger processor logic will be provided here.   A more detailed discussion of the processor is given in Refs. 3-5.

1.   Function of the trigger processor

The trigger processor of this experiment was designed for the rapid identification of kaons.   Also incorporated into the design was logic to determine if oppositely charged kaons had sufficiently low relative mass to be considered candidate $\phi$ meson decay products.   In addition to these experiment-dependent functions, the trigger processor must determine that an interaction has in fact occurred.   Logically, identification of

valid events precedes evaluation of those events for kaon content; consequently, we will describe this function of the trigger processor first.

## 2. Event identification

Event identification proceeded in the following fashion:

a) A logic signal from the accelerator control (BMGT) indicated that the beam spill was in progress.

b) Three small scintillation counters immediately in front of the target were used to verify that the beam particle was on target. SA and SB were on for good beam tracks on target. SC was a veto counter against wide angle beam tracks; if on, it indicated an off-axis beam track.

c) Consequently, the beam particle was accepted by

$$BM = SA \cdot SB \cdot \overline{SC} \cdot BMGT.$$

d) An interaction by the beam was then required. This was provided by two independent determinations. First, a pulse of amplitude greater than some pre-established minimum threshold in the dE/dx counter indicated beam interaction (DEDX). Second, the absence of a beam particle from the 1 x 1 counter far downstream in the beamline served as an independent evaluation of interacting beam ($\overline{1X1}$). Hence, interacting beam was defined by

$$IB = BM \cdot DEDX \cdot \overline{1X1}.$$

e) A preliminary signal (enable) was established as a gate to turn the trigger processor on. This signal required that no more than five mirrors of CB contain light, and that the dE/dx counter pulse height be less than fifteen times that expected from a single minimum ionizing

particle:

$$E = IB \cdot \overline{CB{>}5} \cdot \overline{DEDX{>}15}$$

## 3. Event selection

In order to identify valid four-kaon events, it is necessary to estimate the momentum of a track from its bend angle in the magnet, and establish that this momentum is in the kaon band of CB. In order to perform this function rapidly, the wires of CX, DX1, and DBX2 were logically ORed together to form 32-element hodoscopes within each plane. A trigger processor track consisted of a coincident hit in all three chambers, on a predefined road, which had an associated known upstream production angle, $\theta$, and an associated known momentum P. Before these angles and momenta are used for trigger particle identification, the multiplicities in the trigger chambers are used to generate the event gate,

$$EG = E \cdot CX[4,9] \cdot DX1[4,9] \cdot DBX2[4,10] \cdot \overline{CA{>}8} \cdot \overline{CB{>}6} \cdot \overline{SC{>}7},$$

where the chamber multiplicities are within the inclusive ranges given, and the multiplicity in CA, CB, and SCWALL is limited as shown.

A kaon is defined within the trigger processor by the existence of a valid road with no light in the associated cells of CB. It is thus possible to trigger on the presence of $K^+K^-$ and $K^+K^-K^+K^-$, and these 2K and 4K triggers were intermediate steps in the construction of the $\phi$ and $\phi\phi$ triggers. The $\phi$ was determined by calculating the effective mass of a $K^+K^-$ pair to first order in the trigger processor,

$$M^2_{KK} = P_+P_-(\theta_+ - \theta_-)^2,$$

and establishing that the calculated mass was less than a Monte Carlo

established cutoff mass, approximately 1.02 GeV/c$^2$. In addition, the $\phi$
candidate transverse momentum was estimated by

$$P_t = P_+\theta_+ + P_-\theta_-$$

in order to permit selection of high-effective-mass $\phi\phi$ pairs in a
fraction of the events. Final trigger selection involved a multiplicity
cut on the number of identified kaons (2, 3, or 4 of each charge state
allowed), and the requirement of a $\phi$ mass for two distinct $K^+K^-$ pairs.
The $P_t$ trigger was identified when it occurred, but was not a trigger
requirement during data collection.

CHAPTER IV

DATA ANALYSIS

As in most high energy physics experiments, the data were analyzed using a sequence of programs which performed the following discrete steps:

a) Translating the digital information stored by the on-line computer into position information and performing pattern recognition to identify particle tracks.

b) Performing a high-resolution fit to the identified tracks, to facilitate the elimination of spurious tracks introduced by the pattern recognition process.

c) Particle identification with the surviving reconstructed tracks.

In this chapter, the programs used in each step of this analysis will be described.

A.  Pattern Recognition

Pattern recognition for E623 was performed using the FLOWERS program, written by Dr. J. H. Goldman explicitly for this experiment. The FLOWERS code was optimized for use on the VAX 11/780 computer, and approximately one-third of the FLOWERS analysis was performed at each of three of the collaborating institutions (FSU, Tufts, and Vanderbilt). Approximately $3.65 \times 10^6$ events were processed, with a mean throughput of 0.15 events/second, and an acceptance rate of 90%. The FLOWERS event acceptance criterion was three reconstructed tracks, two of which were

oppositely charged tracks with momenta between 4.0 and 25.0 GeV/c (based on the FLOWERS momentum measurement), and having no light in CB.

The pattern recognition process was:

a) The event was unpacked from the data buffer.

b) The words which contained hit information (that is, which contained information as to the wires in the MWPC and drift chambers which registered particle ionization trails) from the spectrometer were unpacked into a hit register, and a three-dimensional map of these hits was generated in the laboratory coordinate frame.

c) The smart target was examined to determine the z position of the interaction vertex. If no decision could be reached, the center of the target was used, with wide margins of error.

d) The beam track was examined to determine the x and y position of the interaction vertex. As above, if no decision could be reached, the center of the target was used.

e) The track search was initiated in the downstream x-z view. Pairs of the downstream x-z planes (DX1, DX2, DAX2, DAX1, DBX1, and DBX2) were examined. If hits in the pair of planes corresponded to a reconstructed trigger road, these hits were used to generate a straight-line track, and the remaining planes searched for hits within five standard deviations of the established straight-line track. After all trigger roads had been used, the remaining hits were utilized in the same fashion to initiate track finding.

f) Tracking was extended to the upstream x-z plane by extrapolating the downstream legs to the center of the magnet, and establishing a two-point road from the target vertex to the magnet center.

g) Tracking was extended to the y-z plane by use of the u and v planes. These coordinates were paired to the x-z plane track, and used to generate roads with the vertex point. The y chambers, and any u and v chambers not used in the road generation, were searched for hits on the generated road.

h) Criteria for track quality based on the number of hits identified on the given track were developed. These criteria are outlined in Table VII. In general, it was determined that track quality was better determined by the number of hits on the reconstructed track than by the chi squared of the fit(s).

i) After the completion of track finding, the tracks, with all included points, were written to the output data buffer for further processing.

Three typical FLOWERS events are shown in Figs. 31-33. A careful analysis of FLOWERS output in this format has shown that the worst inefficiency in the FLOWERS algorithm is the y-u-v reconstruction and matching, particularly for low momentum (below 6 GeV/c) tracks. The worst consequence of this problem is a broadening of the reconstructed $K^*$ resonance. Since identified kaons are restricted to be between 5.8 and 23.0 GeV/c by the Cherenkov thresholds, the typical pion from $K^*$ decay lies below the 5.8 GeV threshold. These pions are particularly subject to the inefficiencies of the pattern recognition. Since the reconstruction algorithm was optimized near 10 GeV/c, the kaon sample is not strongly affected.

TABLE VII

MINIMUM HIT REQUIREMENTS BY TRACK SEGMENT[a]

| TRACK SEGMENT | LEECH8 REQUIREMENT | QUALITY REQUIREMENT[b] |
|---|---|---|
| Complete track | 12 | 14 |
| Upstream | 5 | 5 |
| Downstream | 5 | 6 |
| Total x | 6 | 6 |
| Total y | 3 | 2 |
| Total u/v | 3 | 3 |
| Upstream x | 3 | 3 |
| Downstream x | 3 | 3 |
| Upstream y | 2 | 2 |
| Downstream y | 0 | 0 |
| Upstream u/v/y | 3 | 3 |
| Downstream u/v/y | 3 | 3 |

[a]That is, the minimum number of hits on each track permitted by the routine following pattern recognition and track quality analysis in the LEECH8 routine

[b]QUALITY is a routine which reevaluated those tracks failing the LEECH8 criteria after analysis of the systematics of FLOWERS. The failed LEECH8 tracks were retained during the analysis if they passed the criteria listed in the second column, if they contained at least 6 u/v/y hits, or if they contained 17 or more total hits. These tracks were, however, the first cut during the test for shared legs. Only LEECH8 kaons were used in the analysis.

a

MPS X COORD ×10¹

MPS BEAM AXIS ×10²

125.00    100.00    75.00    50.00    25.00    0.00    -25.00    -50.00    -75.00    -100.00    -125.00    -150.00

20.00    00.00    60.00    30.00    20.00    10.00    0.00    -10.00    -20.00

874.

78.

BBX2
IBX1

DAX2
SAX1

BX2
BX1

CX

BX3
BX2
RX1
AX1

VBX
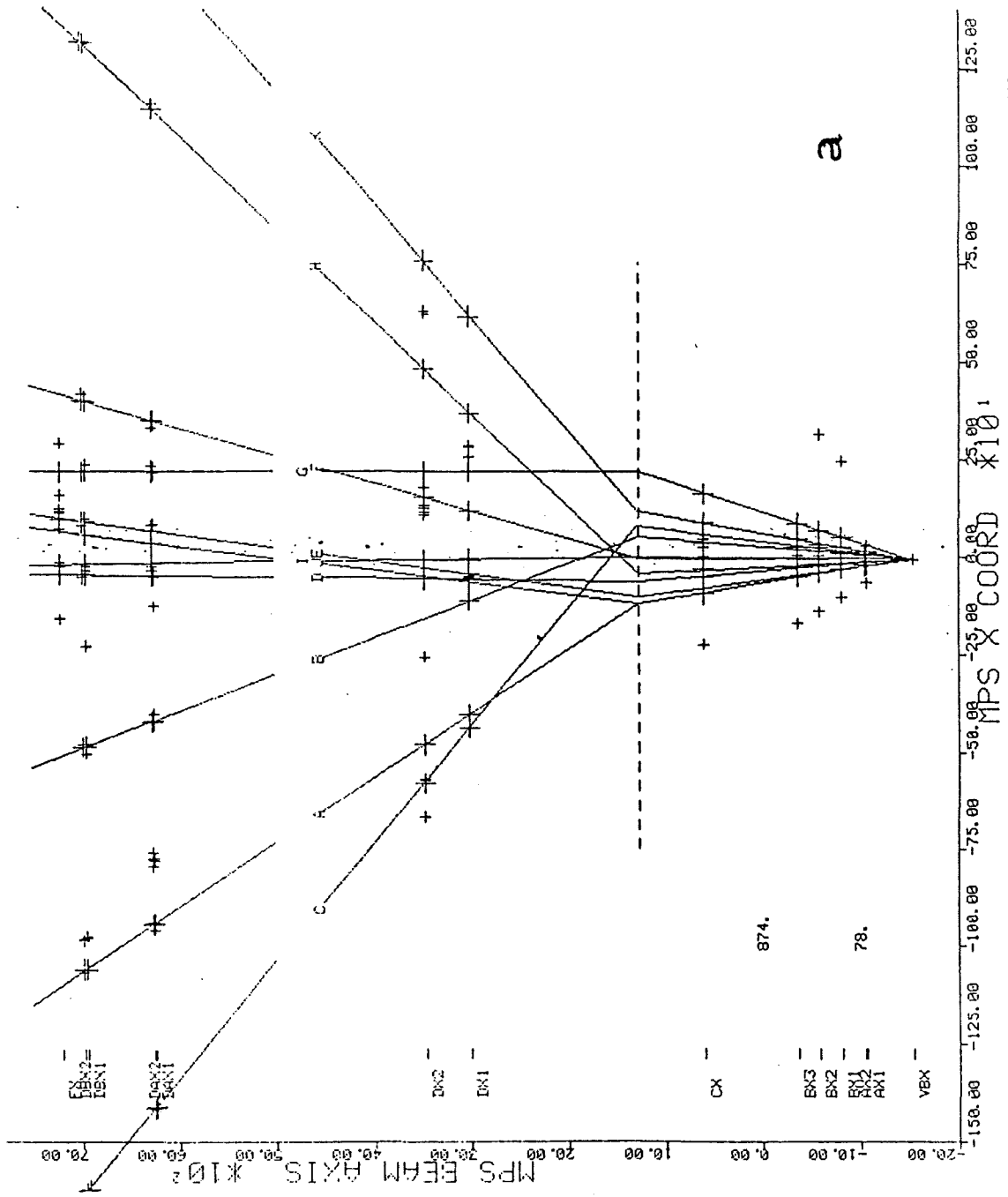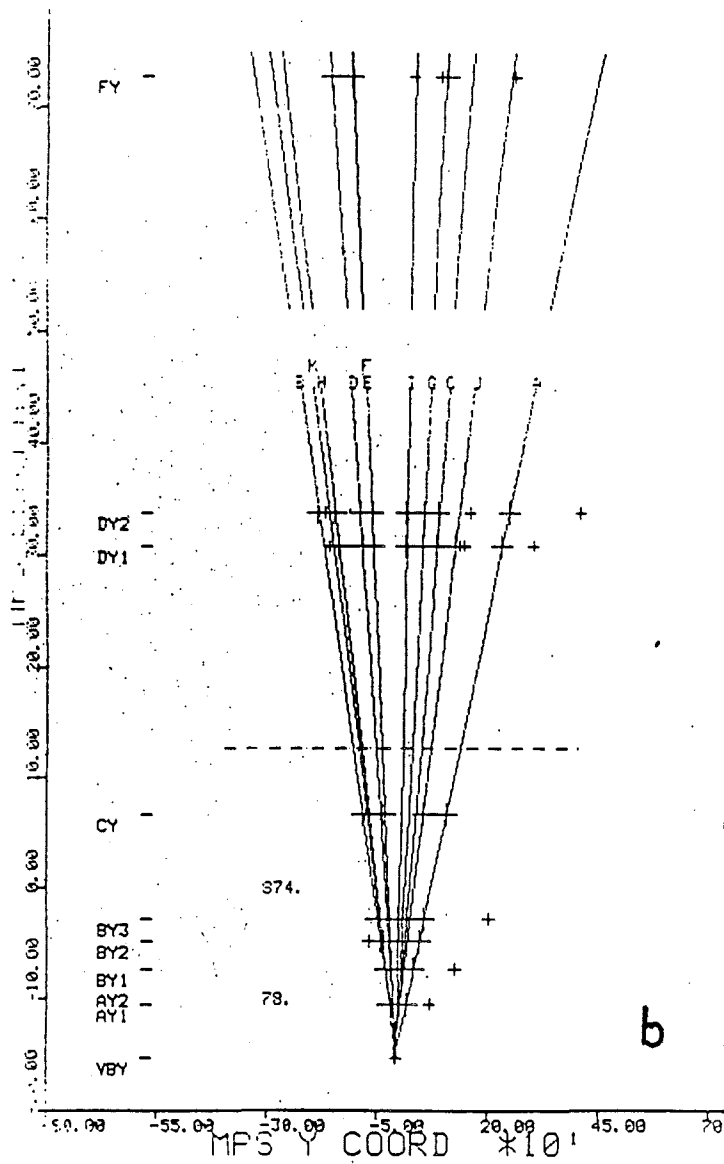
FIG. 31.  FLOWERS reconstruction of Event 78/874

(a)  x-z projection  (b)  y-z projection

W

a

MPS X-COORD *10¹

MPS ELEVATION *10²

125.00  100.00  75.00  50.00  25.00  0.00  -25.00  -50.00  -75.00  -100.00  -125.00  -150.00

877.

78.

EBX2=
DBX1
DAX2=
DAX1

DX2
DX1

CX

BX3
BX2
BX1
AX1
ABX
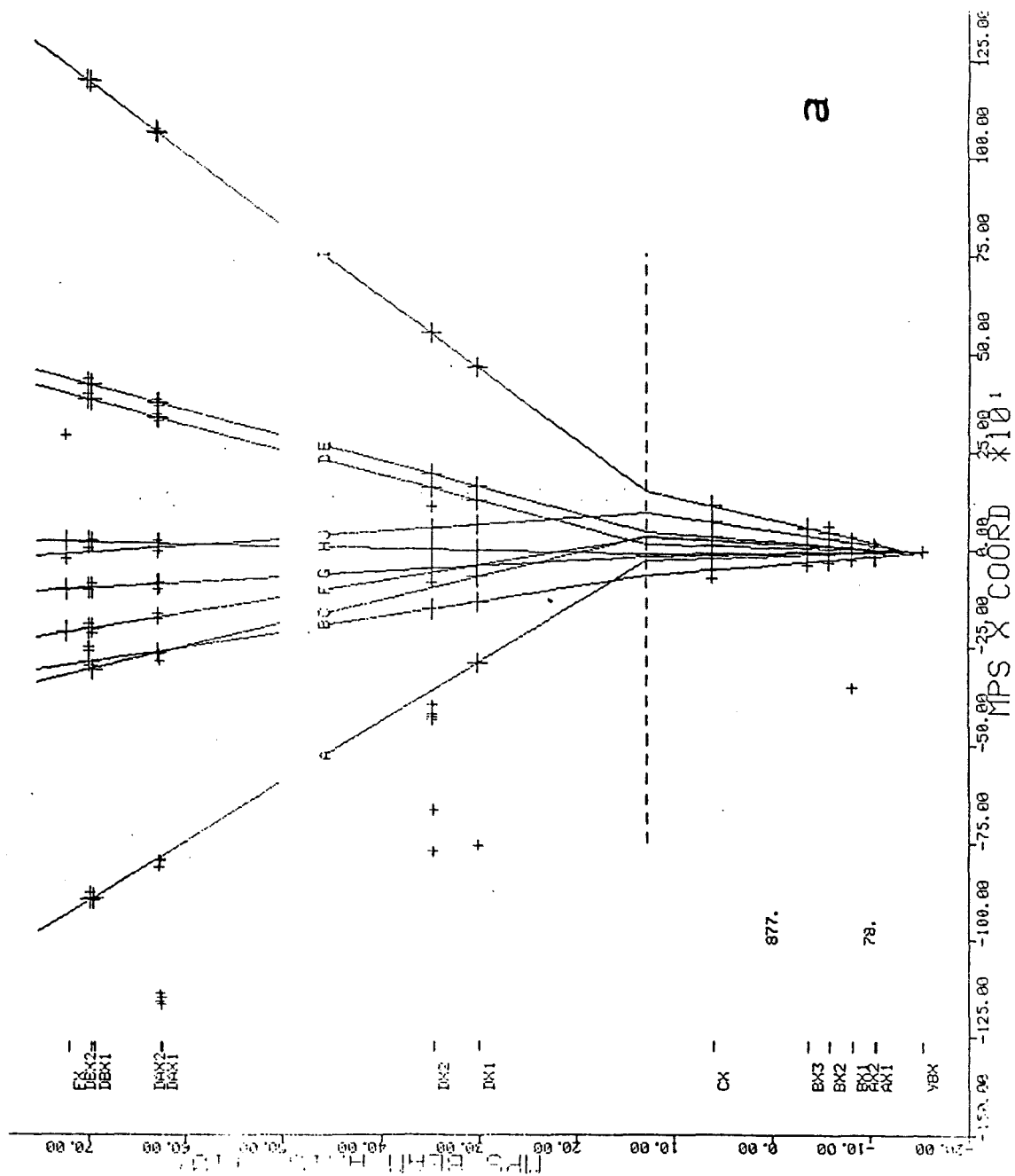
FIG. 32. FLOWERS reconstruction of Event 78/877

(a) x-z projection (b) y-z projection

FIG. 33.  FLOWERS reconstruction of Event 78/895

(a)  x-z projection  (b)  y-z projection

B.   Track Fitting

Following pattern recognition, an independent track fitting program was used.   The KLEANX program developed for FMPS experiment E580 was used for preliminary analysis of track data.   KLEANX used a five-parameter three-dimensional fit that integrated the particle trajectory through the spectrometer magnetic field.   For E623, however, the TIPTOE program developed by J. H. Goldman and J. M. Marraffino was used.   TIPTOE includes the LEECH8 track fitting routine, a six-parameter three-dimensional fit routine which models the track as four straight lines (upstream and downstream, x-z and y-z), with bends in the magnet in both planes.   The track momentum was then obtained from a table generated using the magnetic field grid map and a KLEANX-like fit. Three tracks which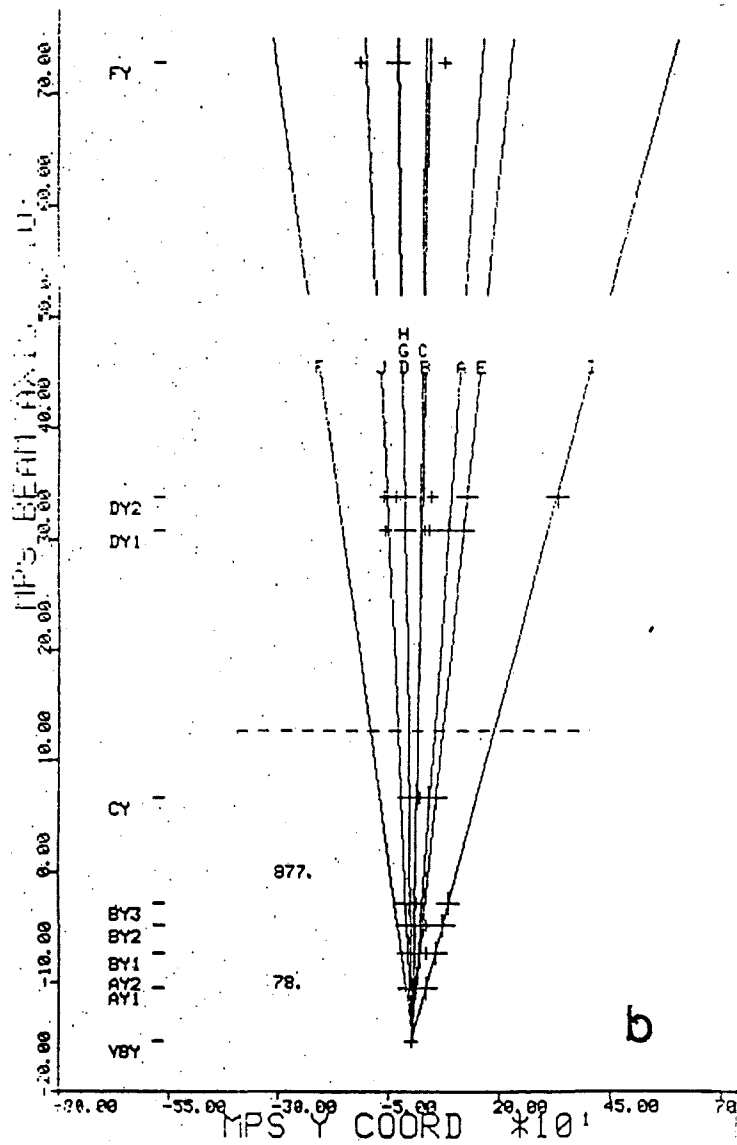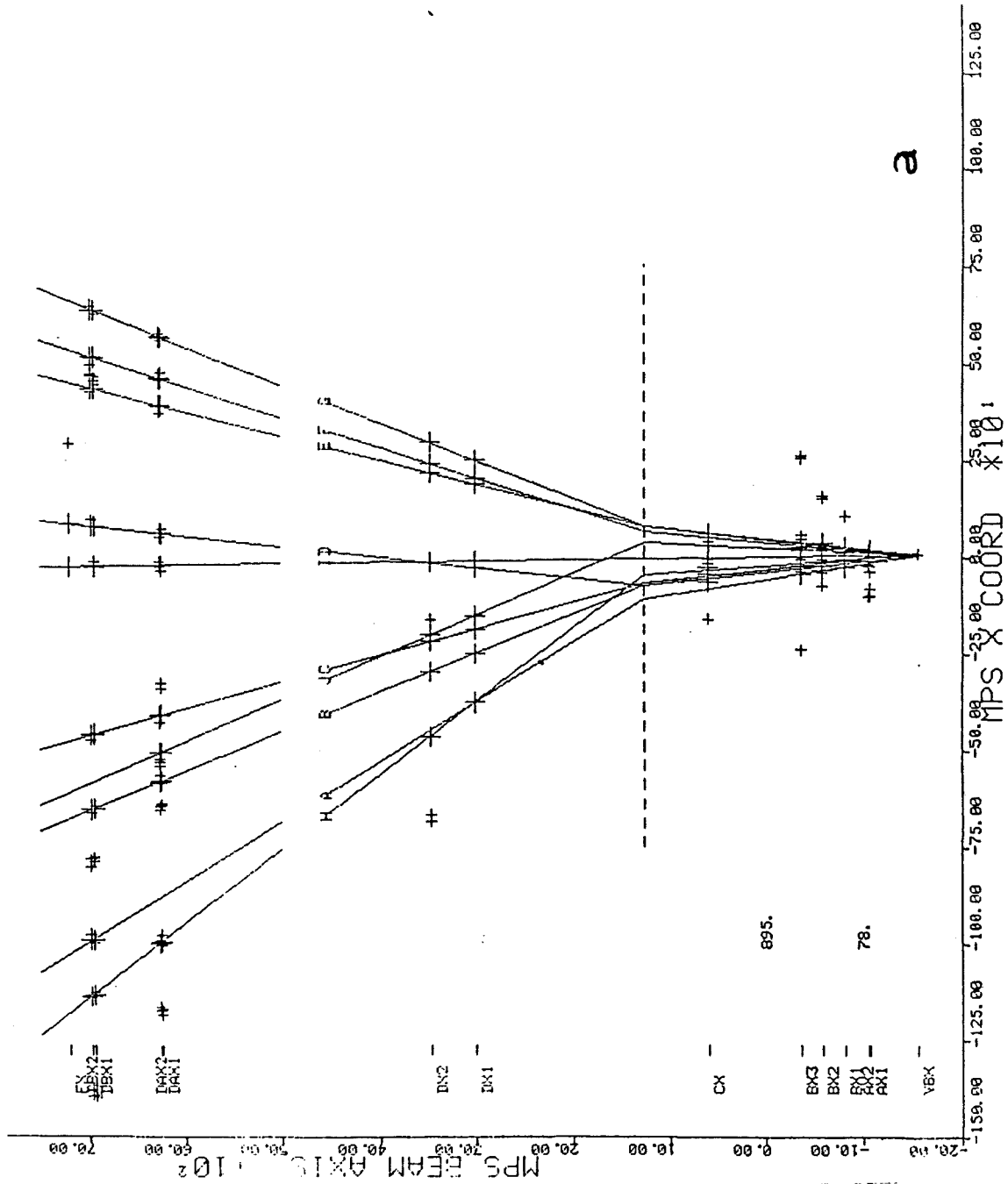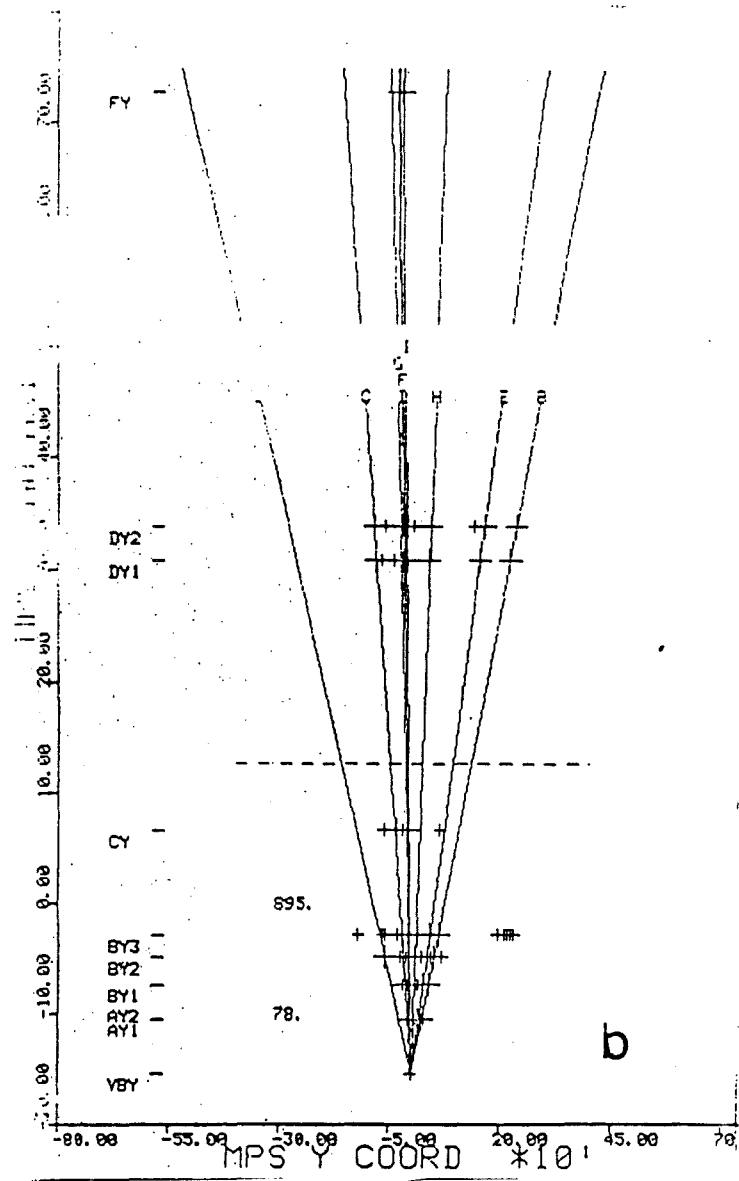 survived the cuts with a somewhat stricter momentum requirement on the opposed charge pair ($5.5 < p < 25.0$ GeV/c) were also required, as was the requirement that the track be a kaon candidate. This was determined either by the absence of light in the Cherenkov cell associated with the track, or by the track sharing the cell with another which could potentially emit light.   With this requirement, $2.1 \times 10^6$ $K^+K^-X$ events survived the TIPTOE cuts.

In addition to the track fit, TIPTOE performed a fit to determine a better vertex for the event, and adjusted the momenta of the tracks to reflect their origin at the common vertex.   This fitting procedure was used to reject tracks which came from secondary vertices due to the decay of long-lived neutral particles (which had already been partially rejected by the trigger).   In analyses on Monte Carlo data, this procedure yielded the best momenta for the reconstructed tracks, and rejection of tracks from secondary decays.

In preparation for the detailed track fit, an analysis was performed to determine the internal consistency of the chamber coordinate system. Studies were performed using the KLEANX and LEECH6 track fitting routines to determine systematic deviations of hit coordinate from the best-fit track. These deviations are due to residual variations of wire position and chamber angle from the surveyed values. The residuals were typically of the order of the survey measurement errors, although a few residuals were as large as a centimeter. A final set of residuals was determined by comparison of the results of the independent determinations; this set of residuals, and the other chamber-dependent information used in the TIPTOE fit, are shown in Table VIII.

C. Particle Identification

Final particle identification for E623 was achieved by analysing the TIPTOE output with the ROSES program, written by J. H. Goldman and C. Georgiopolous. In addition to particle identification, ROSES reevaluated some of the TIPTOE results in the light of the inefficiencies of FLOWERS which have been previously discussed. ROSES yielded $1.8 \times 10^6$ events, each containing at least three surviving tracks with one identified $K^+$ and one identified $K^-$. The momentum band for ROSES kaons was 5.69 - 23.0 GeV/c.

Particle identification made use of CB exclusively. A description of the Cherenkov counters is given in chapter 3. The algorithm used in the particle identification analysis was:

a) For each track in the event, the cone defined by the angle of emission of Cherenkov photons was calculated, based on the assumption

TABLE VIII

CHAMBER RESIDUAL OFFSETS

| CHAMBER | RESIDUAL IN CHAMBER PLANE μm | RESIDUAL IN Z POSITION mm | RESIDUAL ANGLE mrad |
|---|---|---|---|
| AX1 | -46.73 | 0.0000 | -0.1696 |
| AY1 | -7.15 | 0.0000 | 0.1696 |
| AX2 | 103.93 | -0.3836 | 0.0000 |
| AY2 | 37.33 | 0.2440 | -0.9282 |
| AU | -5.20 | -0.3557 | 0.0322 |
| AV | -10.69 | 0.0000 | -1.4165 |
| BX1 | -40.51 | 0.3997 | 1.7165 |
| BY1 | -17.54 | 0.0000 | 0.7570 |
| BX2 | -35.38 | 2.8592 | 2.4128 |
| BY2 | 14.38 | -0.3933 | 1.4868 |
| BX3 | 7.13 | 3.9744 | 2.3057 |
| BY3 | -7.49 | -1.6941 | 2.9680 |
| BU | -116.69 | 2.8188 | 1.0056 |
| CX | -157.75 | 5.8858 | 0.3817 |
| CY | 109.44 | 1.0101 | -0.3538 |
| DX1 | -41.99 | 1.2600 | 0.4136 |
| DY1 | -113.77 | -5.9067 | -0.3236 |
| DU | 174.96 | 3.9413 | -2.9663 |
| DV | 204.47 | 2.4829 | 4.7375 |
| DY2 | 161.93 | -3.0402 | -0.4851 |
| DX2 | -107.25 | 3.3900 | -2.8132 |
| DAX1 | -101.71 | -0.0602 | -0.1538 |
| DAX2 | 114.85 | 0.2600 | 0.0448 |
| DAU | 36.29 | 0.4397 | -0.3422 |
| DAV | 749.80 | -1.1136 | -0.0402 |
| DBX1 | -97.92 | -0.1818 | 0.0806 |
| DBX2 | -166.20 | -0.2529 | 0.3102 |
| DBU | -57.43 | 0.9677 | 0.1022 |
| DBV | -36.23 | -1.6088 | -0.4444 |
| FX | -236.09 | 6.5662 | -1.5610 |
| FY | 321.56 | 11.7094 | -2.6310 |
| FU | -105.45 | 8.3055 | -0.6614 |
| FV | 338.27 | 6.1768 | -1.8030 |

that the track was a pion.  This cone was extrapolated to the mirror plane, and the set of mirrors intersecting the cone determined.  The intersection area of the cone with the mirrors was calculated, weighted by the 1/R dependence of the photon density in the Cherenkov cone.

b) For each track, the expected number of photoelectrons for the track is calculated for the separate identifications of the track as pion, kaon, or proton.  This number is

$$N_{phe} = N_{max} \left[ 1 - \left( \frac{m}{p} \right)^2 \left( n^2 - 1 \right)^{-1} \right],$$

where $N_{max} = 6$, the expected number of photoelectrons from a $\beta = 1$ particle, and n = 1.0003 is the index of refraction for nitrogen at STP.

c) The numbers calculated in step b are weighted by the results of step a and stored in an array by mirror number.

d) A loop over the mirrors is executed, identifying first mirrors with one track, then two, etc., and the expected pulse height in each mirror calculated.

e) If the observed pulse height is below threshold, tracks are assigned an identity based on the particle momentum.  At least 30% of the weighted area of the track must be within the mirror for a clean identification at this stage.

f) If the pulse height is above threshold, the number of photoelectrons detected by the mirror is calculated.  Then, the tracks which have some portion of their cone in the mirror are examined, in order of decreasing track momentum.  The number of photoelectrons obtained for a given track in this mirror in step c is subtracted from the total observed number of photoelectrons.  The subtraction is performed for each candidate track identity, and the identity yielding

the result closer to zero is accepted. This process is repeated with the next track in the sequence for the given mirror until zero photoelectrons remain. Any additional tracks are identified based on the lack of associated light.

Following this procedure, ten distinct identity assignments were given. These assignments are:

ID = 0:  $\pi$, track below pion threshold (5.69 GeV/c)

1:  $\pi$, (5.69 < p <23.0 GeV/c, associated light)

2:  K, (5.69 < p <23.0 GeV/c, no light, ambiguous with protons)

3:  p, (23.0 < p <38.3 GeV/c, no light)

4:  $\pi$, (23.0 < p < 38.3 GeV/c, light)

5:  $\pi$, (p > 38.3 GeV/c, light)

6:  unidentified track (four mirrors intercepted, etc.)

7:  p > 38.3 GeV/c, but no associated light

8,9:  p < 5.69 GeV/c, but light observed or trigger processor kaon road associated with track

In addition, each track has an assigned weight and flag which reflects the quality of that identification. This weight is based on the number of tracks giving light in the mirror which are removed before kaon identification can occur, for that mirror in which the identification of a given track was made.

D.  Summary of Data Analysis Procedures

As can be seen from the discussion above, the worst data in the experiment are the pions below pion threshold (5.69 GeV/c). The pattern recognition yielded poor tracking due to the matching problem discussed in Sect. A, and the low momentum makes any attempt at particle

identification impossible. In the subsequent analysis, however, these data play a key role. The reason for this stems from kinematics. Any final state which decays into a kaon or kaons in the momentum band in which kaons can be identified (ID = 2), tends to yield pions at momenta below that band in the laboratory frame. Thus, we accept the inevitable but small contamination in the data sample and proceed to physics analysis.

CHAPTER V

RESULTS

The results of the analysis will be presented below. In Section A, the final (post-ROSES) data selection procedures will be described. Section B is a summary of previous results obtained from this experiment. Section C is the presentation of the new results. The acceptance and cross section calculation is discussed in Section D. Finally, the interpretation of these results is presented in Section E.

A. Data Selection

Following the end of detailed analysis in ROSES, several other steps were performed to improve the data set for subsequent analysis. First, an analysis of the ROSES output was used to identify tracks which were insufficiently well defined and/or which contained the same set of hits in the y view (shared leg). The shared leg cut required that tracks weakly defined within the y chambers be well defined by the u-v road. Further, pairs of tracks with y slopes differing by less than 0.3 mrad were examined, and only the track with the greater number of points retained. Following this analysis, only events which contained at least four surviving kaon tracks (two neutral pairs) with momenta between 5.8 and 23.0 GeV/c were retained. This stricter criterion for momentum did not significantly affect the $\phi$ measurement. In addition, sharp cuts on the position of the vertex were applied. These cuts rejected all events with vertices outside the limits defined by the

positions (in centimeters measured in the laboratory coordinate system):

$$-1.87 < x < 1.17;$$

$$-1.52 < y < 1.52;$$

$$-170.00 < z < -130.00.$$

Finally, only events with fewer than 19 reconstructed tracks were retained. Events with larger numbers of tracks contained too many spurious tracks for analysis. An average of ten charged tracks is produced per 400 GeV/c pN reaction.

From these cuts, the $1.8 \times 10^6$ ROSES events are reduced to 169,231 by the 4K requirement, and to 120,970 when all other cuts are made. This sample is used for the analysis described in Sect. B. The sub-sample with an additional $\pi^+\pi^-$ contains 94,786 events; only these events are used in the analysis presented in Sect. C - E. The trigger rates for the various processes which combined to form the $\phi\phi$ trigger are given in Table IX. These rates are the fractions of the total interacting beam cross section, 30 mb, represented by each trigger process; for example, the 12 $\mu$b $\phi\phi$ trigger rate means that for each interaction, $12/30{,}000 = 4 \times 10^{-4}$ $\phi\phi$ triggers are recorded.

## B. Previous Results

As was stated in the introduction, E623 was a triggered $\phi\phi$ search. The mass sectrum[4,5] or $\phi\phi$ is shown in Fig. 34, with background subtracted. The acceptance for $\phi\phi$ events was $(4.2 \pm 0.4) \times 10^{-4}$, as determined by the generation of events with $\phi\phi$ in the LUND Monte Carlo, the propagation of these simulated events through the spectrometer and trigger processor, and the analysis of the result using the FLOWERS-TIPTOE-ROSES procedure. The total $\phi\phi$ sample contained 177 $\pm$ 42

TABLE IX

TRIGGER RATES

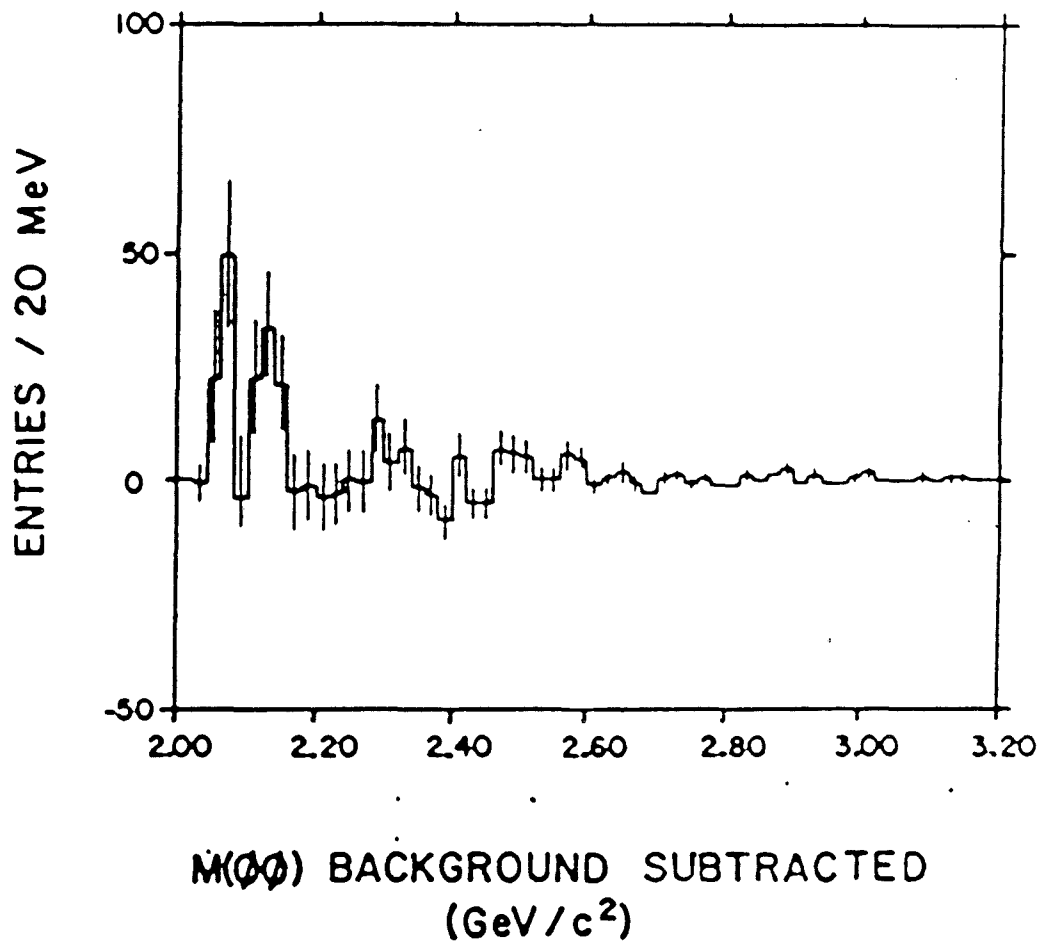| NAME | $\sigma$ |
|------|----------|
|      | $\mu b$  |
| IB = $\sigma_i$ | 30,000 |
| E | 8,760 |
| EG | 1,077 |
| 2K | 377 |
| $\phi$ | 121 |
| $\phi$PT | 60 |
| 4K | 94 |
| 2K$\phi$ | 51 |
| 2K$\phi$PT | 26 |
| $\phi\phi$ | 12 |
| $\phi\phi$PT | 4 |

FIG. 34.  φφ mass spectrum[4,5]

events, yielding a total cross-section $\sigma = 0.84 \pm 0.27$ μb. As can be seen, the bulk of the signal is in the threshold region; the second enhancement in this spectrum is consistent with the $\phi K^+ K^- / \phi \pi^+ \pi^-$ resonance discussed below. An upper limit (99.7% C.L.) of 3.75 μb/nucleon was obtained for $\eta_C$ production by examination of the $\phi\phi$ decay mode. The $\eta_C$ is known[10] to have a branching ratio of 0.008 to this decay mode.

The $\phi\pi^{\pm}$ mass spectrum[6,7] is presented in Fig. 35. As can be seen, the $D^{\pm} \longrightarrow \phi\pi^{\pm}$ Cabibbo-suppressed decay mode is present, with $234 \pm 43$ events above background. The $D_S$ is not seen. An upper limit (90% C.L.) of 53 μb for $D_S$ production is obtained by using a model with small rapidity gaps between the $D_S$ and the two additional charged kaons required by our trigger. Due to the uncertainties in modeling the trigger response for the two identified kaons not required by the $\phi\pi$ state, the inclusive D hadroproduction cross-section could not be obtained.

The $K_4^{*0}(2.060)$ is observed[8,9] in the $\phi K\pi$ spectrum shown in Fig. 36. An excess of $431 \pm 116$ events is obtained, yielding a $\sigma \cdot BR = 403 \pm 110$ nb. Using the Bourquin-Gaillard model[47] for hadroproduction cross-sections, which yields a $K_4^{*0}(2.060)$ production cross-section of 22 μb, a branching ratio for $K_4^{*0}(2.060) \longrightarrow \phi K\pi$ of 0.018 and for $K_4^{*0}(2.060) \longrightarrow \phi K^{*0}$ of 0.006 is obtained.

Finally, the $\phi K^+ K^-$ spectrum of Fig. 37 and the $\phi \pi^+ \pi^-$ spectrum of Fig. 38 both evidence[10] an enhancement at a mass of $2.141 \pm 0.022$ Gev/c$^2$, of width approximately equal to the resolution. When the enhancement at this mass in $\phi\phi$ is included, the total significance of
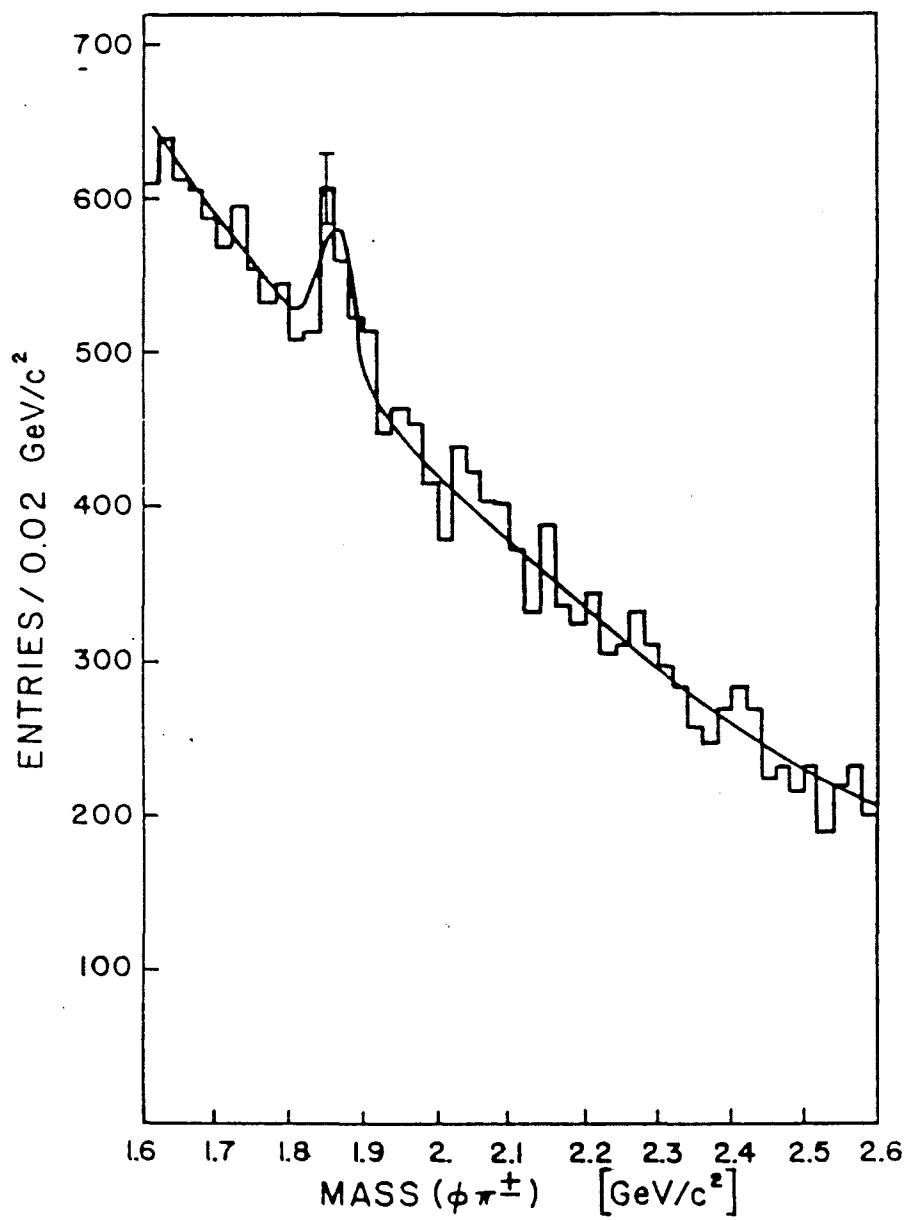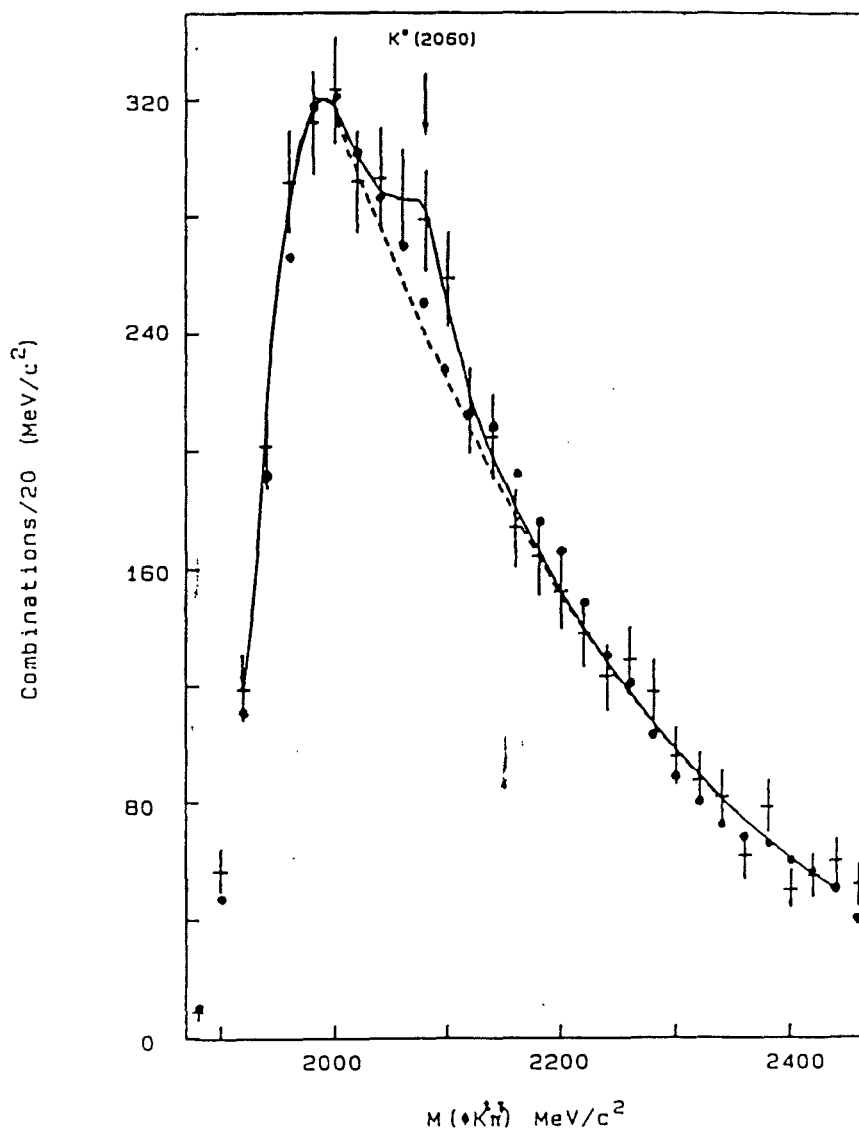
FIG. 35. $\phi\pi^{\pm}$ mass spectrum[6,7]

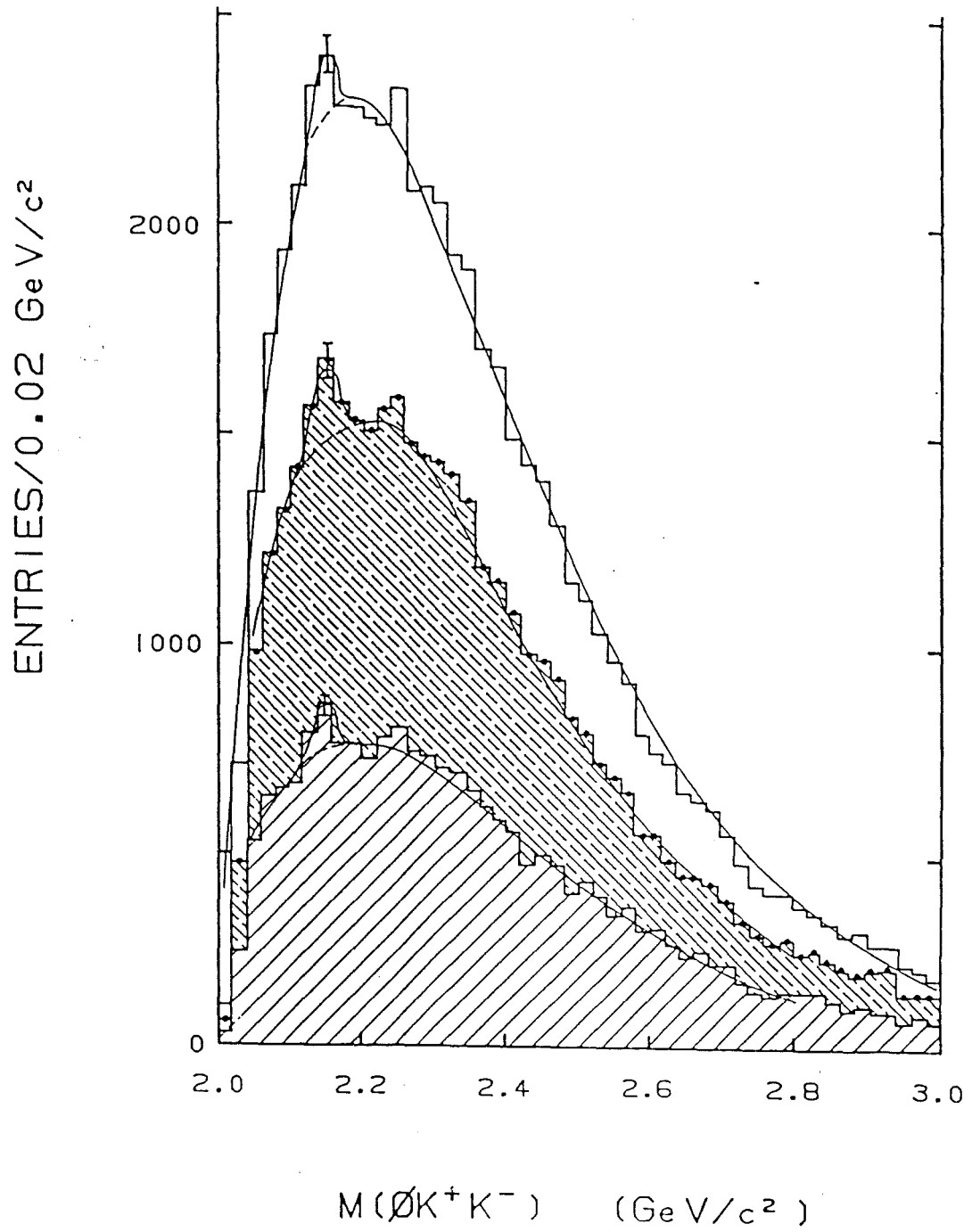FIG. 36. $\phi K\pi$ mass spectrum[8,9]
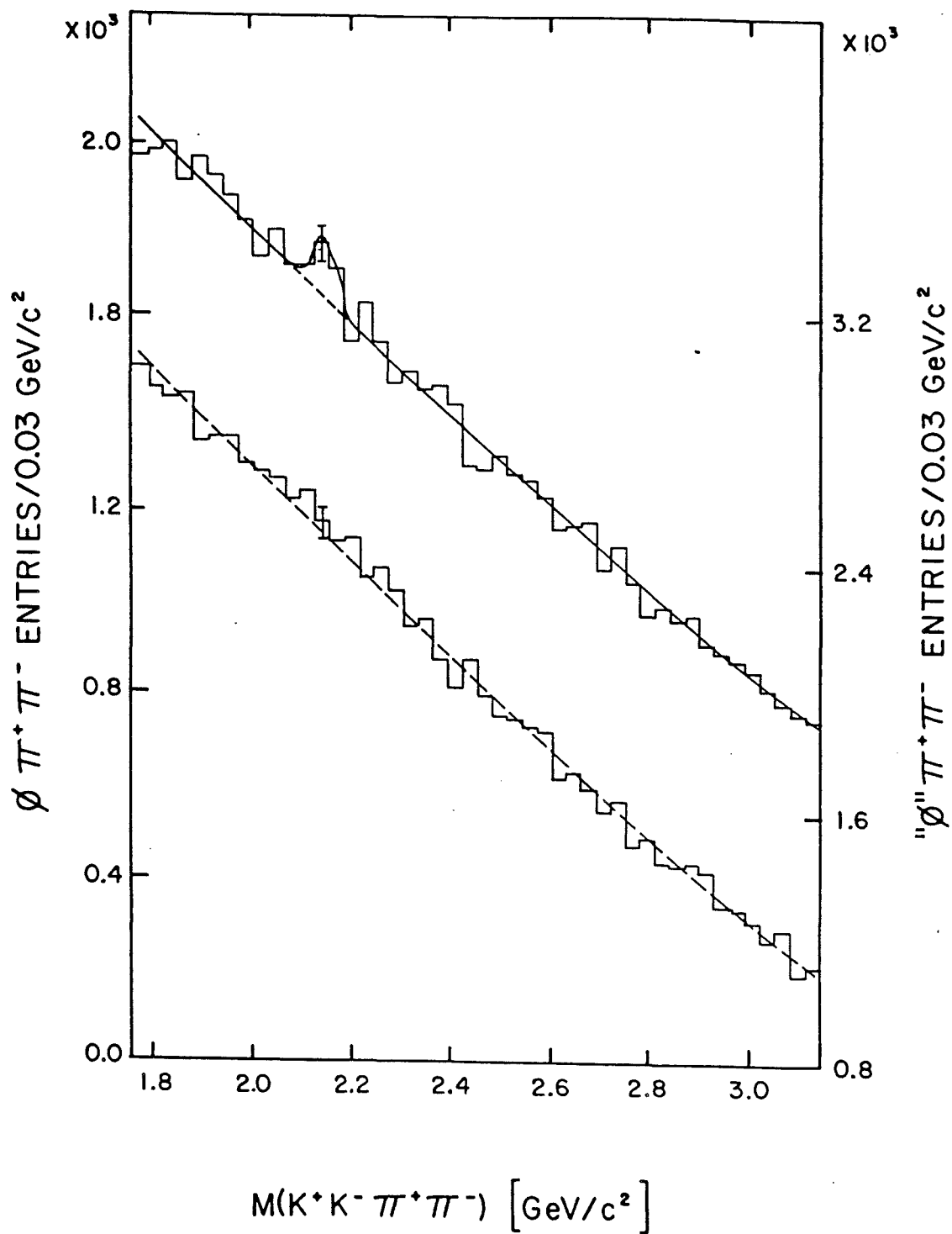
FIG. 37.  $\phi K^+ K^-$ mass spectrum[10]

FIG. 38. $\phi\pi^+\pi^-$ mass spectrum[10]

this enhancement is 7.2 standard deviations. The relative branching ratio is

$$\frac{BR(X \longrightarrow \phi KK)}{BR(X \longrightarrow \phi\pi\pi)} = 0.49 \pm 0.16.$$

The large relative branching ratio to $\phi KK$ suggests that the state is not an ordinary $q\bar{q}$ meson.

## C. Experimental Results

The $K^+K^-$ spectrum is shown in Fig. 39. The spectrum, plotted in $0.002$ GeV/$c^2$ bins in the threshold region, clearly shows the $\phi$ meson, with $2484\ ^{+399}_{-365}$ entries over background. This spectrum, as are all spectra in this analysis, is fitted with the background form

$$b(m) = \alpha(m-m_0)^{\beta}e^{-\gamma(m-m_0)-\delta(m-m_0)^2}.$$

The $\phi$, being resolution dominated, is modeled as a gaussian function. The mass is $1.0196\ ^{+0.0003}_{-0.0004}$ GeV/$c^2$, as compared to the accepted $\phi$ mass of $1.0195$ GeV/$c^2$. The FWHM of the resonance is $0.0099 \pm 0.0013$ GeV/$c^2$, consistent with the natural width ($0.004$ GeV/$c^2$) convoluted with the resolution of $0.006$ GeV/$c^2$. The $\chi^2$/DOF of this fit is $28.4/27$.

In Fig. 40, the $K^+K^-\pi^+\pi^-$ spectrum is presented. This spectrum is fitted in $0.005$ GeV/$c^2$ bins, rather than in the $0.030$ GeV/$c^2$ bins consistent with the Monte Carlo resolution, to demonstrate that the interesting structure in the spectrum is not significantly narrower than the resolution. In this spectrum, ten consecutive bins are seen to be above background, showing a resolution-dominated resonance candidate structure. The resonance candidate is fitted with a gaussian over the background form above; it has a mass of $2.363 \pm 0.005$ GeV/$c^2$, and a FWHM of $0.040 \pm 0.015$ GeV/$c^2$. The resonance contains $1291\ ^{+368}_{-338}$ events over background, and the fit over 200 bins, each of $0.005$ GeV/$c^2$, yields a

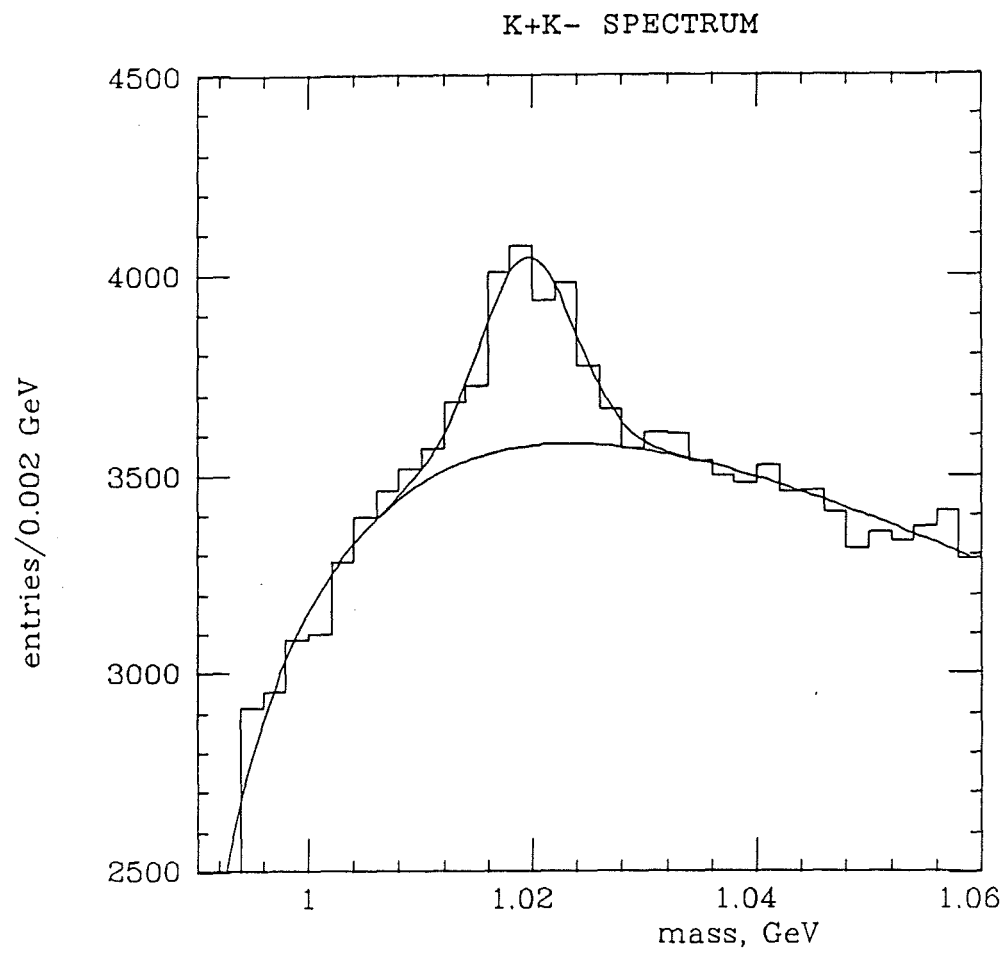K+K- SPECTRUM



FIG. 39. $K^+K^-$ mass spectrum

KKPIPI SPECTRUM


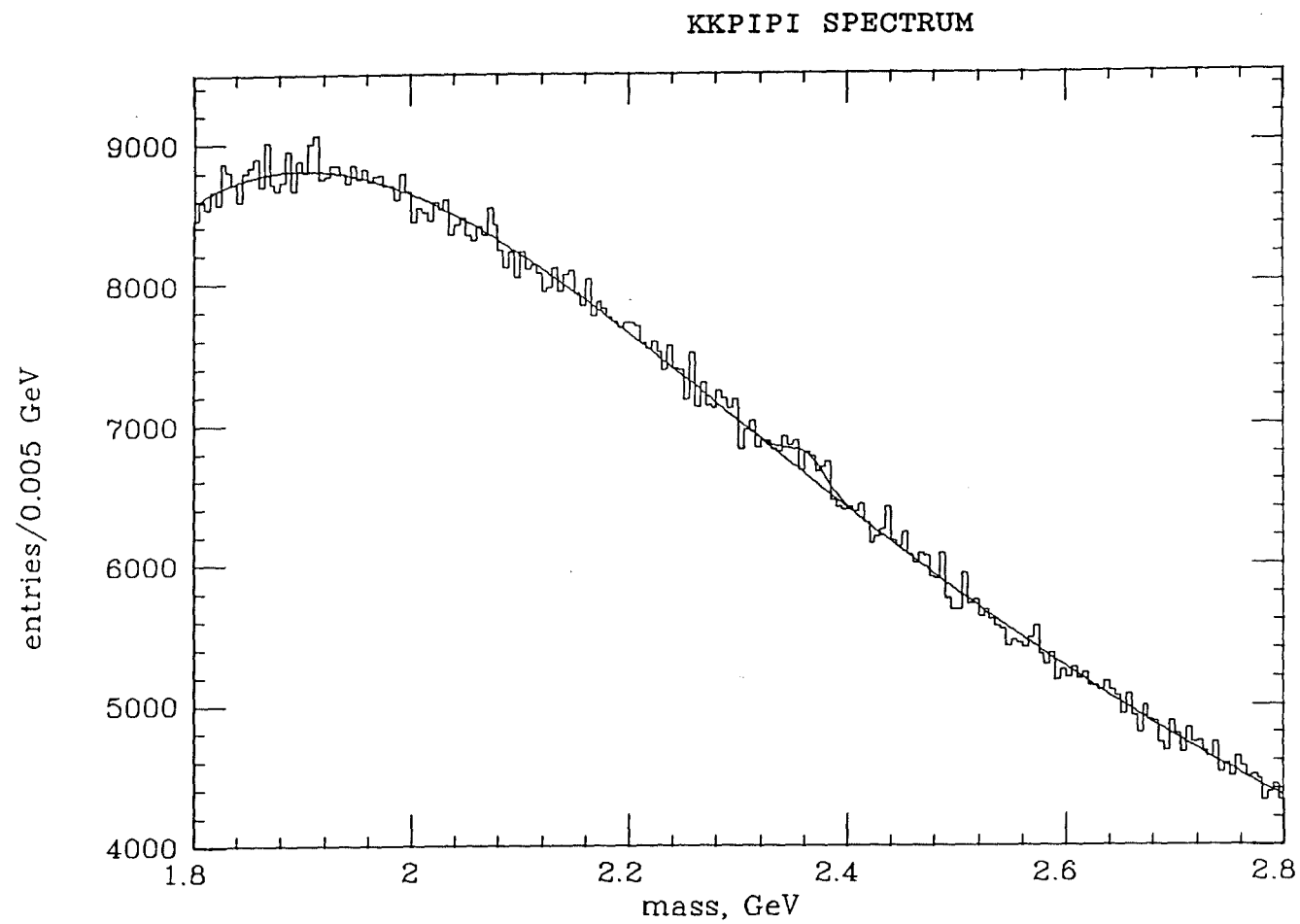
FIG. 40. $K^+K^-\pi^+\pi^-$ spectrum

$\chi^2$/DOF of 222.9/192. In order to show the candidate state more clearly, the difference of the data from the fitted background is shown in Fig. 41; the spectrum is shown in 0.03 GeV/c$^2$ bins (Fig. 42); and, the corresponding background-subtracted spectrum is provided (Fig. 43).

Due to this large background (on the order of 40,000 entries per 0.030 GeV/c$^2$), none of the standard angular correlation techniques for analysis of the resonance candidate can be applied. The most practical correlation is the integral spectrum

$$\int_{p_{t_{min}}}^{\infty} \frac{dN}{dp_t^2} A(p_t^2) dp_t^2,$$

which is shown in Fig. 44. In this equation, A is the angular acceptance of the spectrometer, expressed in terms of the transverse momentum of the four-particle system. It can be seen that the resonance candidate persists to high $p_t$, suggesting a high separation energy in the formation of the state, such as exists in the decay of a significantly more massive state.

The state is also observed to occur in association with high multiplicities of other particles. The observation of the state in events containing more than the minimal (two K$^+$, two K$^-$, one $\pi^+$, one $\pi^-$) kaon and pion multiplicities is shown in Table X. This table shows the number of entries in the resonance candidate state above background in the inclusive (i.e., including all higher multiplicities) subsamples listed on the table. The significance of the signal remains approximately constant as these cuts are applied, demonstrating increased relative production in the more restrictive samples.

KKPIPI SPECTRUM
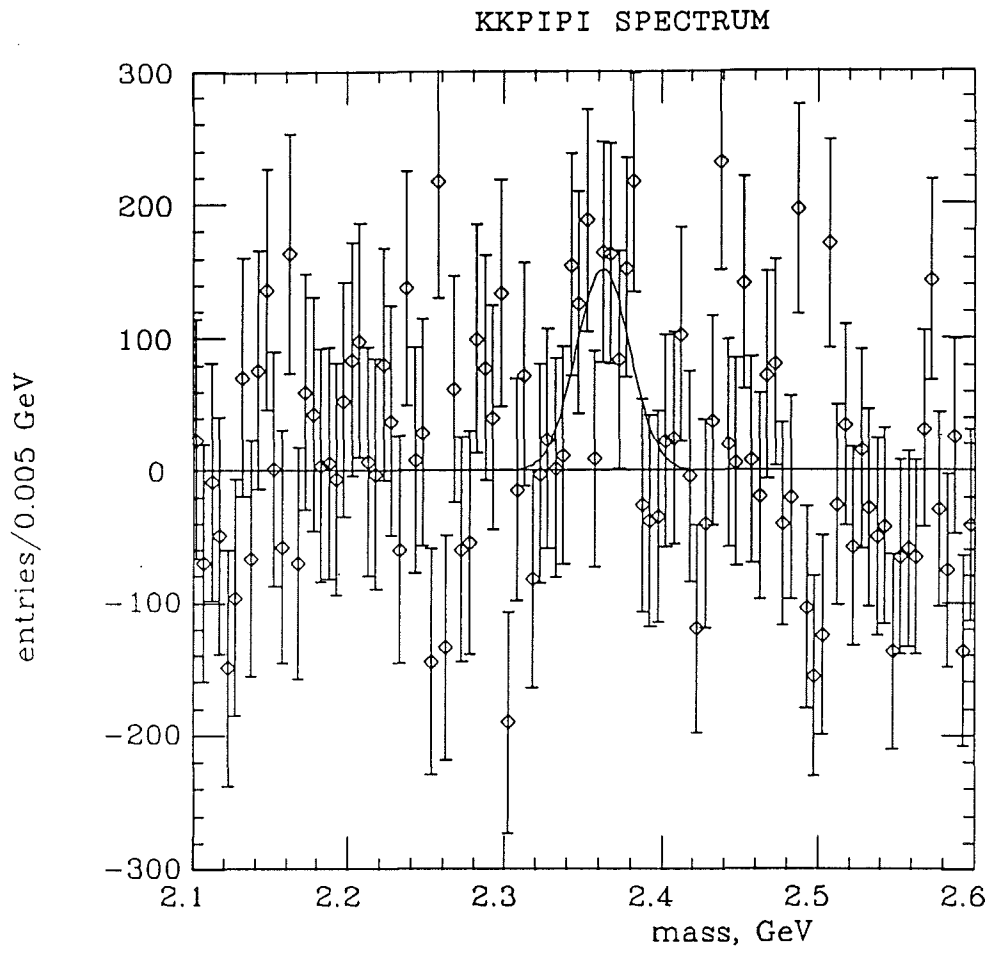


FIG. 41. KKππ spectrum, background-subtracted.

KKPIPI SPECTRUM



FIG. 42. KKππ spectrum, 0.03 GeV/c$^2$ mass bins

W

KKPIPI SPECTRUM
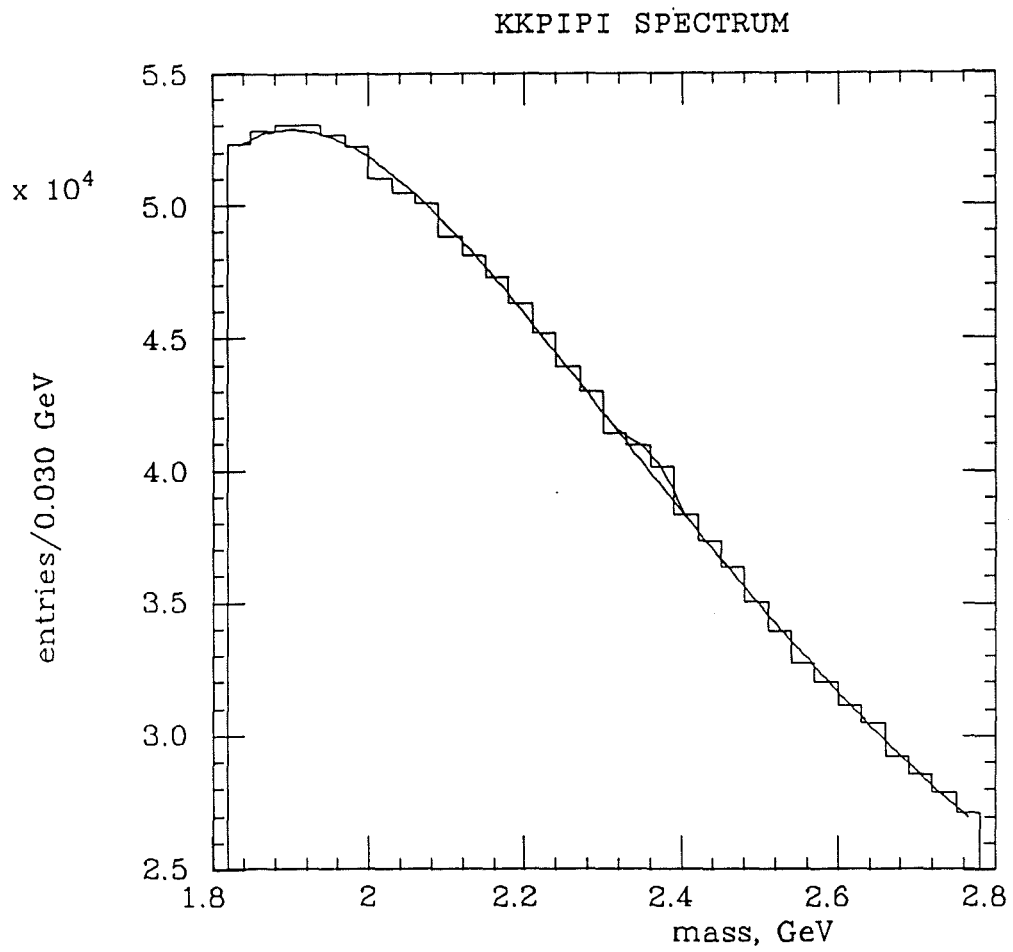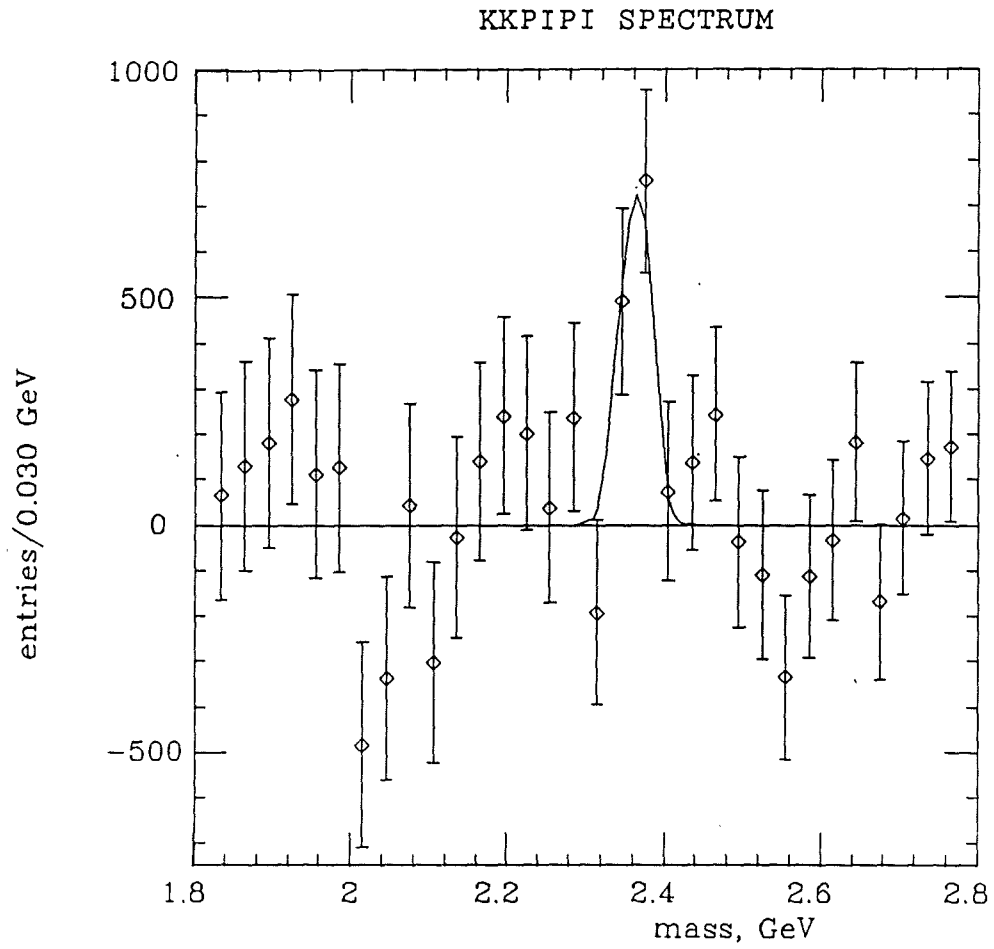


FIG. 43. KK$\pi\pi$ spectrum, 0.03 GeV/c$^2$ mass bins, background-subtracted

INTEGRATED PT SPECTRUM
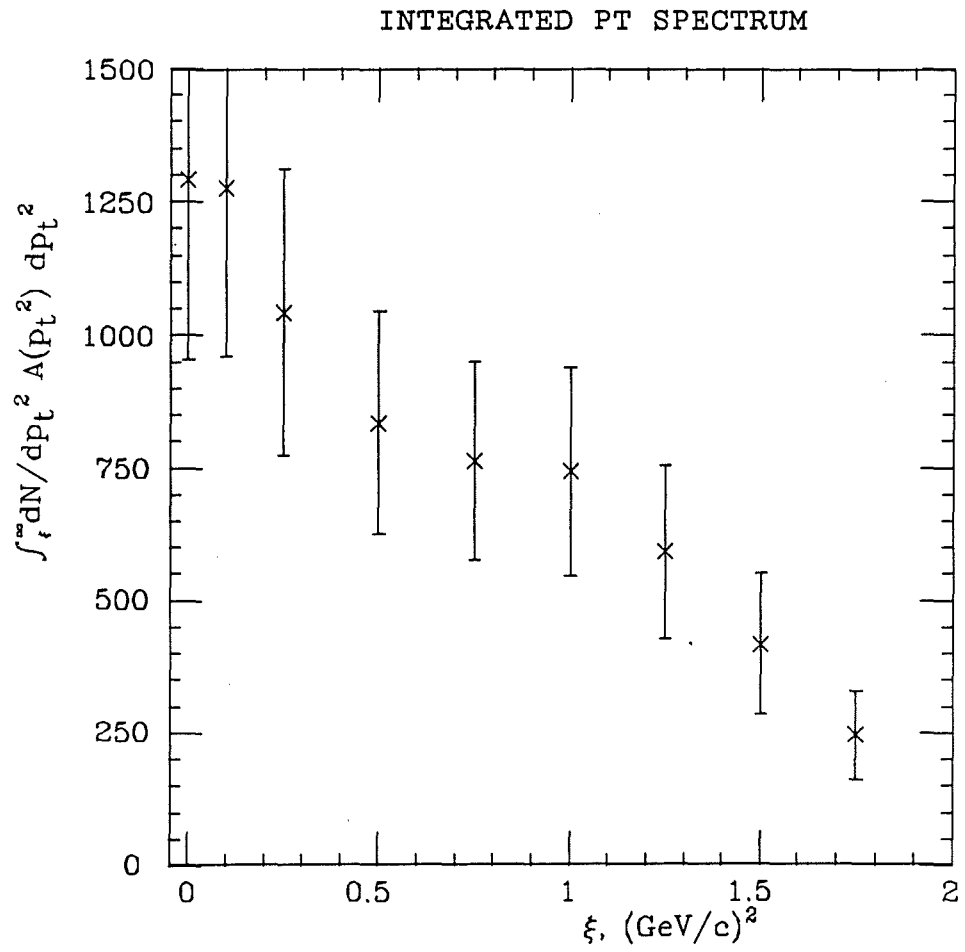


FIG. 44.   Integral $p_t^2$ spectrum

TABLE X

MULTIPLICITY DISTRIBUTION OF X(2.36)

| | $N_K \geq 4$ | $N_K \geq 5$ |
|---|---|---|
| $N_\pi \geq 2$ | $1291 \, {}^{+ \, 368}_{- \, 338}$ | $874 \, {}^{+ \, 302}_{- \, 243}$ |
| $N_\pi \geq 3$ | $982 \, {}^{+ \, 326}_{- \, 308}$ | $\cdots$ |
| $N_\pi \geq 4$ | $988 \, {}^{+ \, 316}_{- \, 294}$ | $\cdots$ |

The set of triggers from which these events were taken all involve a requirement of four kaons, with additional requirements of one or two φ's in the majority of the events. The triggers which contributed to this data sample, and the number of resonant candidate entries which come from each trigger type, are given in Table XI. As can be seen from this table, the requirement of a φφ trigger halves the fractional contribution of that subset of events to the total X(2.36) sample. Consequently, the two kaons in the candidate state are seen to be uncorrelated; they do not form φ, and do not appear to form any other resonance.

Given that the trigger is designed to detect φ mesons, the ability of the other $K^+K^-$ pair in the event to form φ is evaluated. The $K^+K^-$ effective mass spectrum is examined for φ produced in association with the X(2.36) by comparing spectra between the "resonance band" and "sideband," where the resonance band consists of those KKππ within $\pm$ 0.07 GeV/c$^2$ of the 2.363 GeV/c$^2$ resonance mass, and the sideband extends an additional 0.07 GeV/c$^2$ on either side of the resonance band. The $K^+K^-$ in this spectrum are those in the event not included in the KKππ combination (multiple entries from any given event are permitted). The $K^+K^-$ spectrum associated with the resonance band is shown in Fig. 45, and the spectrum associated with the sideband is shown in Fig. 46. The KK spectra are fit to a φ of mass and width fixed at the values obtained for the entire sample and presented above. An excess of 879 $\pm$ 199 φ are seen in association with the resonance band, and an excess of 586 $\pm$ 196 in association with the sideband. Thus, 293 $\pm$ 279 φ are produced in association with the resonance candidate.

TABLE XI

TRIGGER DEPENDENCE OF X(2.36)

| TRIGGER | NUMBER OF EVENTS | NUMBER OF X(2.36) | FRACTION OF EVENTS CONTAINING X(2.36) | SIGNAL TO BACKGROUND OF X(2.36) |
|---------|------------------|-------------------|---------------------------------------|---------------------------------|
| 4K | 9564 | 256 $\pm$ 148 | 0.027 | 0.0117 |
| $\phi$KK | 5129 | 154 $\pm$ 80 | 0.030 | 0.0241 |
| $\phi\phi$ | 80093 | 1047 $\pm$ 306 | 0.013 | 0.0112 |
| $\phi\phi$PT[a] | 24557 | 108 | 0.004 | $\cdots$ |
| TOTAL | 94786 | 1457 $\pm$ 349 | 0.015 | $\cdots$ |

[a]The $\phi\phi$PT trigger is a subset of the $\phi\phi$, not an independent sample. The X(2.36) component in this trigger is completely contained within a 0.010 GeV/c$^2$ bin width. It is not a robust signal, and is not used in the total.
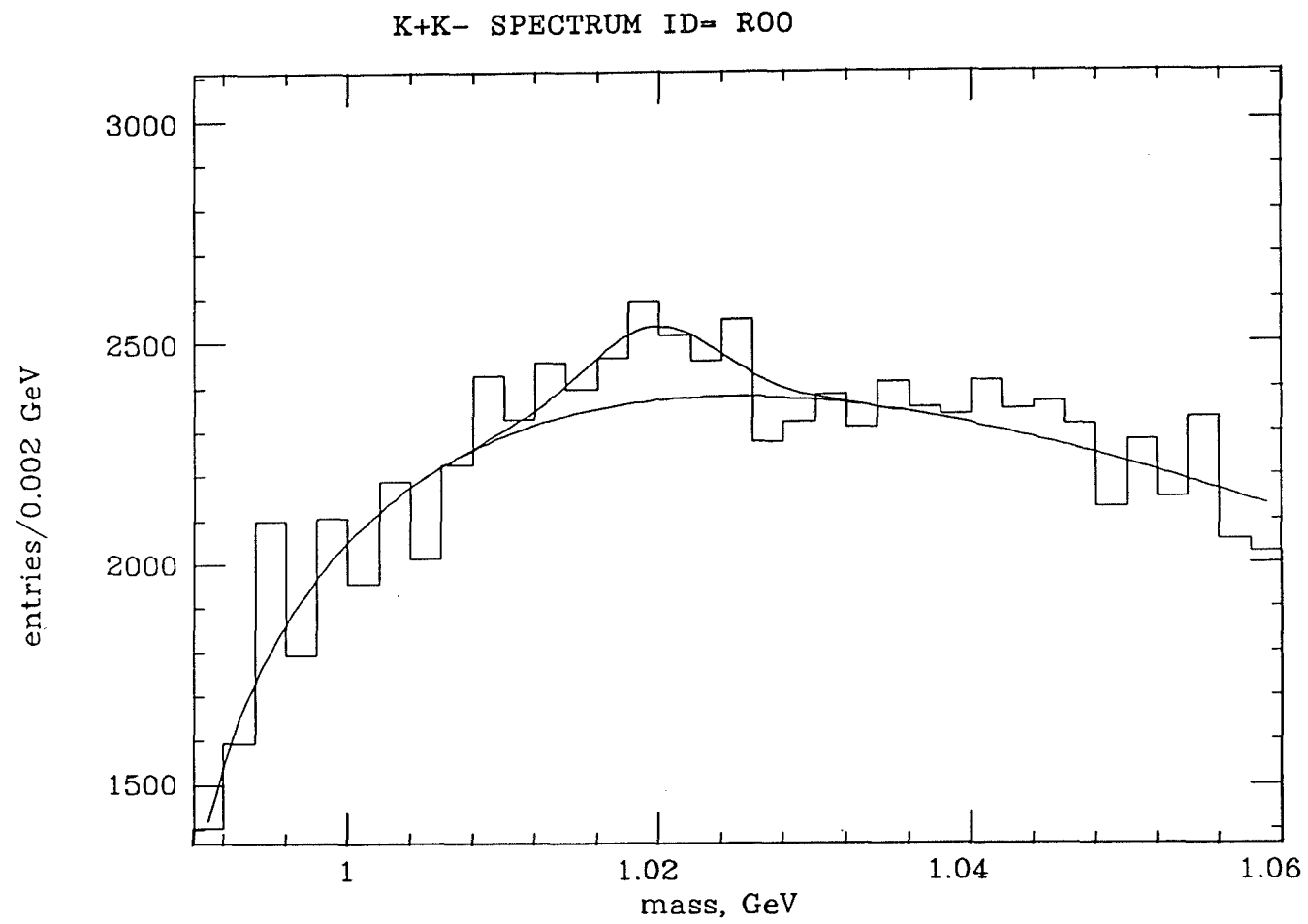
K+K- SPECTRUM ID= R00



FIG. 45.  $K^+K^-$ spectrum associated with resonance band
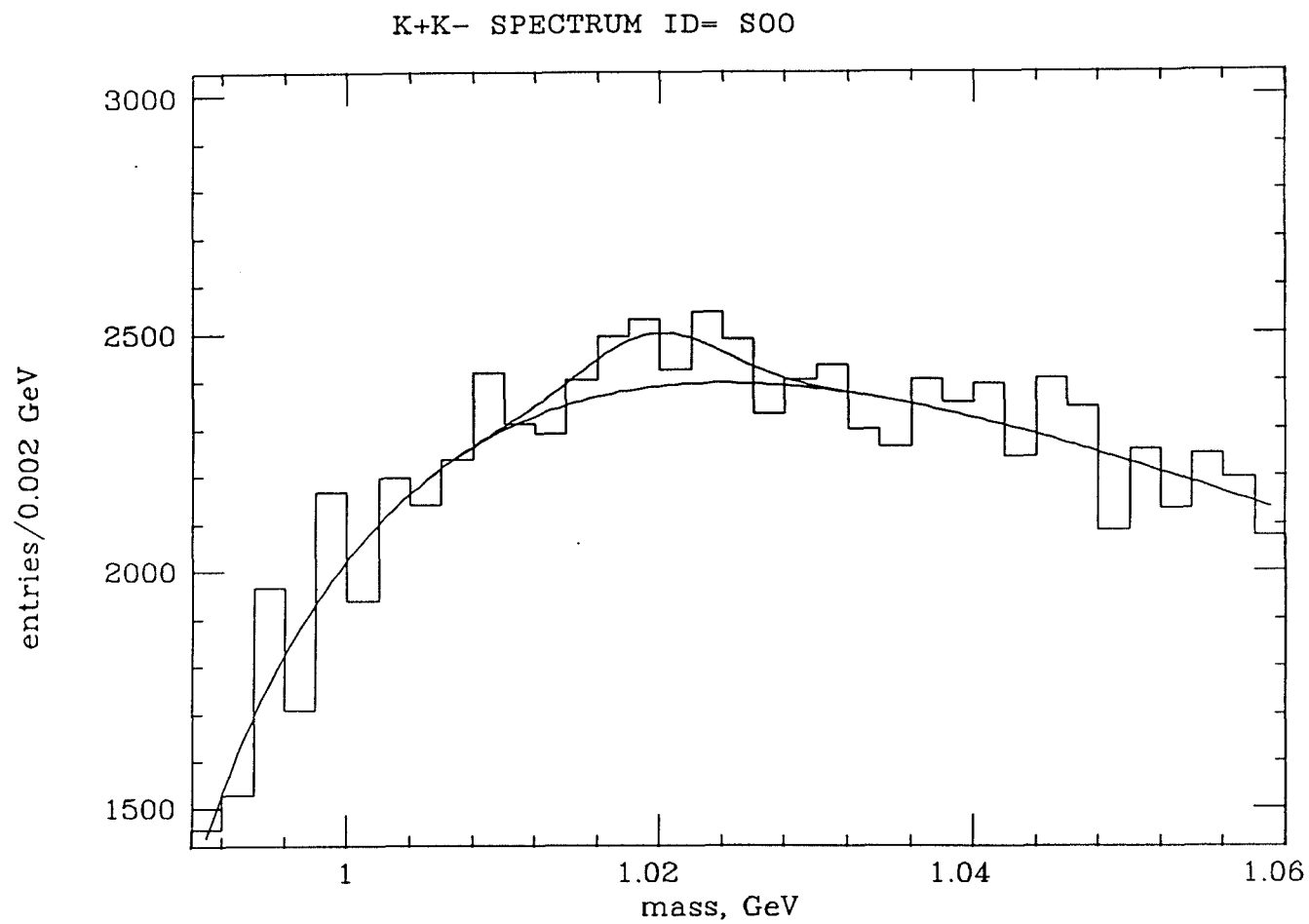
K+K- SPECTRUM ID= SOO



FIG. 46. $K^+K^-$ spectrum associated with sideband

In addition, the data were examined for any match in momentum transverse to the beam between the resonance candidate and the associated $\phi$. The momentum of the $K^+K^-$ and of the $K^+K^-\pi^+\pi^-$ were each calculated in the plane perpendicular to the beam, and the dot product

$$U = \vec{P}_{t(K^+K^-)} \cdot \vec{P}_{t(K^+K^-\pi^+\pi^-)}$$

calculated. If the particles are produced in opposition, $U \leq 0$; else, they are produced in parallel, $U > 0$. In Table XII, the numbers of $\phi$ associated with the resonance band and the sideband are given for all $U$, for $U \leq 0$, and for $U > 0$. The majority of the excess $\phi$ is observed to be in the half-plane opposite the resonance candidate, and the asymmetry is greater for the resonance band than for the sideband. These results, although only at the 1.5 standard deviation level, are consistent with the interpretation of a resonance produced in association with a $\phi$.

D.  Acceptance and Cross-section

The cross section for the production of a resonance is usually obtained by the use fo the formula

$$\sigma \cdot BR = \frac{N_{obs}}{N_B N_T} \frac{W}{A},$$

where $\sigma$ is the integrated cross-section, BR is the branching ratio to the observed channel, $N_{obs}$ is the observed number of events above background, $N_B$ is the total integrated beam on target, $N_T$ is the number of target nucleons per unit area, W is a weighting factor which corrects for particle decay in the spectrometer, and A is the integrated acceptance for the channel. The product $N_B N_T$ is the integrated sensitivity S, and is equal to 800 events/nb in this experiment. The weighting factor W is estimated by using the mean momentum of identified kaons, 10 GeV/c, and calculating the fraction which decay before

TABLE XII

PRODUCTION OF $\phi$ ASSOCIATED WITH X(2.36)

| $\phi$/X MOMENTUM | X(2.36) BAND | X(2.36) SIDEBAND | DIFFERENCE | RATIO |
|---|---|---|---|---|
| ALL | 879 $\pm$ 199 | 586 $\pm$ 196 | 293 $\pm$ 279 | 1.5 $\pm$ 0.61 |
| u $\leq$ 0 | 584 $\pm$ 196 | 390 $\pm$ 139 | 194 $\pm$ 194 | 1.5 $\pm$ 0.64 |
| u > 0 | 236 $\pm$ 144 | 177 $\pm$ 132 | 59 $\pm$ 195 | 1.3 $\pm$ 1.20 |
| DIFFERENCE | 348 $\pm$ 198 | 213 $\pm$ 192 | . . . | . . . |
| RATIO | 2.5 $\pm$ 1.6 | 2.2 $\pm$ 1.8 | . . . | . . . |

[a]The X(2.36) band is defined as those $K^+K^-\pi^+\pi^-$ combinations with mass M within 0.07 GeV/c$^2$ of the nominal 2.36 mass; that is, 2.293 < M <2.433. The sidebands are the bands of equal width on either side of the X(2.36) band; that is, 2.223 < M < 2.503, excluding the band above.

reaching the CB mirrors; for four kaons, this yields $W = 1.61$.

The most difficult problem in the analysis of an experiment such as this is the deconvolution of the cross-section and the acceptance. Without a detailed production model for the resonance candidate, an understanding of the method by which the candidate triggers (including the trigger identification of the associated particles), and a model for the generation of false triggers by the processor, the fractional acceptance as defined by the equation above cannot be determined. As seen in Table XI, the dynamical contributions of the different trigger types are themselves different. Further, the resonance candidate does not produce measurable $\phi$ in its $K^+K^-$ component. Thus, it has not been possible to determine the fractional acceptance for the resonance candidate.

However, the effects of the trigger on the subsample of $293 \pm 279$ $K^+K^-\pi^+\pi^-$ observed in association with an additional $\phi$ has been analyzed. A detailed Monte Carlo study of the $\phi K^+K^-$ acceptance was performed during the analysis of the $\phi\phi$ described in Sect. B, and a $\phi KK$ acceptance of $(4.6 \pm 0.5) \times 10^{-4}$ was obtained.[4] This $\phi KK$ acceptance includes the effect of the 49.5% branching ratio for $\phi \longrightarrow K^+K^-$ decay. The analysis also yielded an independent per-track acceptance of $0.85 \pm 0.01$. The total acceptance for this subsample is thus

$$A = (4.6 \pm 0.5)(0.85 \pm 0.01)^2 \times 10^{-4} = (3.3 \pm 0.4) \times 10^{-4},$$

and the corresponding

$$\sigma(X(2.36)\phi) \cdot BR(X \longrightarrow K^+K^-\pi^+\pi^-) = 1.77 \pm 1.70 \ \mu b.$$

E.   Interpretation of Results

The first step in the analysis of a resonance state is a review of previous work in the given mass region.   The 2.36 GeV/c$^2$ region is infamous for the observation of resonance states with low experimental statistics[10,48-63].   A   summary   of   observations   in   this   region   is presented in Table XIII.   As can be seen, the evidence tends to suggest two   resonances   in   that   region,   the   I = 0   $f_4$(2.300)   and   the   I = 1 $\rho_5$(2.350).   However,   the   agreement   of   these   results   is   poor,   and   the Particle   Data   Group   does   not   consider   these   resonances   to   be   well established.

Three   of   these   measurements[48,58,59]   are   indicative   of   narrow resonance   production.   Two   of   these   are   pion-produced   missing   mass measurements,   with   indeterminate   decay   chains   for   the   resonance   state. The   third   measurement   is   a   formation   experiment   with   decay   through $K\bar{K}3\pi$[48],   which   gives   excellent   agreement   in   mass   and   width   with   the present   observation,   but   which   was   not   confirmed   in   later   $K\bar{K}3\pi$ studies[62,63].   If   the   present   result   is   indeed   a   confirmation   of   this measurement,   the   $\bar{p}p$   formation   suggests   that   the   candidate   is,   in   fact,   a baryonium   state   containing   an   $s\bar{s}$   pair.   The   $\bar{p}p$   formation   of   such   a   state is   shown   in   Fig.   47a;   $\pi^-p$   production   is   shown   in   Fig.   47b,   and   pp production   in   Fig.   47c.

Charmed   interpretation   of   this   resonance   is   impossible   given   the apparently   large   $\sigma \cdot BR$   of   the   state   and   the   non-observation   of   charmed substates.   Given   that   the   resonance   is   above   threshold   for   DK   or   $D_s\pi$ decay,   failure   to   observe   a   charmed   component   is   conclusive.   The   K$\pi$   and K$\pi\pi$   submasses   were   not   observed   to   form   the   $K^*$(0.892)   or   other   allowed   K

TABLE XIII

RESONANCE OBSERVATIONS IN THE 2.36 GeV/c$^2$ REGION

| REFERENCE | BEAM PARTICLE | MOMENTUM GeV/c | DETECTED FINAL STATE | MASS GeV/c$^2$ | WIDTH GeV/c$^2$ | I | J$^P$ |
|---|---|---|---|---|---|---|---|
| 48 | $\bar{p}$ | 1.51-1.91 | $KK\pi\pi\pi$ | 2.360±0.025 | <0.060 | 1 | -- |
| 49 | $\bar{p}$ | 0.7 -2.4 | $\pi\pi$ | ∿2.480 | ∿0.210 | 1 | $5^-$ |
|  |  |  |  | ∿2.310 | ∿0.210 | 0 | $4^+$ |
| 50 | $\bar{p}$ | 0.7 -2.4 | $K^+K^-$ | ∿2.500 | ∿0.150 | 1 | $5^-$ |
|  |  |  |  | ∿2.340 | ∿0.150 | 0 | $4^+$ |
| 51 | $\bar{p}$ | - | $\pi\pi$ | ∿2.250 | ∿0.300 | 1 | $5^-$ |
|  |  |  |  | ∿2.300 | ∿0.200 | 0 | $4^+$ |
| 52 | $\bar{p}$ | - | $\pi\pi$ | ∿2.300 | ∿0.250 | 1 | $5^-$ |
|  |  |  |  | ∿2.300 | ∿0.200 | 0 | $4^+$ |
| 53 | $\bar{p}$ | 1.0 -3.3 | $\sigma_T(\bar{p}p)$ | 2.345±0.010 | ∿0.140 | 1 | -- |
|  |  |  |  | 2.380±0.010 | ∿0.140 | 0 | -- |
| 54 | $\bar{p}$ | ∿2.0 | $\sigma_T(\bar{p}p)$ | 2.359±0.002 | $0.165^{+0.018}_{-0.008}$ | - | -- |
| 55 | $\bar{p}$ | 0.7 -2.4 | $\bar{p}p$ | 2.345±0.015 | ∿0.135 | - | -- |
| 56 | $\bar{p}$ | 0.97-3.0 | $\bar{n}n$ | ∿2.380 | -- | - | -- |
| 57 | $\bar{p}$ | 1.0 -2.0 | $\pi^0\pi^0$ | ∿2.330 | -- | - | -- |
| 58 | $\pi^-$ | 16.0 | $(MM)^-$ | 2.370±0.017 | ∿0.057 | - | -- |
| 59 | $\pi^-$ | 3.0 -12.0 | $(MM)^-$ | 2.382±0.024 | <0.030 | - | -- |
| 60 | $\bar{p}$ | 0.7 -2.4 | $\pi\pi,KK$ | ∿2.330 | -- | - | 5 |
| 61 | $\bar{p}$ | 1.0 -2.0 | $\pi^+\rho^-$ | BROAD | BROAD | - | -- |
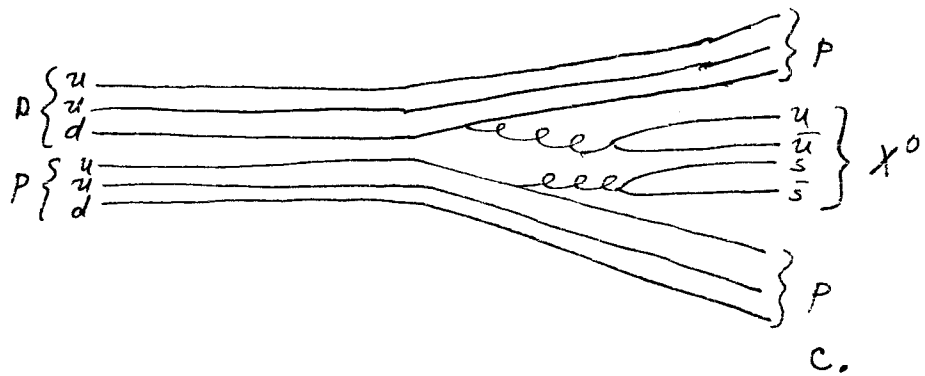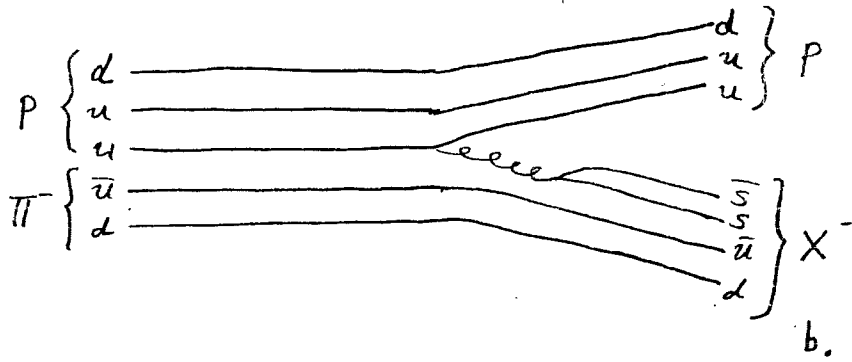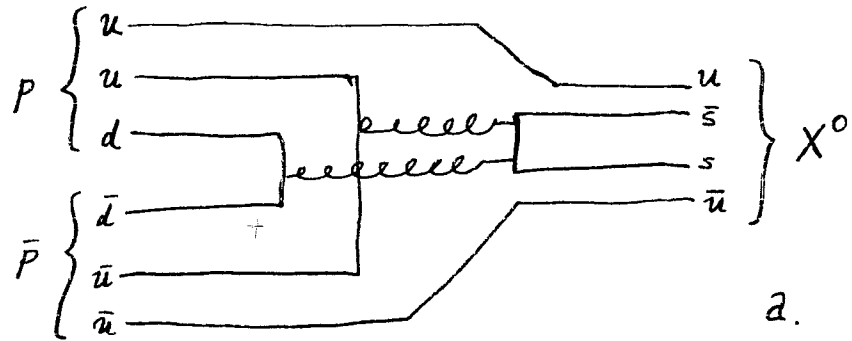
FIG. 47. Production mechanisms of baryonium states
(a) p̄p (b) π⁻p (c) pp

resonances (see Fig. 7), demonstrating that uncorrelated $K^+K^-\pi^+\pi^-$ is the actual decay mode. Since the net parity of the decay products is +1, the net parity of the state is even or odd as J is even or odd. Given that the width of the state is dominated by the experimental resolution, interpretation of the state as an ordinary $q\bar{q}$ meson is unconvincing. As stated in Ref. 22, however, an F-wave (L = 3) state may possess a narrow width because of its large angular momentum; the angular momentum barrier in the isosinglet states inhibits the annihilation decay modes. Based on the observable quantum numbers, it cannot be determined whether the state might also be either a glueball or a hybrid $s\bar{s}g$ state. Possible decay diagrams for each of these hypotheses are shown in Fig. 48. As can be seen, the $q^2\bar{q}^2$ interpretation has open an OZI superallowed decay mode, which should tend directly to form intermediate meson states not observed by this experiment. This observation is not, by itself, conclusive; baryonia are often seen with narrow widths despite the expectation of superallowed decay modes. It is possible that, for these states, some suppression mechanism inhibits the superallowed decay (for example, an angular momentum barrier as described above). This quark combination is also produced as an intermediate state in the decay of either the gg glueball or the $s\bar{s}g$ hybrid as shown in Fig. 48c-d. The additional strong vertices should act to suppress the rate, and could lead to the narrow width observed if other decay modes proved forbidden. However, these possibilities can only be postulated in the absence of further information about the quantum numbers of the state.
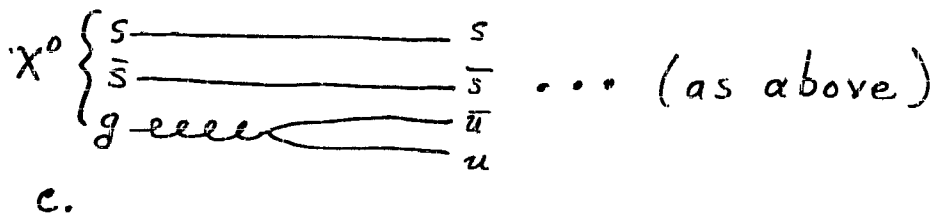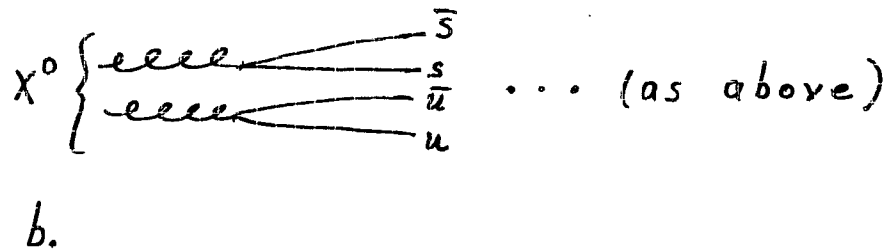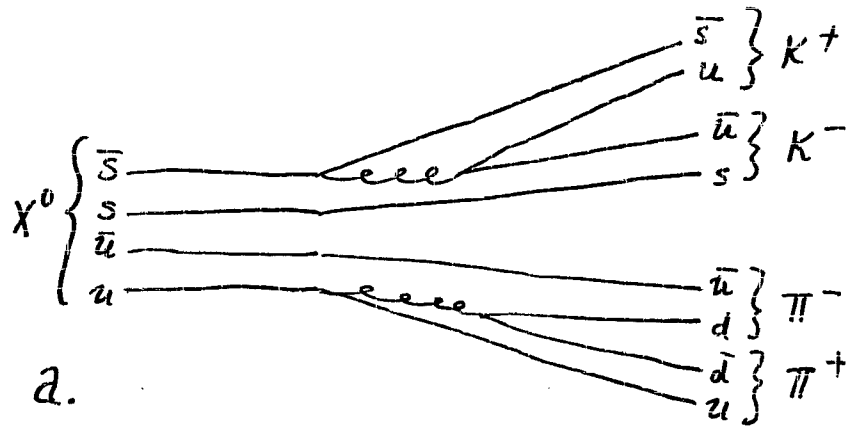
FIG. 48. Decay mechanisms of candidate interpretations to $K^+K^-\pi^+\pi^-$ (a) exotic meson (b) glueball (c) $s\bar{s}g$ hybrid

W

CHAPTER VI

SUMMARY AND CONCLUSIONS

This thesis is the presentation of results from Fermilab experiment E623. Experiment E623 is a study of pN final states including two $K^+K^-$ pairs, with a software trigger designed to enhance the observation of low-mass $K^+K^-$ pairs in a search for massive states decaying through $\phi\phi$. The present study is an examination of the $K^+K^-\pi^+\pi^-$ final state occurring in the events selected by this trigger. A $K^+K^-\pi^+\pi^-$ resonance candidate is observed at a mass of $2.363 \pm 0.005$ GeV/c$^2$, with a FWHM of $0.040 \pm 0.015$ GeV/c$^2$. The observed signal has $1291 ^{+\,368}_{-\,338}$ entries over a large background in $K^+K^-K^+K^-\pi^+\pi^-$ events; of these events, $293 \pm 279$ entries are observed in conjunction with the additional $\phi$ selected by the trigger. Given the $(3.3 \pm 0.4) \times 10^{-4}$ acceptance for $\phi KK\pi\pi$, this corresponds to a cross section of

$$\sigma(\phi X(2.36)) \cdot BR(X \longrightarrow KK\pi\pi) = 1.77 \pm 1.70 \; \mu b.$$

The state is consistent with a $K\bar{K}3\pi$ resonance previously observed (but not confirmed with higher statistics) in $\bar{p}p$ interactions. If this is a new observation of that state, the formation mechanism suggests that the state is a $s\bar{s}q\bar{q}$ baryonium/exotic meson of isospin 1. If not, only the interpretation of the new resonance as a charmed state has been ruled out. Interpretation of this state as glueball, narrow $s\bar{s}$, or hybrid $s\bar{s}g$ are equally permitted within the constraints of the data.

W

REFERENCES

1. Abrams, R., et al, Fermilab Proposal No. P-623, 1979.

2. Green, D., Addendum to Fermilab Proposal No. P-623, 1980.

3. Fenker, H., "The E623 Trigger Processor," 1981; H. Fenker et al, Fermilab-Pub-82/62-Exp, 1982.

4. Davenport, T. F., Ph.D. thesis, Florida State University, 1984.

5. Davenport, T. F., et al, Phys. Rev. D33, 2519 (1986).

6. Georgiopoulos, C. H., Ph.D. thesis, Tufts University, 1985.

7. Georgiopoulos, C. H., et al, Physics Letters 152B, 428 (1985).

8. Torres, S., Ph.D. thesis, Virginia Polytechnic Institute and State University, 1985.

9. Torres, S., et al, Phys. Rev. D34, 707 (1986).

10. Green, D. R., et al, Phys. Rev. Lett. 56, 1639 (1986).

11. The material presented in Chapter II is an abstract of readings from the following nine references, barring other specific reference. The presentation and interpretation remain the author's, as do any failures of the same. Sections D, E, and F of this chapter are abstracted from a previous report by the author, "Glueballs and $q^2\bar{q}^2$ Exotic Mesons: Search in $\phi\phi$ and $K^{*0}\bar{K}^{*0}$ Channels."

12. Wohl, C. G., et al, Review of Particle Properties, Rev. Mod. Phys. 56, S1 (1984); M. Aguilar-Benitez, et al, ibid, Physics Letters 170B, 1 (1986).

13. Close, F. E., An Introduction to Quarks and Partons, (Academic, 1979).

14. Perkins, D. H., Introduction to High Energy Physics, 2nd ed. (Addison-Wesley, Reading MA, 1982).

15.  Quigg, C., Fermilab-Conf-80/64-Thy, 1980.

16.  Leader, E., and E.  Predazzi, An Introduction to Gauge Theories and the "New Physics", (Cambridge, New York, 1982).

17.  Fritsch, H., Quarks, Basic Books, 1983.

18.  Fraunfelder, H., and E. M. Henley, Subatomic Physics, (Prentice Hall, 1974).

19.  Aitchison, I. J. R., and A.  J.  G.  Hey, Gauge Theories in Particle Physics, (Adam Hilger, 1982).

20.  Cummins, E., and P.  Bucksbaum, Weak Interactions of Leptons and Quarks, (Cambridge, 1983).

21.  Crater, H. W., and P.  Van Alstine, Phys. Rev. Lett. 53, 1527 (1984).

22.  Godfrey, S., et al, Physics Letters 141B, 439 (1984).

23.  Ammar, R., et al, FERMILAB-PUB-86/112-E, 1986.

24.  Reucroft, S., presented at the XXI Rencontri de Moriond, Les Arcs, 1986 (unpublished).

25.  Matveev, V. A., and P.  Sorba, L. Nuovo Cimento 20, 435 (1977).

26.  D'Agostini, G., et al, Physics Letters 104B, 330 (1981).

27.  D'Agostini, G., et al, Nuclear Physics B209, 1 (1982).

28.  Carroll, A. S., et al, Phys. Rev. Lett 32, 247 (1974).

29.  Montanet, L., Report CERN/EP-80-51, 1980.

30.  Lipkin, H. J., Report FERMILAB-Conf-83/65-THY, 1983.

31.  Kitazoe, T., et al, Kobe University Report KULA-HP-11, 1983.

32.  Chanowitz, M. S., and S.  R.  Sharpe, Report LBL-16489, 1983.

33.  Chanowitz, M. S., Report LBL-16653, 1983.

34.  Chanowitz, M. S., Report LBL-16541, 1983.

35.  Etkin, A., et al, Phys. Rev. Lett. 49, 1620 (1982).

36.  Lindenbaum, S. J., Report BNL-33401, 1983.

37. Lindenbaum, S. J., Report BNL-33650, 1983.

38. Clavelli, L., presented at Vanderbilt University, Nashville TN, 1983 (unpublished).

39. Jaffee, R. L., Report MIT-CTP-657, 1977.

40. Li, B.-A., and K.-F. Liu, Phys. Rev. D28, 1636 (1983).

41. Li, B.-A., and K.-F. Liu, "A possible explanation of $\rho^0\rho^0$ production in J/insy radiative decay," University of Kentucky, 1983.

42. Li, B.-A., and K.-F. Liu, Phys. Rev. D29, 426 (1984).

43. Breakstone, A., et al, Report CERN/EP-83-157, 1983; K. Bochmann, Bonn University Report BONN-HE-83-18, 1983.

44. Chanowitz, M. S., and S. R. Sharpe, Nuclear Physics B222, 211 (1983).

45. Li, B.-A., and K.-F. Liu, Phys. Rev. Lett. 51, 1510 (1983).

46. Napier, A., et al, Physics Letters B149, 514 (1984).

47. Bourquin, M., and J. M. Gaillard, Nuclear Physics B114, 334 (1976).

48. Oh, B. Y., et al, Phys. Rev. Lett. 24, 1257 (1970).

49. Carter, A. A., et al, , Physics Letters 67B, 117 (1977).

50. Carter, A. A., Nuclear Physics B141, 467 (1978).

51. Martin, A. D., and M. R. Pennington, Nuclear Physics B169, 216 (1980).

52. Martin, B. R., and D. Morgan, Nuclear Physics B176, 355 (1980).

53. Abrams, R. J., et al, Phys. Rev. Lett. 18, 1209 (1967).

54. Alspector, J., et al, Phys. Rev. Lett. 30, 511 (1973).

55. Coupland, et al, Physics Letters 71B, 460 (1977).

56. Cutts, D., et al, Phys. Rev. D17, 16 (1978).

57. Dulande, et al, Physics Letters 79B, 335 (1978).

58.  Anderson, E. W., _et al_, _Phys_. _Rev_. _Lett_. 22, 1390 (1969).

59.  Focacci, M. N., _et al_, _Phys_. _Rev_. _Lett_. 17, 890 (1966).

60.  Nicholson, H., _et al_, _Phys_. _Rev_. D7, 2572 (1973).

61.  Yoh, J. K., _et al_, _Phys_. _Rev_. _Lett_. 26, 922 (1971).

62.  Chapman, J. W., _et al_, _Phys_. _Rev_. D4, 1275 (1971).

63.  Oh, B. Y., _et al_, _Nuclear Physics_ B51, 57 (1972).